Interferometric Scattering Microscopy: from Bacterial Dynamics to Molecular Assembly



Adam Fineberg

St Hugh's College

University of Oxford

A thesis submitted for the degree of

Doctor of Philosophy in Theoretical and Physical Chemistry

11th October, 2019

Acknowledgements

During the last few years, I have been fortunate to have the support and guidance from a number of outstanding people, both in my academic and social lives.

Firstly, I would like to thank my supervisor, *Philipp Kukura*, for the help and guidance he has offered me over the course of my time in such a fantastic group. The Kukura group have been an amazing set of people, whom I have been privileged to call both friends and colleagues. When I first joined, *Joanna 'MJ' Andrecka* took me under her wing and has been an invaluable source of guidance and advice, teaching me what the 'bio' in biophysics meant. For the technical side of my work I would like to thank *Dan Cole* for the hours of microscope instruction and troubleshooting: your advice has saved me many long nights in the lab realigning my optics. I must of course also thank *Gavin Young*, my partner in crime. Not only have you been a fantastically patient colleague in our work together, but have been a constant source of good humour and conversation, somehow keeping me sane through it all. Thank you also to *Nick Hundt* and *Manish Kushwah*, as well as the rest of the Kukura group, for your help and friendship over the past few years.

I would not have had such an amazing time during my DPhil had it not been for my dancing friends. We have had so much fun together and no matter how stressed I have been at the start of our dance sessions, you always left me with a smile on my face. I am especially grateful to my talented dance partner *Christine Potter*, who has been such a source of enjoyment and kindness

throughout our time dancing together. I would also like to thank my friends in the Oxford JSoc and Jewish community, especially *Rabbi Michael and Tracey*, for your hospitality and friendship, making Oxford a real home-from-home during my Jewish life here.

Most importantly, I would like to thank my parents for their continuous encouragement and guidance throughout my studies in Oxford. I am truly grateful for everything you have done for me. Finally, I must give a special mention to *Peter*: we may have only known each other for about a month, but I hope this thesis is a true testament to you're prof reding abillity.

Statement of Originality

The research described in this thesis was carried out by the author between October 2015 and September 2019 and includes nothing which is the outcome of work done in collaboration, except where specifically indicated in the text. The use of the first person plural is strictly a matter of style in keeping with standard scientific convention.

Abstract

We explore the capabilities of interferometric scattering microscopy (iSCAT) by investigating a series of biophysical systems that span a range of particle sizes, down to the single particle level.

The work presented starts with single particle tracking of 20 nm gold nanoparticles bound to single myosin 5a molecules. We identify temporally and spatially constrained transient states of the different domains of myosin 5a, shedding light on the structural transitions that the molecule undergoes. The work demonstrates iSCAT's ability to reveal global conformational changes and relative motions of different domains in a single protein.

Next, we make the transition to explore iSCAT's capability for label-free studies of complex biophysical systems. By minimising iSCAT's phototoxicity, we visualise bacterial protein filaments extending from the bacterial cell body. This allows us to understand the roles of different proteins which are employed under varying friction environments to maintain pili function.

By further improving iSCAT's ability to measure smaller scattering signals, we next monitor the assembly kinetics of a MDa-sized gold coordinated protein cage, label-free, in solution. The work demonstrates iSCAT's suitability to determine kinetic information from biological systems, as a dynamic approach complementary to cryoEM.

Lastly, we present an experimental assay to measure the dissociation constant of a simple interaction between two 55 kDa proteins, highlighting the potential for iSCAT to become a universal analytical tool for quantifying protein-protein interactions.

Contents

List of Figures iii

List of Abbreviations vii

1 Introduction 1

2 Theoretical Background 5

2.1 Fluorescence Microscopy 5

2.2 Scattering Microscopy 7

Darkfield & Interferometric Scattering Microscopies 8

Contrast Enhancement via Numerical Aperture Filtering . . 14

Mass Photometry 17

3 Experimental Design 19

3.1 Interferometric Scattering Microscopy 20

The iSCAT Channel 20

Focus Stabilisation 22

3.2 Correlative iSCAT and Fluorescence 24

Fluorescence Channel 24

Image Registration 27

iSCAT for Photosensitive Systems 30

3.3 iSCAT for Mass Photometry 31

Image Processing and Particle Detection 32

3.4 Microscope Stabilisation 35

4 Structural Coupling in Myosin 5a 39

4.1 Introduction 39

4.2 Methods 46

4.3 Results and Discussion 50

Lever Arm Experiments 51

Stalk Domain Experiments 54

Correlation of Motor - Stalk Domain Localisation 56

Dwell Time Analysis 58

4.4 Conclusions and Outlook 58

5 Type IV Pili Movements of *Pseudomonas aeruginosa* 61
5.1 Introduction . . . 61
5.2 Methods . . . 65
5.3 Results and Discussion . . . 70
Phototoxicity . . . 70
Visualising Bacterial Filaments . . . 70
Filament Morphology . . . 73
TFP Dynamic Activity . . . 75
TFP Dwell Time Analysis . . . 78
5.4 Conclusion and Outlook . . . 81

6 Assembly Kinetics of a Gold-Coordinated Protein Cage 85
6.1 Introduction . . . 85
6.2 Methods . . . 89
6.3 Results and Discussion . . . 92
Mass Photometry Measurement of TRAP(K35C/R64S) . . 92
Monitoring Cage Formation . . . 93
6.4 Conclusion and Outlook . . . 95

7 Determining the Dissociation Constant of a Dimeric System with Mass Photometry 97
7.1 Introduction . . . 97
7.2 Methods . . . 106
7.3 Results and Discussion . . . 108
Determining the Dissociation Constant . . . 108
7.4 Conclusion and Outlook . . . 110

8 Summary and Outlook 113
8.1 Summary . . . 113
8.2 Outlook . . . 114

References 117

List of Figures

Chapter 2

2.1 Signal detection in scattering microscopy 7
2.2 Localised surface plasmon resonance in a gold nanoparticle . . 10
2.3 Individual microtubules imaged with confocal scattering microscopy in reflectance mode 12
2.4 Raw and processed iSCAT images 13
2.5 Emission pattern in the back focal plane of the objective . . . 15
2.6 Raw and processed iSCAT images with numerical aperture filtering 16
2.7 A typical mass photometry calibration and a plot of measured mass vs. sequence mass in mass photometry 17

Chapter 3

3.1 A simple iSCAT setup 20
3.2 A polarisation-dependent optical isolator 21
3.3 A simple iSCAT with focus stabilisation 23
3.4 Ray tracing diagram of focus stabilisation mechanism 24
3.5 A correlative iSCAT and fluorescence setup 25
3.6 Determining the temporal synchronicity of the iSCAT and fluorescence channels 27
3.7 Image registration between iSCAT and fluorescence channels . 29
3.8 An iSCAT setup with correlative fluorescence adapted to photosensitive systems 30
3.9 A numerical aperture filtered iSCAT microscope for mass photometry 32
3.10 Image processing and analysis sequence for mass photometry . 33
3.11 An example of mechanical drift being averaged into a ratiometric image 35
3.12 An iSCAT setup optimised for stability 36
3.13 A compact iSCAT setup for mass photometry 37

Chapter 4

4.1 Domain structure of Myosin 5a 40
4.2 The definition of a step and a stride of Myosin 5a 41
4.3 The kinetic cycle for Myosin 5a 42
4.4 Current mechanism of the myosin step 45
4.5 A typical trace from a lever arm tracking experiment 52
4.6 A 2D density estimate of lever arm localisations before and after the unlabelled lever arm steps 53
4.7 A typical trace from a stalk tracking experiment 55
4.8 Trace from a dual labelled motor - stalk M5a experiment 57
4.9 Dwell time analysis of the stalk and the motor domains' transient states 58

Chapter 5

5.1 Type IV pili (TFP) assembly and subcomplex components . . 64
5.2 iSCAT reveals extracellular bacterial filaments 72
5.3 TFP dynamics in WT and *fliC*$^{-}$ 73
5.4 Visualisation of TFP position and retraction in three dimensions 74
5.5 Visualisation of TFP position and retraction in three dimensions 75
5.6 PilU does not affect number of TFP per cell 76
5.7 PilU does not affect TFP dynamics in free solution 77
5.8 Sequence of TFP function 78
5.9 Dwell time and tension time analysis 79
5.10 Coordination of TFP retraction motors 81

Chapter 6

6.1 Structure of the TRAP(K35C/R64S) 11-mer ring building block. 87
6.2 Cryo-electron microscopy density maps of TRAP-cage 88
6.3 Mass kernel density estimates for TRAP(K35C/R64S) without Au 92
6.4 Mass kernel density estimates for TRAP(K35C/R64S) with Au 93
6.5 Mass kernel density estimates for TRAP(K35C/R64S) with Au over 30 minutes 94
6.6 Time series of cage formation at high TRAP(K35C/R64S) concentration 95

Chapter 7

7.1 A schematic of the two modes of AUC 99
7.2 A schematic of an ITC experiment 101
7.3 A schematic of a typical SPR experiment 102
7.4 A schematic of a typical BLI experiment 103
7.5 Ribbon diagram of the tubulin dimer 105
7.6 Mass kernel density estimates for tubulin at varying concentrations 108
7.7 K_d measurements of tubulin over a range of concentrations . . 110

List of Abbreviations

ADP	Adenosine Diphosphate
AFM	Atomic Force Microscopy
AODs	Acousto-Optic Deflectors
ATP	Adenosine Triphosphate
Au-TPPMS	Monosulfonated Chloro(triphenylphosphine)gold(I)
AUC	Analytical Ultracentrifugation
biotCaM	Biotinylated Calmodulin
BLI	Biolayer Interferometry
BRB80	Brinkley BR Buffer 1980
CaM	Calmodulin
CMOS	Complementary Metal-Oxide-Semiconductor
DLS	Dynamic Light Scattering
eGFP	Enhanced Green Fluorescent Protein
EMCCD	Electron Multiplying Charge-Coupled Device
FGPA	Field-Programmable-Gate-Array
GDP	Guanosine Diphosphate
GTP	Guanosine Triphosphate
HMM	Heavy Meromyosin
IRM	Interference Reflection Microscopy
ITC	Isothermal Titration Calorimetry
LB	Luria-Bertani
LED	Light Emitting Diode
M5a	Myosin 5a
MALS	Multiangle Light Scattering
NA	Numerical Aperture
PBS	Polarising Beam Splitter
PDMS	Polydimethylsiloxane
PR	Partial Reflector
PSF	Point Spread Function
QWP	Quarter Waveplate
RICM	Reflection Interference Contrast Microscopy
RU	Response Units

SEC	Size Exclusion Chromatography
SNR	Signal to Noise Ratio
SPR	Surface Plasmon Resonance
TFP	Type Four Pili
TIRF	Total Internal Reflection Fluorescence
TRAP	trp RNA-Binding Attenuation Protein
WT	Wild-Type

Chapter 1
Introduction

For centuries, optical microscopy has been an essential tool for studying the physical properties of biological systems, both *in vivo* and *in vitro*.[1] From the invention of the first microscope aimed at observing microscopic organisms,[2] scientists have sought to improve the techniques in existence and find new ways to use the physics of light interacting with matter to probe deeper into biological systems. Recent advancements have pushed optical microscopy to new limits regarding resolution and sensitivity.[3]

Fluorescence, the most widely used optical microscopy technique today,[4] involves measuring the emission of light from fluorescent markers attached to a molecule of interest.[5,6] While incredibly effective, the technique is still limited in its ability to simultaneously achieve high temporal resolution and spatial precision. Recently, interferometric scattering microscopy (iSCAT) has emerged as a technique capable of achieving this,[7] and has been further developed to measure single protein molecules label-free.[8]

The work presented in this thesis builds on the previous development of iSCAT and continues its evolution from high spatial and temporal precision single particle tracking to label-free single protein detection in solution. To do this, the work follows four illustrative biological systems and the use of iSCAT to answer fundamental questions about their inner workings.

Chapter 2 details the theoretical background of scattering microscopy, discussing the advantages of its use over fluorescence microscopy and the advantages of iSCAT over pure scattering. The chapter continues to discuss

the theory of contrast enhancement via numerical aperture filtering and how an iSCAT microscope can be used for a mass photometry experiment.

Chapter 3 sets out the methodology of building an iSCAT microscope and details modifications and advancements necessary to answer the biological questions explored in this thesis. This includes building a correlative iSCAT and fluorescence setup, modifying an iSCAT setup to reduce phototoxicity to cells, implementing numerical aperture filtering to allow for sensitive mass photometry experiments, and stabilising an iSCAT microscope to achieve the best sensitivity possible.

Chapter 4 discusses iSCAT's use as a tool for single particle tracking by focusing on the motor protein myosin 5a. By tracking a gold label attached to different domains of the motor protein, we observe transient states for the different domains. This is complemented by correlative iSCAT and fluorescence measurements to probe the synchronicity of the movements of different domains of myosin 5a. The chapter describes the insight gained into the structural and mechanical properties of the protein by using iSCAT's high temporal and spatial precision.

In *Chapter 5*, we reveal how the pathogen *Pseudomonas aeruginosa* coordinates the motorised activity of type IV pili to power efficient surface motility through adaptations to iSCAT in order to reduce phototoxicity. The work uses dynamic label-free visualisations of type IV pili extension, attachment, and retraction events at high resolution in four dimensions. Through type IV pili measurements we gain a better understanding of the functions of PilT and PilU proteins when the bacteria is moving in free solution or under high-friction. The results are complemented by dwell time analysis allowing us to suggest a mechanism for the motility machinery during the bacterial cells' displacement.

Chapter 6 uses iSCAT with numerical aperture filtering to run sensitive

mass photometry experiments. We study the kinetics of the assembly of a capsid-like protein cage, self-assembled through gold coordination. The chapter explores the global assembly kinetics of the cages, laying the ground work for more complex kinetic studies using mass photometry.

Chapter 7 discusses preliminary experiments to demonstrate iSCAT suitability as a tool for determining the thermodynamic properties of biological systems. To do this, the work focuses on making measurements of the dissociation constant of a simple dimeric system, tubulin. The chapter starts with a discussion of current techniques to measure thermodynamic properties of biological systems and continues with our efforts to establish iSCAT as a single-molecule, label-free tool to extract dissociation constants.

Finally, *chapter 8* provides a short summary of the contents of this thesis and concludes with an outlook.

Chapter 2
Theoretical Background

Parts of this chapter have been adapted from content that will be published in the following invited book chapter:

> Y. Takagi, N. Hundt, A. Fineberg, 'Single-molecule biophysical techniques to study actomyosin force transduction' in *Myosins: A Superfamily of Molecular Motors*, ed. L. M. Coluccio, Springer Netherlands, Dordrecht, 2nd edn., vol. 7 of the Proteins and Cell Regulation series, ch. 6, *submitted.*

2.1 Fluorescence Microscopy

For many years, fluorescence microscopy has been the imaging tool of choice for those wishing to study biological systems in molecular detail, both *in vivo*[9,10] and *in vitro*.[11] As a tool for studying single molecule assays, new labelling techniques and experimental developments aimed at overcoming the diffraction limit have allowed fluorescence to grow to become a versatile tool with a wide range of applications.[12] These range from single molecule protein localisation to cell cytoskeleton dynamic studies, and have provided valuable insight into many different areas of the biological sciences.[5,13] Part of the success of fluorescence microscopy has been the relative ease of background suppression, through the use of optical filters, providing a large signal to noise ratio (SNR) and allowing for sensitive and specific imaging with high spatial resolution.[11] The main limitations of single molecule fluorescence microscopy are associated with the photophysics and photochemistry of the fluorescent labels.[13] A fluorophore's excitation-emission cycle has a limited frequency, determined by the finite lifetime of the excited state, limiting the number of emitted photons per second.

Non-radiative relaxation pathways of a given excited fluorophore reduce the quantum yield further limiting the number of detectable photons per unit time. Fluorophore localisation can be hampered due to blinking, the reversible transition into a non-fluorescent state, causing it to temporarily go dark.[14] This, together with oxidative stress and photobleaching, further impedes the quest for ever higher imaging speeds.[15] Additionally, the need to fluorescently label the system introduces additional experimental difficulties, such as toxicity of labelling conditions[16–18] or disruption of biological mechanisms by probe insertion.[19]

Historically, bulk scattering techniques have been used to study macromolecular, biological systems. Among the existing techniques are multiangle light scattering (MALS), which can determine absolute molar mass of macromolecules as well as their root mean squared radii in solution, and dynamic light scattering (DLS) which is used to measure the hydrodynamic radii of macromolecules.[20] In MALS, the scattering intensity of the bulk sample will be directly proportional to the species' mass and the angular dependence provides information on their root mean square radii.[21] By coupling the MALS with size exclusion chromatography (SEC), one can determine absolute mass in real-time.[22] DLS measures fluctuations in light scattering intensity due to Brownian motion and autocorrelation of the intensity trace which can be used to extract the hydrodynamic radii of species present and their diffusion coefficients.[21] These techniques are limited in the fact that they are bulk measurements, and therefore do not provide information on individual molecular behaviour. In recent years, various alternative single molecule imaging techniques based on light scattering have been demonstrated, which overcome some of the difficulties found in fluorescence and bulk scattering.

2.2 Scattering Microscopy

The process of light scattering is not affected by the fundamental limit of fluorescence on number of photons per second, as the number of scattered photons simply scales with the number of incident photons.[23] Theoretically, detection in scattering is therefore only limited by the light intensity that can be directed onto the sample. In practice, however, scattering-based detection has a major disadvantage over fluorescence, which has probably been the main reason for its lower popularity in single molecule studies. While the signal in fluorescence measurements is specifically generated by the fluorophore and the majority of background signal can be suppressed through optical filters, scattered light is produced by any refractive index inhomogeneity, contributing to the detected signal. This makes it crucial for scattering-based single-molecule studies to have a strategy for removal of any unwanted background. The reduced specificity of scattering experiments also makes it better suited for single molecule *in vitro* assays rather than cellular measurements.

Many single molecule *in vitro* experiments operate near a glass-water interface.[24] If one designs the microscope to measure in reflection, light is directed onto such an interface as shown in figure 2.1 and it reflects 0.4% of the incident illumination. The light that is not reflected will then be scattered by any object at the interface with a different refractive index to the surrounding medium, in this case aqueous solution.

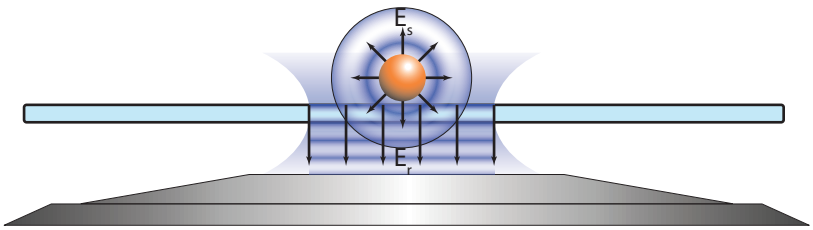


Figure 2.1: Signal detection in scattering microscopy. A microscope objective tightly focuses incident light onto the sample and collects the light reflected, E_r, at the glass coverslip interface and the light scattered by particles, E_s.

The intensity detected by the microscope's camera, I_{det}, depends on the amplitudes of any reference background light, $\mathbf{E}_r$, and the scattered electric field, $\mathbf{E}_s$, as well as their relative phase difference φ in the following way:

$$I_{det} \propto |\mathbf{E}_r + \mathbf{E}_s|^2 = |\mathbf{E}_r|^2 + |\mathbf{E}_s|^2 + 2|\mathbf{E}_r||\mathbf{E}_s| \cos\varphi \tag{2.1}$$

Equation 2.1 shows the three contributions to the detected intensity: the combined reference and background signal $|\mathbf{E}_r|^2$, the scattering signal $|\mathbf{E}_s|^2$, and an interference term $2|\mathbf{E}_r||\mathbf{E}_s| \cos\varphi$. Equation 2.1 suggests two principal ways for optimally detecting scattering signals: removal of background so as to reduce $|\mathbf{E}_r|$ leaving the pure scattering term, $|\mathbf{E}_s|^2$, or making use of a well-defined reference field so as to be able to control the $|\mathbf{E}_r|$ term and use the interference term, $2|\mathbf{E}_r||\mathbf{E}_s| \cos\varphi$ as the signal of interest. These two methods are termed darkfield,[25–27] and interference microscopy, respectively.[28–31]

Darkfield & Interferometric Scattering Microscopies

As early as 1903, scattering has been used as a contrast mechanism to visualise colloidal gold particles.[26] Siedentopf and Zsigmondy used a so-called ultramicroscope to collect light from a sample at a 90° angle from the illuminating beam path, eliminating background illumination.

In modern commercial dark-field microscopes, the illuminating light is usually focused onto the sample through a condenser.[27] The light can then be seamlessly shifted into and away from the detecting optic, through insertion of a stop, blocking the centre of the beam of light and creating a hollow cone of illumination at higher numerical apertures (NA) than the objective can collect. This way the user can easily switch between bright- and dark-field imaging by inserting or removing the stop. Other more recent strategies use laser beams that are coupled into the back focal plane of an objective and illuminate the sample in total internal reflection[32–34] in a manner previously used with total

internal reflection fluorescence microscopy (TIRF).[35] The illuminating beam in these setups is directed into the objective using perforated mirrors[32,33] or micro-mirrors[34] that leave space for the scattering image to be picked up and directed into the imaging path while excluding the illuminating light.

With a mechanism to efficiently remove all background illumination and spurious light, equation 2.1 reduces to:

$$I_{det} \propto |\mathbf{E}_s|^2 = |\mathbf{E}_i|^2 |s|^2 \tag{2.2}$$

where $\mathbf{E}_i$ is the electric field of incident light upon the sample and s is the complex scattering amplitude.

As the scattering intensity is directly proportional to the intensity of the incident light, the signal obtained from objects in dark-field microscopy can be arbitrarily increased through higher incident light intensities. Lasers help in this endeavour as they provide much higher photon fluxes than traditional incoherent light sources.

According to Mie theory,[36,37] in the small particle limit the scattering amplitude s of a spherical particle (diameter $< 1.6\lambda$)[38] scales with the polarisability of the particle, α:

$$\alpha(\lambda) \propto \epsilon_m(\lambda) \frac{D^3}{\lambda^2} \frac{\epsilon_p(\lambda) - \epsilon_m(\lambda)}{\epsilon_p(\lambda) + 2\epsilon_m(\lambda)} \tag{2.3}$$

where ϵ_p and ϵ_m are the complex dielectric constants of the particle and its surrounding medium, respectively, λ is the wavelength of illumination, and D is the particle diameter. As the scattered signal detected depends on the square modulus of the scattering amplitude, the signal scales with D^6. This means that the scattering cross section of a particle decreases rapidly with its size, thereby making it more difficult to distinguish from the background. Following from equations 2.2 and 2.3, a particle that reduces its diameter by half will generate $\frac{1}{64}^{th}$ of the signal.

To maximise the scattering cross section it is common to attach a marker to the molecule of interest that is made from a material with a strong polarisability.[39] Gold nanoparticles have become very popular as molecular probes, due to their large scattering cross section leading to high contrast. This effect is amplified by their surface plasmon resonance.[40] If a gold particle is of a diameter smaller than the wavelength of illuminating light, electrons at their surface are displaced within the gold lattice by the electric field, such that a dipole is generated as shown in figure 2.2.[41] The positively charged ions in the lattice generate a restoring force, making the electrons behave like a harmonic oscillator. The gold particles, therefore, act as 'nano-antennas' with certain resonance frequencies, which depend on the surrounding medium and particle size, and they scatter light strongly at these frequencies.

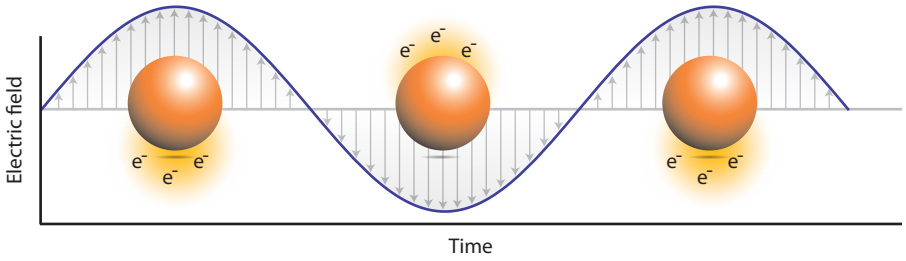


Figure 2.2: Localised surface plasmon resonance in a gold nanoparticle. An oscillating electromagnetic field interacts with the metal nanoparticle, resulting in localised oscillations in the electron cloud density of the particle. Figure adapted from S. Unser, *et al.*, Localized Surface Plasmon Resonance Biosensing: Current Challenges and Approaches, Sensors, 2015, **15**, 1568415716.[41] (licensed under CC BY 4.0)

Darkfield microscopy does have limitations. Due to the ability to increase signal by illuminating with higher light intensities, it is possible to achieve nm spatial precision at µs temporal resolution with modern darkfield setups.[33] In this time regime, however, the Brownian motion of any label around its tether starts to be resolved and the ability to localise the labelled structure may be limited by this effect rather than by the localisation precision for the gold label

itself. Therefore, it should be carefully considered what time scales are relevant for the chosen experiment and the time-averaging window should be as long as possible when following a molecule's motion.[7]

A 40 nm gold particle is still a large marker compared to most fluorescent dyes ($< 1\,\mathrm{nm}$), fluorescent proteins ($\approx 4\,\mathrm{nm}$), or quantum dots ($\approx 10\,\mathrm{nm}$).[6] This may reduce labelling efficiency, introduce significant drag to the system, or otherwise sterically interfere with the system's conformational freedom. In order to minimally perturb the labelled system, it would be desirable to use smaller nanoparticles or image entirely label-free. As discussed earlier, the strong scaling of the scattering signal with size makes it technically very challenging to achieve similar results with smaller nanoparticles.

Interferometric scattering microscopy (iSCAT) helps to circumvent the size-scaling problem and enables high signal-to-noise ratio, non-resonant imaging of smaller sized gold nanoparticles and even direct detection of native, unlabelled biomolecules.[8,42]

If instead of eliminating all background light, one includes a reflection in a controlled manner, so that the $|\mathbf{E}_r|$ term in equation 2.1 is no longer insignificant, $|\mathbf{E}_r|$ can be chosen so that the pure scattering term $|\mathbf{E}_s|$ is now the negligible term for small scatterers. The dominant signal now arises from the interference between background and scattered light with the contrast determined by the ratio of the total detected light and the background reference light:

$$\text{contrast} = \frac{I_{det}}{I_{bkg}} = \frac{|r|^2 + 2|r||s|\cos\varphi}{|r|^2} = 1 + \frac{2|s|\cos\varphi}{|r|} \tag{2.4}$$

where $|r|^2$ is the reflectivity of the interface that provides the reference light.

An obvious choice for the background reference field would be the weak reflection from the glass-water interface mentioned previously. This principle has originally been realised by interference reflection microscopy (IRM)[28] or

reflection interference contrast microscopy (RICM)[29] developed in the 1960's and 1970's. These techniques were originally used to study cell adhesion sites.[43–45] It wasn't until the 1990's and 2000's that interferometric scattering was starting to be used for measurements of nanoscopic size objects,[46] when Amos and Amos (1991) first used confocal scattering microscopy in reflectance mode to image microtubules ($\approx$ 25 nm in diameter) associated to the glass surface (figure 2.3).

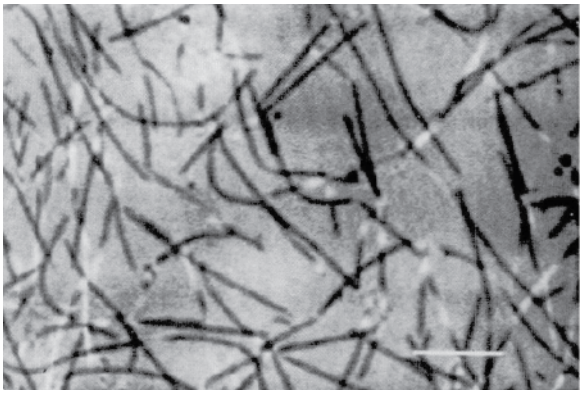


Figure 2.3: Individual microtubules imaged with confocal scattering microscopy in reflectance mode, by Amos and Amos. Scale bar: 4 µm. Adapted with permission from L.A. Amos and W.B. Amos, The bending of sliding microtubules imaged by confocal light microscopy and negative stain electron microscopy, *Journal of cell science. Supplement*, 1991, **14**, 95-101. ©The Company of Biologists Limited 1991[46]

The advent of lasers had finally enabled illumination with high power densities, at the expense of coherent artefacts such as laser speckle or interference fringes. Although nanoscopic particles had been measured successfully with incoherent light sources in both reflection[47] and transmission,[48] the use of this technique with an incoherent light source in this manner has not become common practice. The first laser-based setups were used to take non-fluorescent images of small metallic nanoparticles[49,50] and virus like particles[51] at glass-water interfaces. Later, the technique was termed interferometric scattering microscopy (iSCAT) when detecting single quantum dots[30] and tracking a virus particle diffusing on a lipid bilayer.[31]

The image acquired by the camera on an iSCAT setup is dominated by the reference field $|\mathbf{E}_r|$ (figure 2.4 **a**). However, because this is the reflection from the glass-water interface, it is sample-independent. One can reveal the smaller sample-dependent scattered signal by flat-fielding the image.[53] This is achieved by acquiring a stack of N frames, during which the sample is translated, and dividing each subsequent frame by the invariant median of the acquired stack. This removes all static features, resulting in a flat-fielded image dominated by the scattering signal from the nanoscopic roughness of the clean glass surface (figure 2.4 **b**). From this flat-fielded image, any changing signals smaller than the glass roughness can be revealed through a static background subtraction. For example, figure 2.4 **c** shows a flat-fielded and static-background-subtracted image of microtubules binding to kinesin immobilised on a glass surface. In comparison with figure 2.3, one can see that flat-fielding effectively removes all

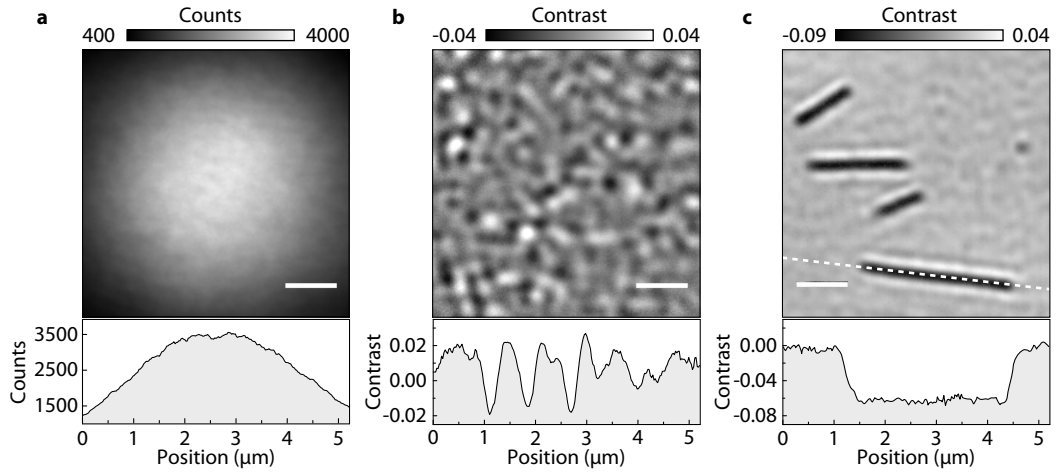


Figure 2.4: **a** Raw iSCAT reflection image of a microscope cover glass covered by water. **b** The same image after division by a median image produced while laterally translating the sample. **c** A flat-fielded and static-background-subtracted iSCAT image of microtubules bound to a glass surface. Scale bars: 1 µm. **a** and **b** are reproduced with permission from D. Cole, *et al.* Label-Free Single-Molecule Imaging with Numerical-Aperture-Shaped Interferometric Scattering Microscopy, *ACS Photonics*, 2017, **4**, 211-216. doi: https://doi.org/10.1021/acsphotonics.6b00912, further permissions related to the material excerpted should be directed to the ACS. Data in **c** is courtesy of Joanna Andrecka.[52]

static features in the background, such as illumination inhomogeneities, and fixed-pattern noise.

The SNR achievable for the 'perfect' iSCAT experiment is limited by shot noise, the Poissonian noise from the random arrival of photons at the detector. The SNR for a shot-noise limited iSCAT experiment scales with the square root of N, the number of photons detected:

$$\mathrm{SNR} = \frac{\text{iSCAT signal}}{\text{background fluctuations}} = \text{contrast}\sqrt{N} \tag{2.5}$$

For a given exposure time, and camera well depth, more photons can be collected per pixel by using higher magnifications than are necessary for adequate sampling of a diffraction-limited point spread function (PSF), and then spatially binning pixels together. Similarly, frames can be averaged together at the expense of time resolution. This increases the SNR to the point at which other noise sources such as mechanical drift begins to average background glass roughness into the image.

The laser intensity used is also limited both by the biological systems' ability to withstand high illumination intensity and the full well capacity of the camera sensor. Higher photon fluxes can be captured on cameras with high full well capacities. However, this approach has its limitations, since most cameras with high full well capacities are expensive and have low quantum efficiencies, making them less efficient for collecting the incident light.[54]

Contrast Enhancement via Numerical Aperture Filtering

An alternative strategy to using a high full well camera would be to increase the contrast of a molecule while capturing the same number of photons, so as not to saturate the detector. This consideration has led to contrast enhancement through numerical aperture filtering.

Examining equation 2.4 demonstrates that the contrast detected on the camera is proportional to the scattering amplitude, $|s|$ and inversely proportional to reflectivity of the glass-water interface, $|r|$. If we could therefore reduce the reflectivity without reducing the efficiency of scattering detection, we could enhance the contrast. Of course the extreme limit of this returns us to darkfield imaging, but partial attenuation of the reference field is possible with numerical aperture filtering.

This reduction in reflectivity is possible by making use of the fact that most of the signal from small scatterers close to the glass-water interface is collected at high numerical apertures by the objective,[55,56] as shown in figure 2.5. By coupling the illumination light into the low NA of the objective, the reference reflection from the glass-water interface will also be localised to the low NA. Then, if one places a partially reflective mirror into the back focal plane of the objective, it will attenuate the low numerical aperture contributions to the image, preferentially attenuating the reference field over the scattered field.

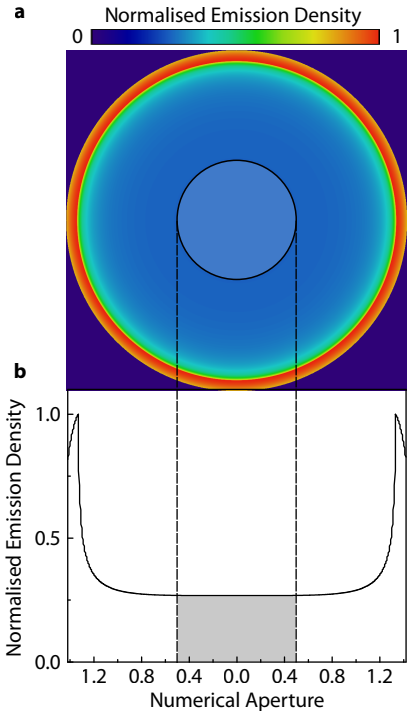


Figure 2.5: The calculated emission pattern of a nanoscopic scatterer at a glass-water interface emerging from the back aperture of a 1.42 NA microscope objective for circularly polarised illumination. The semitransparent circle indicates the region occupied by a partial reflector shown in the schematic experimental setup in figure 3.9. This figure is reproduced with permission from D. Cole, *et al.* Label-Free Single-Molecule Imaging with Numerical-Aperture-Shaped Interferometric Scattering Microscopy, *ACS Photonics*, 2017, **4**, 211-216. doi: https://doi.org/10.1021/acsphotonics.6b00912, further permissions related to the material excerpted should be directed to the ACS.

In this way, the contrast of scattering objects will be selectively enhanced at the expense of the total number of detected photons.[54,57] For example, if a partially reflective mirror reduces the reference light on the camera ($|E_r|^2$) by 100-fold, the reflectivity term ($|r|$) in equation 2.4 will be reduced by 10-fold and therefore lead to a 10-fold increase in contrast, as shown in figure 2.6 as compared to figure 2.4.

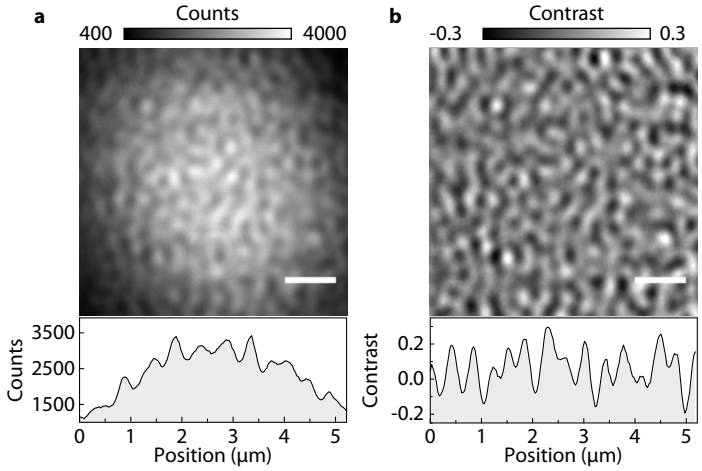


Figure 2.6: Equivalent iSCAT images to figure 2.4 with numerical aperture filtering using a 1% transmissive partial reflector. To generate equivalent images, 100-fold longer exposure time was used. **a** Raw iSCAT reflection image of a microscope cover glass covered by water. The contrast of glass roughness is noticeably enhanced as compared to figure 2.4. **b** The same image after division by a median image produced while laterally translating the sample. Scale bars: 1 µm. **a** and **b** are reproduced with permission from D. Cole, *et al.* Label-Free Single-Molecule Imaging with Numerical-Aperture-Shaped Interferometric Scattering Microscopy, *ACS Photonics*, 2017, **4**, 211-216. doi: https://doi.org/10.1021/acsphotonics.6b00912, further permissions related to the material excerpted should be directed to the ACS.

It is apparent that the procedure does not by itself improve the SNR, due to the decrease of detected photons on the camera. For a 100-fold decrease in incident light on the camera, equation 2.5 shows that the shot-noise-induced background fluctuations for the same exposure time and incident light intensity increases by $\sqrt{100} = 10$, which matches the increase in contrast, as shown above. However, this allows one to increase the illumination intensity accordingly. The major advantage of this strategy is that by using the correct combination

of illumination intensity and transmissivity of the partial mirror, the higher illumination intensity used increases the absolute sensitivity of the microscope. Additionally, the camera used no longer requires a high full well capacity and photons can be captured more efficiently.

Mass Photometry

As equation 2.3 shows, the scattered signal scales with D^3, or in other words the volume of the particle. For particles of different masses but similar refractive indices and densities, their contrasts should thus be directly proportional to their masses. This opens up a new use for an iSCAT microscope as a solution phase mass photometer, an instrument that can measure the mass of macro-molecules in solution.

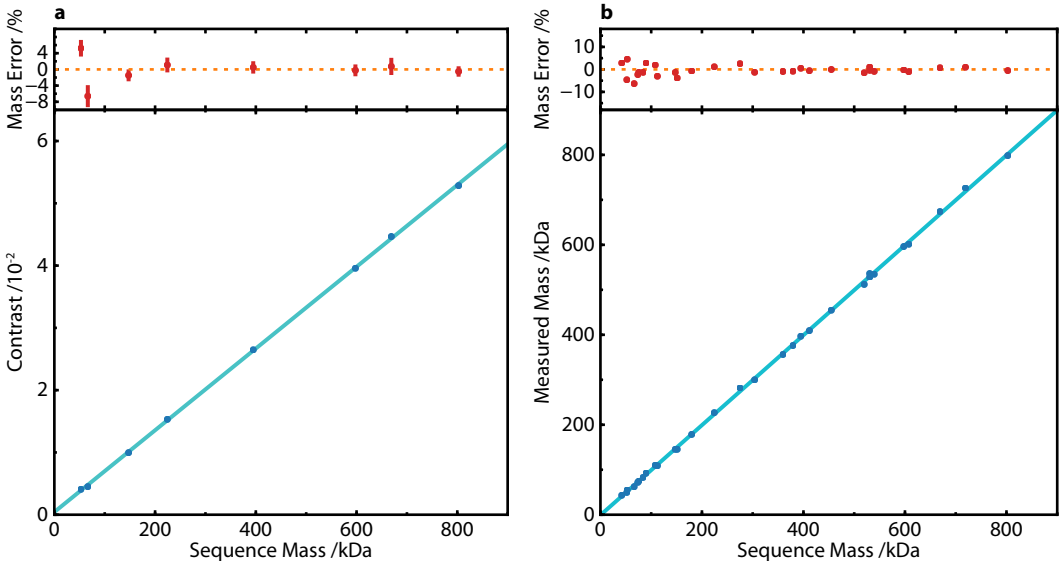


Figure 2.7: a An example mass photometry calibration. Contrast as a function of mass (bottom) for several proteins ranging in mass from 52 to 802 kDa. Mass error (top) is given as a percentage of the sequence mass relative to the given linear fit. Error bars represent standard error of the mean. This figure is adapted with permission from G. Young, *et al.*, Quantitative mass imaging of single biological macromolecules, *Science*, 2018, **360**, 423-427.[8] Reprinted with permission from AAAS. **b** A plot of measured mass vs. sequence mass in mass photometry. Measured mass as a function of mass (bottom) for several proteins ranging in mass from 52 to 802 kDa. Mass error (top) is given as a percentage of the sequence mass relative to the given linear fit. Data collected by Kukura Group, Oxford.

For proteins, the specific volumes of their amino acid sequences and their refractive indices vary only by $\approx 1\%$,[8] suggesting that this linearity between interferometric contrast and mass should hold. A mass photometry measurement of several proteins does in fact yield a linear relationship, as shown in figure 2.7 **a**, and if we take advantage of numerical aperture filtering to boost the sensitivity, proteins as small as 30 kDa can be detected without labels.[58]

To extract the contrasts of the particles from the data, a model point spread function is fitted to the signal of each particle and a histogram of contrasts is plotted, as described in section 3.3. A Gaussian fit of the histogram yields a mean contrast which can be plotted as a function of sequence mass as shown in figure 2.7.

The linear relationship, shown in the data, between interferometric contrast and mass holds between 40 to 1000 kDa, with on average a $\approx 2\%$ deviation of measured mass from sequence mass, as shown in figure 2.7 **b**.[8] The mass resolution, as defined by the standard deviation of the Gaussian fit on the histogram, is $\approx 10\%$ of sequence mass and the precision on a mass photometry experiment, determined by the shot-to-shot repeatability on the mean contrast of the histogram, is $\approx 2\%$ of protein mass. The high accuracy, oligomeric resolution, and high precision demonstrates mass photometry's potential to study biological systems by measuring species' mass in near-native conditions.

Chapter 3
Experimental Design

Parts of this chapter have been adapted from content that will be published in the following invited book chapter:

> Y. Takagi, N. Hundt, A. Fineberg, 'Single-molecule biophysical techniques to study actomyosin force transduction' in *Myosins: A Superfamily of Molecular Motors*, ed. L. M. Coluccio, Springer Netherlands, Dordrecht, 2nd edn., vol. 7 of the Proteins and Cell Regulation series, ch. 6, *submitted.*

The following chapter will discuss the details of the interferometric scattering microscopy (iSCAT) setups developed and used during the course of the work set out in this thesis. We will start with describing a basic setup capable of single particle tracking with high spatial precision and temporal resolution. Secondly, we will also describe modifications to enable both correlative total internal reflection fluorescence (TIRF) microscopy and live bacterial cell imaging. Finally, we will conclude with a description of adapting and increasing the stability of an iSCAT microscope to optimise the sensitivity of mass photometry.

The optical setups described in this section were based on previous designs by Jaime Ortega-Arroyo,[23,53] Gabrielle de Wit,[59] and Daniel Cole.[53,54] I have built and modified these setups entirely myself during the course of the work covered in this thesis. The data acquisition and analysis software used throughout this work was initially developed by Jaime Ortega-Arroyo and Gavin Young, and has been modified by myself. I was responsible for improvements to the iSCAT camera interfacing, full integration of the fluorescence channel into the iSCAT acquisition software, and improvements to the myosin analysis software. The

data acquisition software was written in LabView and the analysis software was written in both LabView and Python. Function fitting, data quantification, and presentation of results was performed by myself in Python.

3.1 Interferometric Scattering Microscopy

The iSCAT Channel

A simple iSCAT microscope can be constructed as shown in figure 3.1.[53] Briefly, a 445 nm diode laser beam is expanded and collimated using two lenses. The beam is then scanned in two dimensions by two orthogonal acousto-optic deflectors (AODs). The deflections generated by the two AODs are scanned in a sawtooth pattern by separate function generators (Rigol DG1022) at 79 and 83 kHz. Both the absolute and relative frequencies are chosen to induce the smallest detectable fluctuations in the background light intensity on the timescale of the camera exposure time. The function generators are synchronised with the exposure of the camera to ensure an integer number of

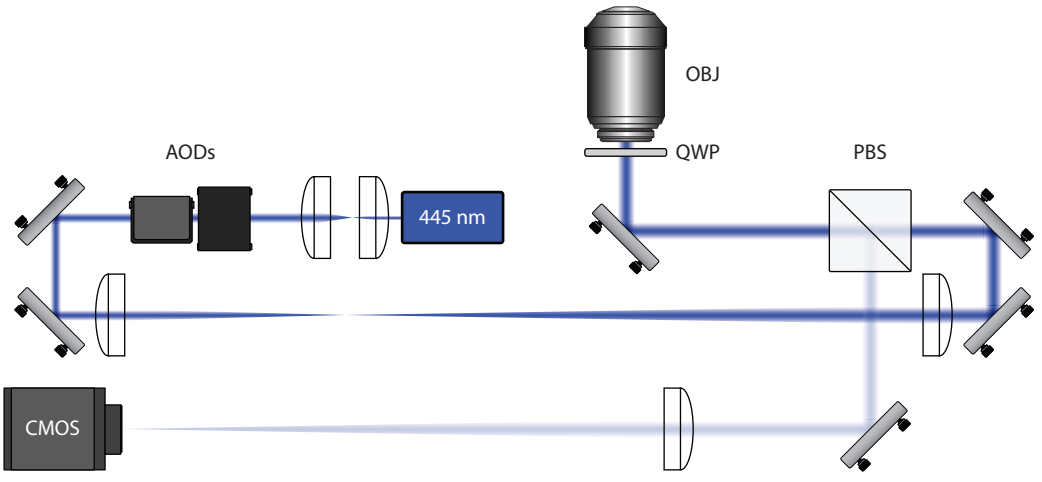


Figure 3.1: A simple iSCAT setup. The scanning pattern of a 445 nm laser generated by two orthogonal acousto-optic deflectors (AODS) is mapped into the back focal plane of a high NA objective (OBJ). The returning light is separated from illumination by a combination of a polarising beam splitter (PBS) and a quarter waveplate (QWP). The signal is imaged onto a CMOS camera.

scans per exposure, and that each iteration of the scan starts at the same point in space. The deflection of the collimated beam is then imaged onto the sample by a 4f telecentric lens system. Before the illumination beam is coupled into the oil immersion 1.42 NA, 60× objective (Olympus PLAPON), it is transmitted through a polarising beam splitter (PBS) and a quarter waveplate (QWP). These two components act as an optical isolator, allowing efficient separation of the illuminated light and the detected interferometric signal as shown in figure 3.2. After a second pass through the QWP, this signal is reflected by the PBS and imaged onto a complementary metal-oxide-semiconductor (CMOS) camera by an appropriate lens.

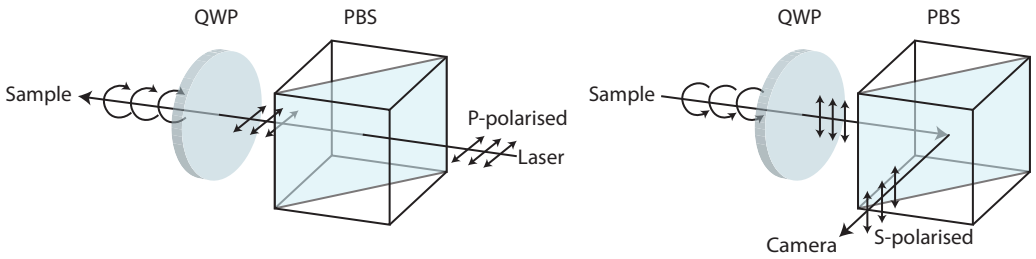


Figure 3.2: A polarisation-dependent optical isolator. (Left) P-polarised light is transmitted by the polarising beam splitter, PBS, and converted to circularly polarised light by the quarter waveplate, QWP. (Right) Reflected light from the sample returns with opposite handed circular polarisation, is converted to s-polarised light by the QWP and reflected by the PBS, effectively separating illumination and detection paths.

Although in reality any wavelength can be chosen for a simple iSCAT setup, a blue wavelength, like 445 nm, is optimal for high sensitivity. This is due in part to the $\frac{1}{\lambda^2}$ dependence of the scattering amplitude (equation 2.3) and in part to the availability of high power blue diodes at this wavelength. Additionally, AOD scanning is not strictly necessary to achieve an iSCAT image. Simple Köhler illumination, with a Gaussian beam input, can provide a Gaussian shaped sample illumination with a full width at half maximum between 1 to 20 µm depending on the required power density and field of view.

Beam scanning allows for higher instantaneous power density whilst retaining a large field of view as one is scanning a diffraction-limited beam over the sample. AOD scanning also suppresses the diffraction patterns generated by scattering objects as the scatterers 'see' different parts of the spatially-coherent beam at different times during a single exposure. This provides a flatter image with high sensitivity and adjustable field of view.

In order for there to be interference between the reference and scattering signals, the chosen laser light source must have a coherence length longer than the optical path difference between the two signals. However, care should be taken because if the coherence length of the laser used is too long, back reflections from the various optics in the beam path will introduce further interferences and the image quality will degrade. For this work, diode lasers with a coherence length between 30 to 100 µm have been used.

Several factors must be considered when choosing a detector for iSCAT microscopy. As mentioned in the previous chapter, the useable illumination intensity is limited by the full well of the camera pixels. Therefore, a sensor with high full well and fast readout capabilities would be ideal for a simple iSCAT setup. Unfortunately, this often comes at the expense of quantum efficiency and pixel fill factor, so a compromise must be found. Complementary metal-oxide-semiconductor (CMOS) sensors are a suitable candidate to meet this compromise of requirements and have been used throughout this work.

Focus Stabilisation

In order to maintain focus during acquisition we implemented a simple focus stabilisation protocol as shown in figure 3.3.[53] Briefly, a 405 nm laser beam is expanded to a size comparable to or bigger than the diameter of the microscope

objective's back focal plane, which can be calculated using the formula:

$$d_{BFP} = \frac{2fNA}{M}; \quad \text{with} \quad NA = n\sin(\theta) \tag{3.1}$$

where f is the tube length of the objective, NA is the numerical aperture of the objective, M is the magnification of the objective, n is the refractive index of the medium in which the lens is working (immersion oil in this case) and θ is the maximal half-angle of the cone of light that can enter or exit the objective.

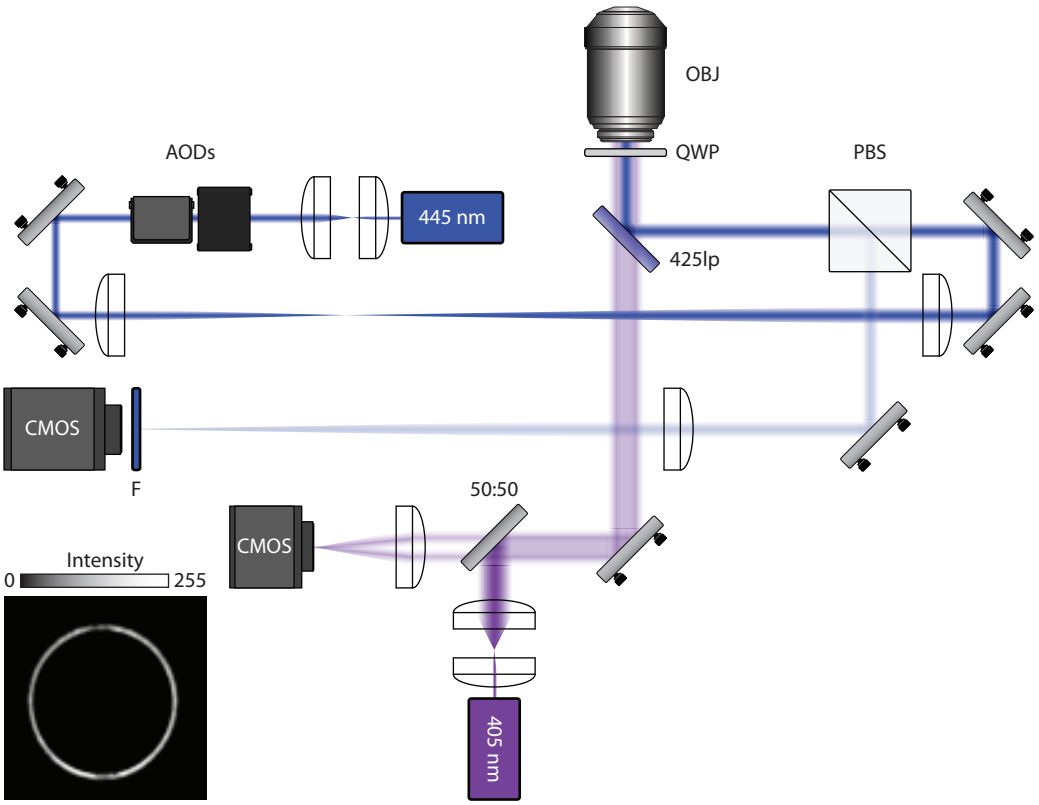


Figure 3.3: A simple iSCAT with focus stabilisation. For focus stabilisation, a 405 nm laser is expanded and coupled into the objective by a 425 nm long-pass dichroic mirror. The returning ring-shaped beam (inset) is separated from the illumination by a 50:50 beamsplitter and imaged onto a CMOS camera.

The 405 nm beam is then coupled into the iSCAT channel with a 50:50 beam splitter and a 425 nm long-pass dichroic mirror. The large beam overfills the back aperture of the objective and whilst light at the low NA of the back focal plane of the objective is transmitted and lost, the light at the high NA,

i.e. the periphery of back focal plane, is focused onto the sample at an angle greater than the critical angle for the glass - water interface and is totally internally reflected back to form a ring. As figure 3.4 shows, the ring diameter depends on the focus position of the sample because the distance between the coverslip and the objective determines the position of the reflection relative to the back aperture of the objective.

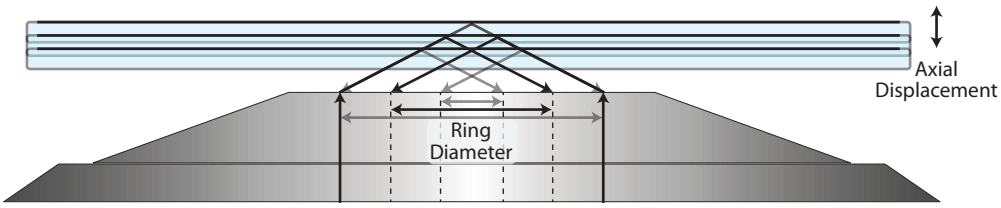


Figure 3.4: Ray tracing diagram of focus stabilisation mechanism. The incoming light rays at the periphery of the back focal plane of the objective are totally internally reflected at the glass - water interface. Should the axial displacement of the coverslip change, the lateral position of the totally internally reflected beam changes with respect to the back focal plane of the objective. Therefore there is a change in ring diameter. An active feedback loop can then signal a piezo electric stage to adjust sample height and correct ring diameter.

This ring is then separated from the iSCAT channel by the dichroic mirror, and half the ring's intensity is transmitted through the 50:50 beam splitter and imaged onto a CMOS camera. Software analysis of the ring actively fits its diameter, and using an active feedback loop adjusts the sample height using a piezo electric stage to maintain ring diameter and therefore focus to within a few nanometres precision. To reduce any interaction with the sample, low power ($\approx 0.1\,\mathrm{mW}$) is used.

3.2 Correlative iSCAT and Fluorescence

Fluorescence Channel

For correlative fluorescence and iSCAT imaging it is preferable to use a red wavelength for the iSCAT channel, for example 660 nm, in order that the high

laser intensities do not bleach the fluorophores used. A blue excitation laser will then provide a fluorescence detection window in the green region, ideal for molecules labelled with GFP or green emission quantum dots.

A fluorescence channel can be coupled into the iSCAT setup through addition of further dichroic mirrors, as shown in figure 3.5.

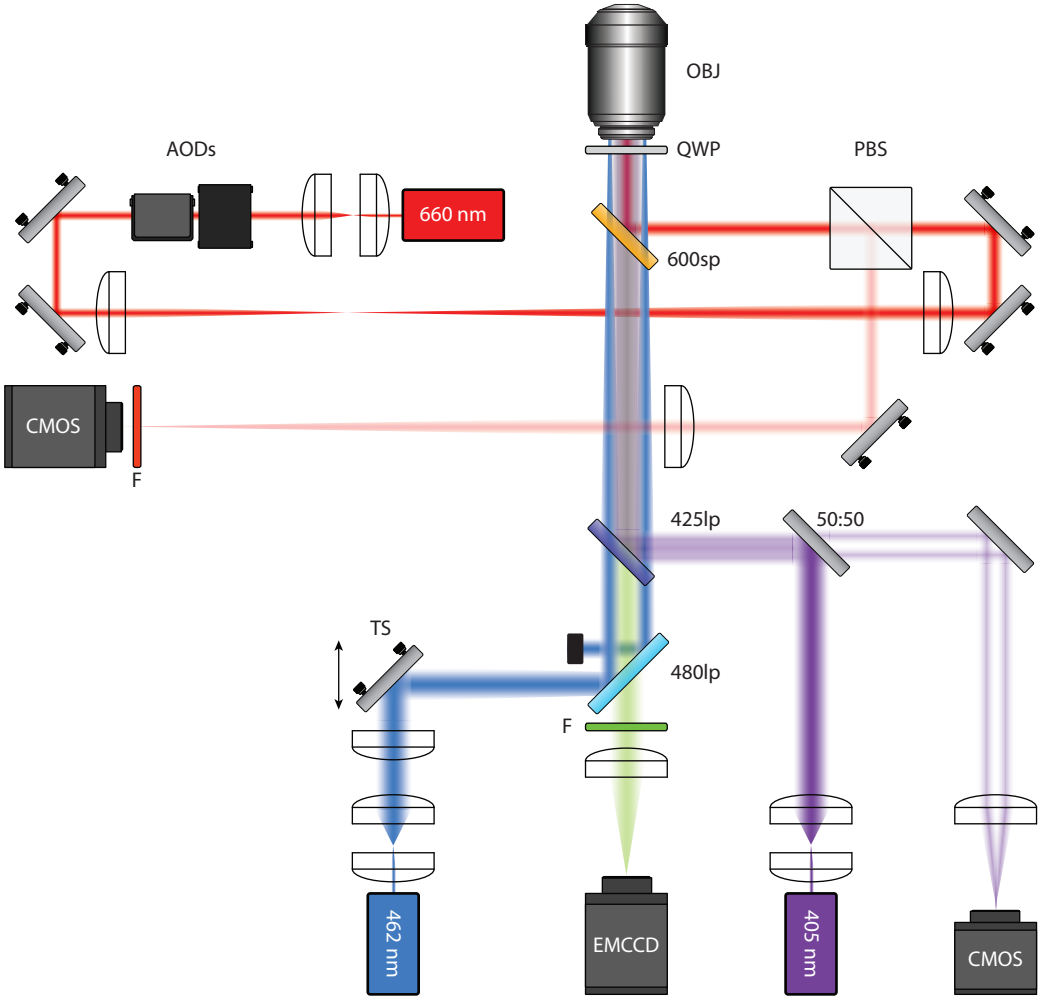


Figure 3.5: A correlative iSCAT and fluorescence setup. Starting with 660 nm iSCAT setup in the same configuration as figure 3.3, a 462 nm laser is focused into the periphery of the back focal plane of the objective, so that the beam is totally internally reflected at the sample. The returning beam is sent to a beam block. A 600 nm shortpass dichroic mirror separates the iSCAT and fluorescence channels. The fluorescence emission is separated from the illumination by a 480 nm longpass dichroic mirror. A green bandpass filter ensures no stray light is imaged onto the EMCCD with the fluorescence emission.

Briefly, a 462 nm laser is focused through a 500 mm lens into the back focal plane of the objective, steered by a mirror and 480 nm long-pass dichroic. The beam's position can be displaced laterally by mounting the mirror onto a translation stage in order to switch between epi-illumination and TIRF. A 425 nm long-pass and a 600 nm short-pass dichroic mirror couple the iSCAT, focus stabilisation and fluorescence channels. The red-shifted fluorescence emission is separated from the other channels by the 480 long-pass dichroic, and the image is passed through a filter and is focused onto an electron multiplying charge-coupled device (EMCCD).

To ensure temporal synchronisation between the two channels when simultaneously acquiring images, a trigger is used to signal the start of acquisition to the two cameras. This can be achieved either through a hardware trigger, like an electrical signal sent from one camera to another, or a trigger built into the software so that acquisition programme ensures both cameras are exposed simultaneously. Due to difficulties arising from interfacing the two brands of camera used for the iSCAT and fluorescence channels, we opt to use a software trigger. Software triggers can be less reliable than hardware triggers due to delays in propagating the signal through the computer to the cameras. To test whether a software trigger would in fact provide sufficient temporal synchronicity, the Gaussian beam of the iSCAT channel is scanned in a one dimensional sinusoidal wave across a sample and the illumination profile recorded in both channels. In order to achieve sufficient 'bleed through' from the iSCAT channel onto the fluorescence camera, the fluorescence filter is removed.

The movies of the scanning beam in each channel are smoothed by convolution with a Gaussian kernel and the centres of the beams are determined and tracked using an analytic, non-iterative calculation of the best-fit radial

symmetry centre.[60] The centres of the beam in each image along the direction of travel are then plotted versus time and a sinusoidal curve is fitted to each using the function: $f(x) = A\sin(\omega x + \varphi) + c$, where A is the amplitude, ω the angular frequency (2πf), φ is the phase and c is a constant offset. To calculate the time delay between the two channels, the phase difference between the two curves is calculated. It is important to compare the measured frequencies and ensure they are identical within the error of the measurement.

We achieved a time delay of 8.55 µs, a value well below the time resolution required for the planned experiments in this work, which is on the order of a few milliseconds. We can therefore conclude that software triggering provides sufficient temporal synchronicity between the iSCAT and fluorescence cameras for the experiments in this work.

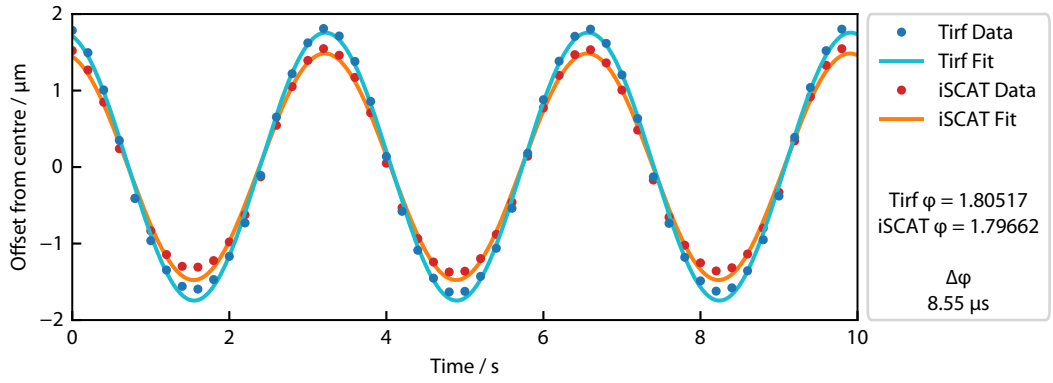


Figure 3.6: A plot of time vs. displacement of a beam in both channels. The phase difference between the two sinusoidal fits gives the time delay between the two cameras' exposure.

Image Registration

To accurately correlate the resulting iSCAT and fluorescence images, an image registration algorithm is required. To achieve this, a fluorescent fiducial marker large enough to give a sufficient scattering signal is used. TetraSpek™ microspheres (0.1 µm, Thermo Fisher), are an ideal candidate for this, due to

their large size and their broad spectrum of possible absorption and emission wavelengths. Alternatively, gold nanoparticles do also fluoresce and can be used, however high laser intensity in the TIRF channel is required.

To create an accurate image registration, a global transform model estimation is used.[61] Briefly, a sample of Tetraspek™ microspheres are allowed to non-specifically bind to a glass coverslip to give a sparse coverage and an iSCAT and TIRF image taken simultaneously. A simple candidate search can be run on each image by taking pixel values over a user-set threshold and running a local maxima search within a given window size. The candidate search is improved in reliability by first convolving the images with a Gaussian kernel in order to smooth out local high frequency noise. Each resulting raw point spread function from the candidate search is then fit with a standard 2D Gaussian function to accurately determine the centre coordinates of each particle. A map of the particle centres in each image is generated with the TIRF map being scaled by the expected magnification ratio between the two channels. A set of trial parameters that map the TIRF coordinates onto the iSCAT coordinates are optimised using the Levenberg-Marquardt algorithm. The parameters applied are a rotation about the origin ($\mathbf{R}_\theta$), translations ($\mathbf{T_x}$ and $\mathbf{T_y}$), and uniform scaling ($\mathbf{S_x}$ and $\mathbf{S_y}$). Although one could allow the centre of rotation to also be optimised, for the data taken in this work it is not necessary. The optimised parameters can then be used to map any TIRF coordinates onto the iSCAT coordinates, for accurate image registration with particle distances varying by $\approx 2.7 \pm 1.45$ nm as shown in figure 3.7.

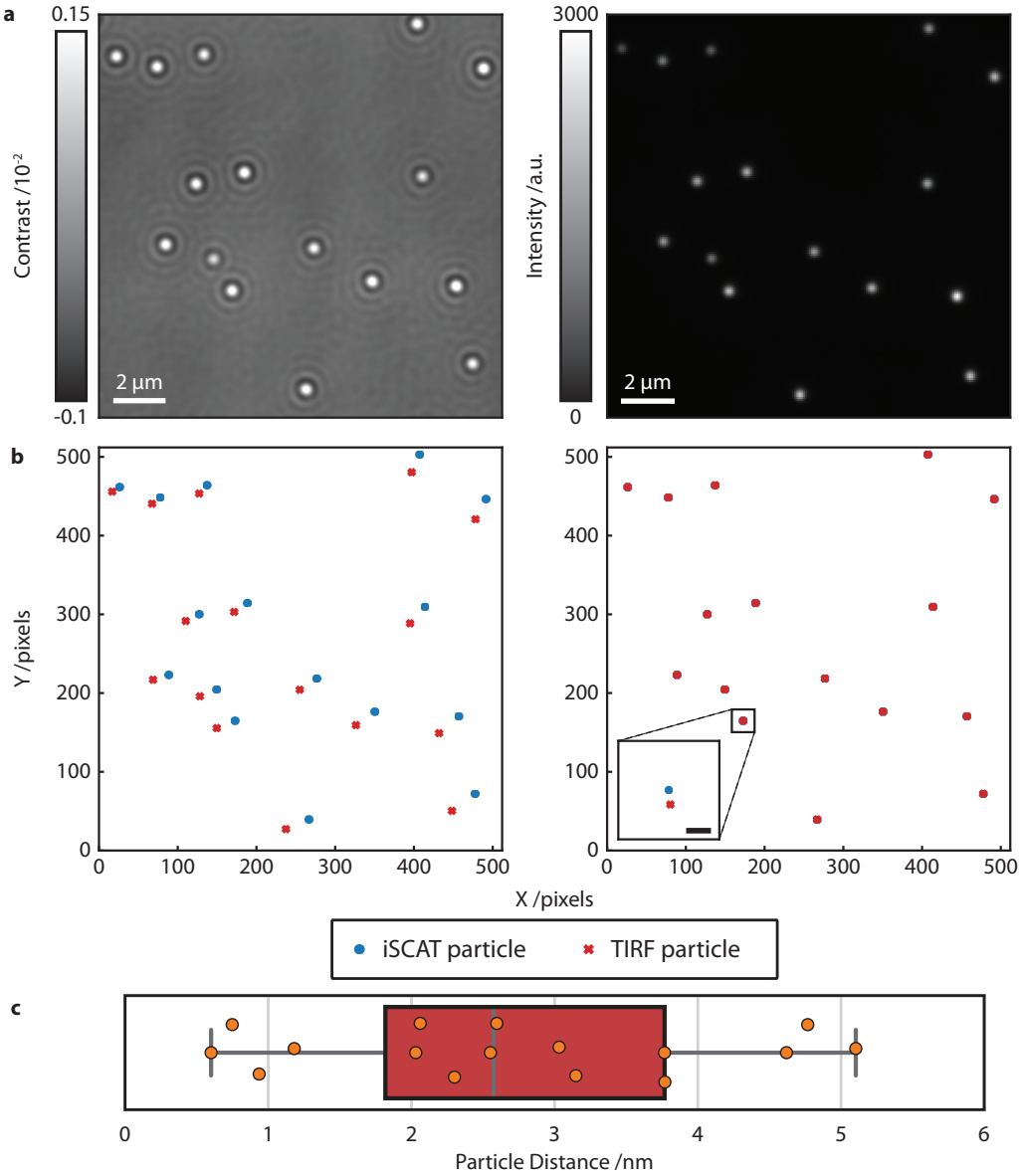


Figure 3.7: Image registration between iSCAT and fluorescence channels. **a** An array of 100 nm fluorescent beads are imaged in iSCAT (left) and fluorescence (right). **b** The centres of the particles are plotted (left) and the transformation to map one onto the other is calculated, resulting in a registered image of coordinates (right). The inset shows a zoomed-in view of a single bead in both channels after registration. Scale bar: 0.05 pixels. **c** A box plot of distances between centres of beads after image registration. Mean distance between the channels = 2.7 ± 1.45 nm.

iSCAT for Photosensitive Systems

As mentioned previously, the scattering signal increases for shorter wavelengths of light. However some systems, such as bacterial cells, are photosensitive and therefore there is a trade-off between sensitivity to small scattering objects and phototoxicity to the sample. Certain modifications can be made to an iSCAT setup in order to make it more applicable to photosensitive samples as shown in figure 3.8.

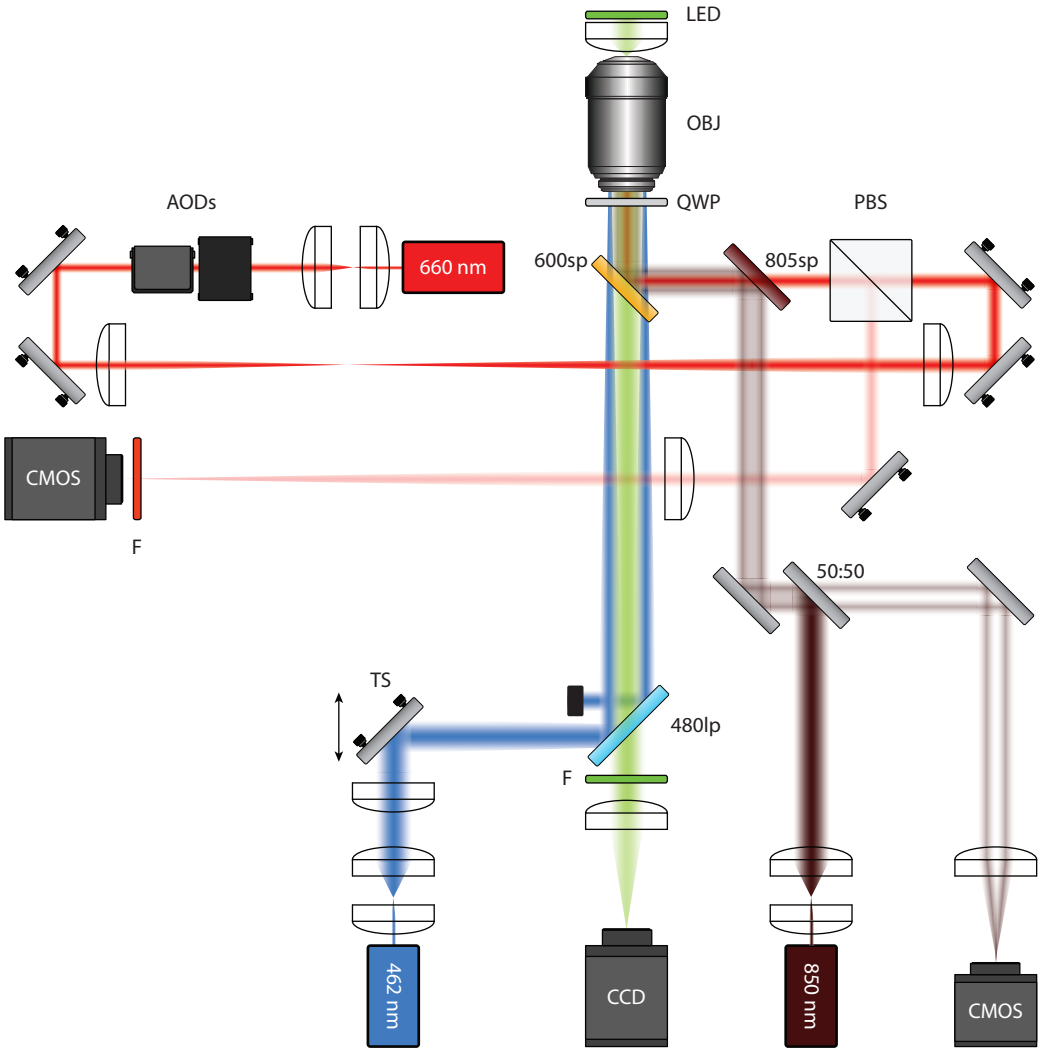


Figure 3.8: An iSCAT setup with correlative fluorescence adapted to photosensitive systems. To reduce heating effects a red iSCAT channel is used, as is an infrared focus stabilisation laser. A light emitting diode (LED) is coupled into the objective in transmission to image large bodies in the sample without high illumination.

As with correlative iSCAT and fluorescence, using a red wavelength for iSCAT will minimise the energy transferred to the sample. For the focus stabilisation channel, an infrared wavelength with low power ($\approx 0.1\,\mathrm{mW}$) is used to reduce any heating effects or interactions this laser may have when focused onto the sample. In addition, a shutter can be installed into the beam path so as to only illuminate the sample during acquisition. If large features, like bacterial cells, are imaged, a brightfield illumination module can be aligned in transmission. A white light emitting diode (LED) is focused onto the sample from above and the resulting brightfield image is detected through the already aligned fluorescence channel. This eases the process of finding a region of the sample to image without exposing it to the relatively high laser intensities required for iSCAT.

3.3 iSCAT for Mass Photometry

To increase the sensitivity of the microscope, so that it is capable of mass photometry experiments to detect small proteins with high mass resolution, numerical aperture filtering (as described in chapter 2.2) can be introduced. By adding a second 4f telecentric lens system to the detection arm of the beam path, an image of the back focal plane of the objective is formed in the detection pathway. A window with a thin layer of silver coated onto its centre can be slotted into this plane to attenuate the reflected reference light, enhancing the contrast as described in section 2.2.

The diameter of this partial reflector (PR) should be carefully chosen taking into account the size of the illumination beam, the size of the objective's back aperture (equation 3.1), and the magnification and NA of the objective. Typically, a diameter of 2 to 3 mm is used.

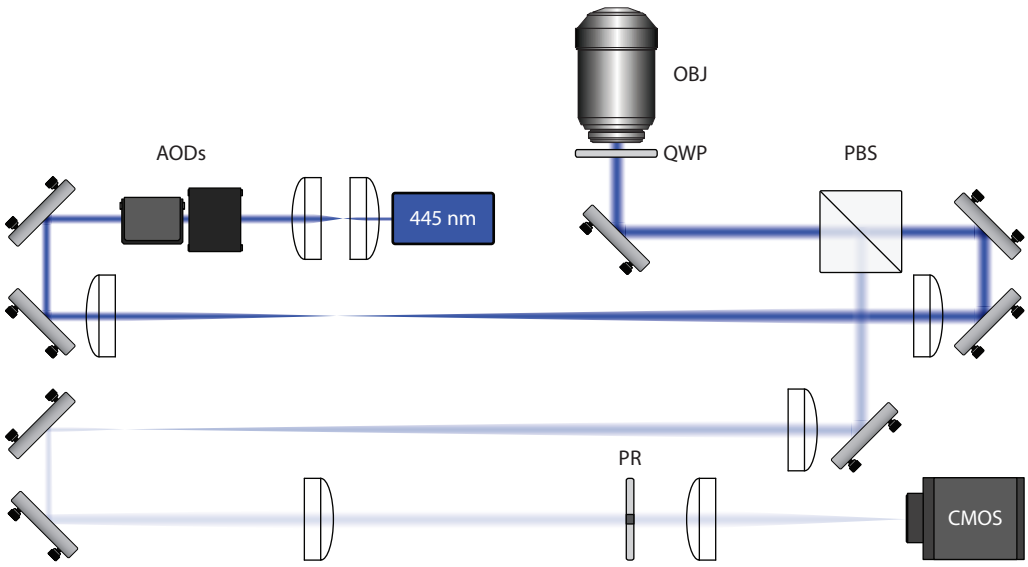


Figure 3.9: A numerical aperture filtered iSCAT microscope for mass photometry. A 4f telecentric lens system is introduced into the detection pathway and a partially reflective mirror (PR) is placed in the Fourier plane. This attenuates the reflected reference field without attenuating the scattering signal, enhancing contrast.

Image Processing and Particle Detection

To extract the contrasts of the particles from the data, a different image processing procedure is used from the flat-fielding mentioned above as described by Young *et al.* (2018). Briefly, to remove the static scattering background from the glass surface, ratiometric images, R, were calculated as:

$$R = \frac{N_{m+1}}{N_m} - 1 \tag{3.2}$$

where N_m and N_{m+1} are consecutive normalised averages of several images, as shown in figure 3.10 **a** (blue and red). Each frame stack is normalised by the mean pixel value to reduce the effects of slow laser fluctuations. The processing is then stepped through the raw movie, frame-by-frame, to produce a ratiometric movie as shown in 3.10 **b**. A binding event appears in the ratiometric movie as a PSF which increases in contrast and decreases as the midpoint of the two frame stacks approaches and then moves past the time at which the protein binds. This processing method has an advantage over

the flat-fielding method mentioned previously because here, the background is continuously updated when the averaged frame stacks step through the movie, making it resistant to the long term fluctuations in background. However, this method can only be applied because a landing event occurs on a timescale shorter than the averaged window and the particle does not move after binding. By changing the averaged window size one can improve the signal to noise ratio (as shown in equation 2.5), however if a large window size is used, too many particles will be present in the resulting frame and their contrasts can not be extracted due to their PSFs overlapping.

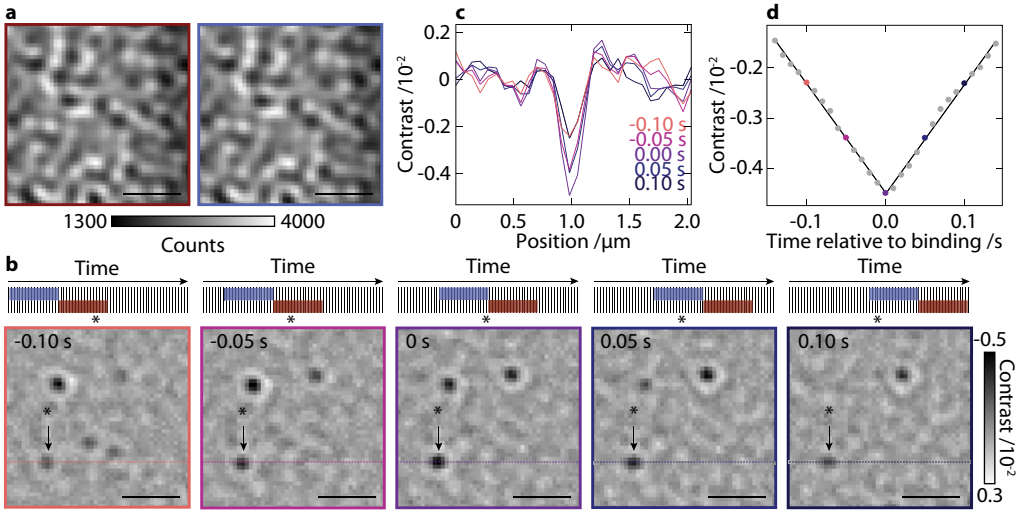


Figure 3.10: Image processing and analysis sequence for mass photometry. **a** Raw images before and after the landing event in **b-d** showing image contrast due to coverslip roughness. **b** Illustration of the differential imaging approach. The asterisk marks a landing event. Individual images are averaged into two consecutive blocks (blue and red), which are normalised and divided to provide differential contrast. The mid-point is scanned in time, meaning that the signal from stochastic landing events grows and fades, as indicated by the black arrow. Scale bars: 1 µm. **c** Corresponding cross-sections for the particle highlighted in **b**. **d** Corresponding signal magnitudes extracted by a fit to the PSF and fit (black). This figure is adapted with permission from G. Young, *et al.*, Quantitative mass imaging of single biological macromolecules, *Science*, 2018, **360**, 423-427.[8] Reprinted with permission from AAAS.

Particles are identified in each frame of the ratiometric movie by an automated spot detection routine.[62] Briefly, the ratiometric frame is convolved with an experimentally measured PSF, and a particle probability image is

calculated. Pixels with particle probability > 0.3 that also corresponded to a local maximum in the convolved image were taken as candidate particles. This value was chosen as the lowest value which gave few false positive results in a reference buffer solution. Normally, the number of false positives is not that sensitive to this parameter (± 0.05), however if there is a transient increase in mechanical noise, due to sample drift or environmental vibrations, then this parameter is crucial in ensuring the results are not affected. An 11×11 pixel^2 region of interest around each particle is fitted with a model point spread function to extract the particle contrast. This size was chosen as it effectively samples the extent of the PSF which is modelled without causing the process to become computationally cumbersome. Eccentric PSFs were rejected as not arising from a single binding event. This is determined from the ratio of the larger to smaller standard deviations from the fit (σ_x and σ_y) and rejecting if it is below 0.7, a value chosen to reject obviously non-spherical signals.

As mentioned previously, a single molecule landing at the glass surface results in a signal that appears in several consecutive frames of the ratiometric movie with increasing then decreasing contrast. To extract the most accurate measure of the particle contrast and to avoid over-counting particles, the fits were grouped based on spatial and temporal location in the ratiometric movie. Fits were classified as arising from one particle if they were within 1 pixel of each other and if they were in a frame within a window size of twice the temporal frame averaging window. The linear increase and decrease of the particle contrast as the sliding window moves past the landing event are then fit with a pair of straight lines with gradients of equal magnitude but opposite sign (figure 3.10 **d**), and the peak contrast taken to be the best estimate of the true particle contrast. If a particle distance threshold greater than 1 pixel is used, neighbouring particles become grouped as one and the two linear fits fail

due to the two changes of contrast being out of phase with each other.

3.4 Microscope Stabilisation

In order to remain in the shot noise limited regime for as long as possible, any mechanical sources of noise must be suppressed to prevent the coverslip roughness from being averaged into the background, as shown in figure 3.11.

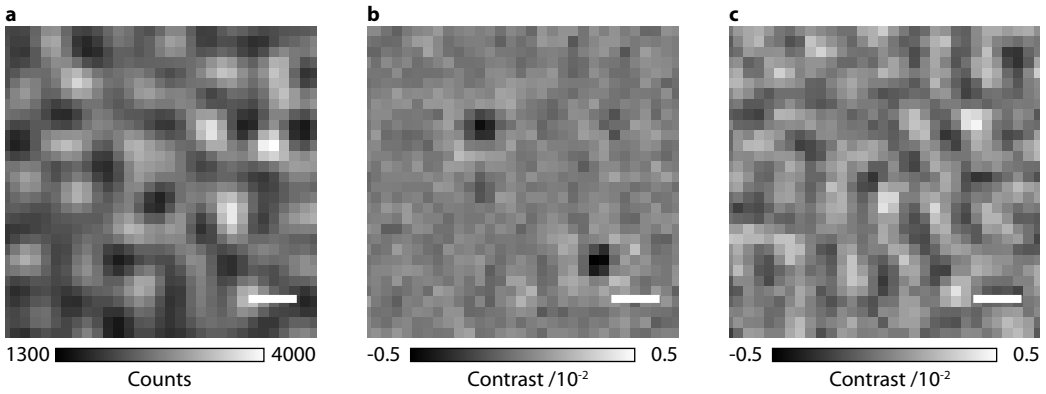


Figure 3.11: An example of mechanical drift being averaged into a ratiometric image. **a** A raw image showing image contrast due to coverslip roughness. **b** A single frame from a ratiometric movie showing landing events. **c** A single frame from the same ratiometric movie during a short period of high mechanical noise showing the coverslip roughness being averaged into the frame. Scale bars: 1 µm.

Vibrations coupling into the setup contribute to laser beam pointing and sample drift, and degrade the image stability over time. To reduce this the beam path length can be shortened and all components mounted onto a single, thick, heavy piece of metal as shown in figure 3.12. By incorporating walls around this, the components are sealed inside a metal box reducing airflow and dampening vibrations. This ensures that all components of the microscope are both mechanically and thermally coupled to each other.

An easy way of shortening the beam path, besides using shorter focal length lenses, is to move the 4f telescope after the polarising beam splitter in the illumination path as shown in figure 3.13. Now, if a partial reflector is required, a second 4f need not be introduced to create an image of the back focal plane

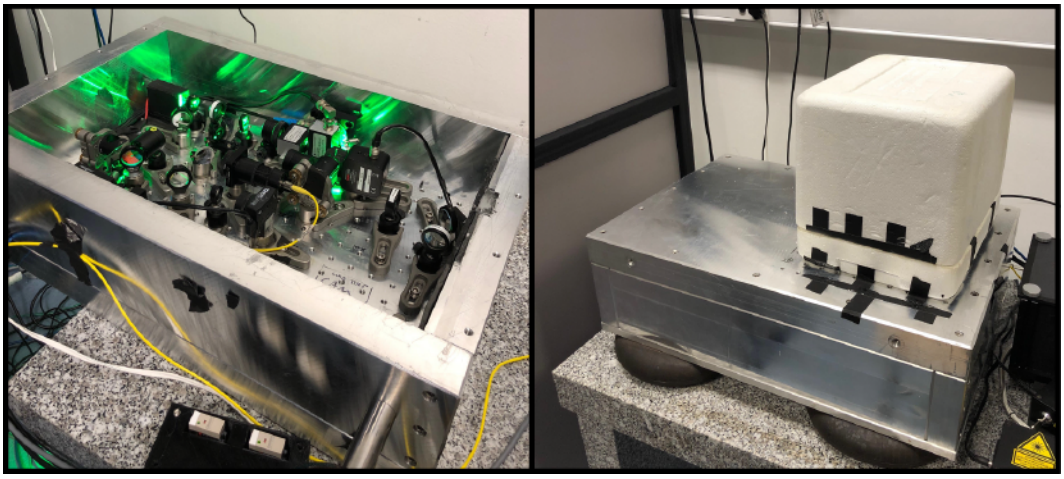


Figure 3.12: An iSCAT setup optimised for stability. (Left) The inside of an iSCAT setup that has been mounted onto a single, thick, heavy piece of metal. (Right) The finished iSCAT microscope fully enclosed inside a metal box. A polystyrene box has been fixed around the sample to reduce air currents to the sample.

in the detection pathway. Reducing the number of adjustable mirror mounts to just two ensures long term stability, keeping alignment changes due to thermal fluctuations to a minimum.

Another consideration, particularly for the blue wavelengths, is the high laser intensity required at the sample. As discussed previously, the higher the illumination intensity, the larger the scattering signal from small scatterers. This, however, could lead to damage to the objective over extended continuous use. To prevent such damage, a fail-safe shutter can be introduced into the beam path. This approach also provides the benefit of making the microscope a class I laser device, by simply having the shutter close when the objective is open to the surroundings.

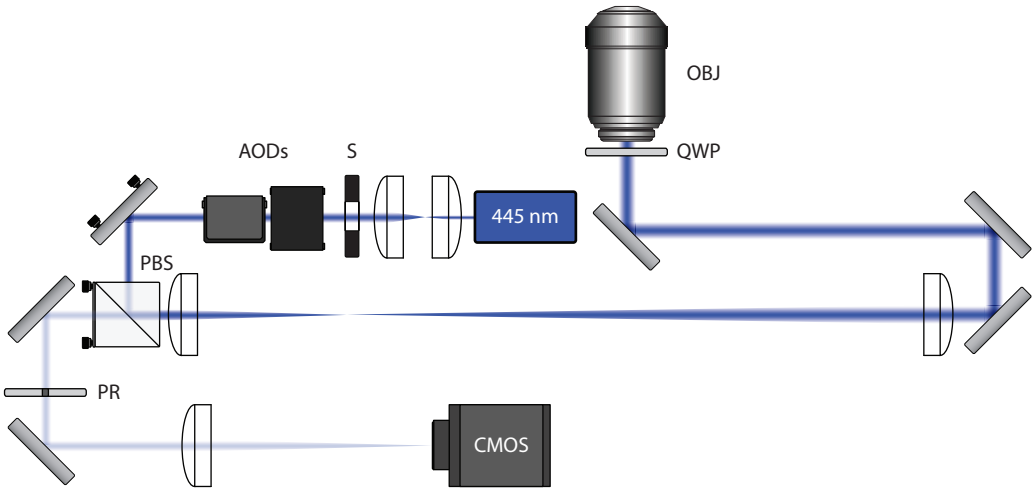


Figure 3.13: A compact iSCAT setup for mass photometry. Introduction of a shutter helps reduce the high intensity laser from damaging the objective over prolonged use. A single 4f telecentric lens system is used with both the illumination and detection reducing beam path length. The short beam path then allows this setup to be mounted inside a small, heavy, sealed metal box for stability.

Chapter 4

Structural Coupling in Myosin 5a

Parts of this chapter are adapted with permission from:

> J. Andrecka*, J. Ortega Arroyo*, Y. Takagi, G. de Wit, A. Fineberg, L. MacKinnon, G. Young, J. R. Sellers and P. Kukura, Structural dynamics of myosin 5 during processive motion revealed by interferometric scattering microscopy, eLife, 2015, **4**, 05413.[63]

Parts of this chapter have been adapted from content that will be published in the following invited book chapter:

> Y. Takagi, N. Hundt, A. Fineberg, 'Single-molecule biophysical techniques to study actomyosin force transduction' in *Myosins: A Superfamily of Molecular Motors*, ed. L. M. Coluccio, Springer Netherlands, Dordrecht, 2nd edn., vol. 7 of the Proteins and Cell Regulation series, ch.6, *submitted.*

The motor domain, lever arm, and stalk tracking data in this chapter were acquired by myself. Joanna Andrecka acquired the dual labelled motor domain - stalk labelled data. Optical setups used were built by Gabrielle de Wit and myself. The particle tracking software was created by Jaime Ortega-Arroyo and modified by myself.

4.1 Introduction

Myosin 5a (M5a) is a cytoskeletal molecular motor protein that transports cargo inside cells through translocation of its motor domains along actin filaments.[64,65] It has long been known that M5a strides in a hand-over-hand fashion, with an individual step size of 37 nm.[66–69] The mechanism with which M5a moves

is processive, in that a single protein undergoes several catalytic cycles and consequently takes several steps once attached to actin without dissociating.[70]

There are four major structural domains to the M5a homodimer: the motor domain, the lever arm, the stalk domain, and a globular tail, as shown in figure 4.1. Towards the N-terminus of the molecule are the actin binding site and the nucleotide binding site on the motor domain,[71,72] followed by the α-helical lever arm.[73] The lever arm consists of six IQ calmodulin binding motifs and extends 24 nm.[67,74,75] This is significantly longer than many other types of Myosin, and is thought to be the main reason for M5a's relatively large step size.[76–78] The monomers dimerise at the coiled-coil stalk region, which ends with a globular tail at the C-terminus, where cargo binding occurs via multimerisation with other adapter proteins.[79]

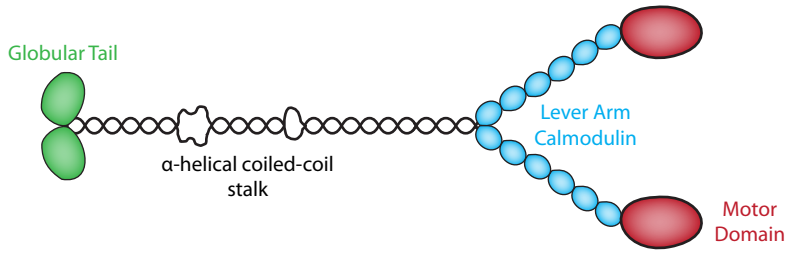


Figure 4.1: Domain structure of Myosin 5a. At the N-terminus, the motor domain contains the actin-binding site and nucleotide-binding site, followed by an ≈24 nm long lever arm that binds six calmodulins. The stalk region of M5a contains three stretches of α-helical coiled-coil, that are interrupted by two major regions of non-coiled-coil. At the C-terminus, the globular tail binds adapter proteins that link it to cargo. This figure is adapted with permission from K. M. Trybus, Myosin V from head to tail, *Cellular and Molecular Life Sciences*, 2008, **65**, 1378-1389. ©Springer Nature 2008[64]

The work discussed in this chapter uses a M5a construct with the coiled-coil stalk region truncated at amino-acid 1104. Figure 4.2 highlights the different domains of the construct used and the standard nomenclature in the myosin field. A step is defined as the distance between the two actin bound motor domains, typically 37 nm.[67–69,80] A stride is used to refer to the translocation

of the trailing motor domain before it rebinds to the actin as the new leading motor domain, a distance twice the step size.

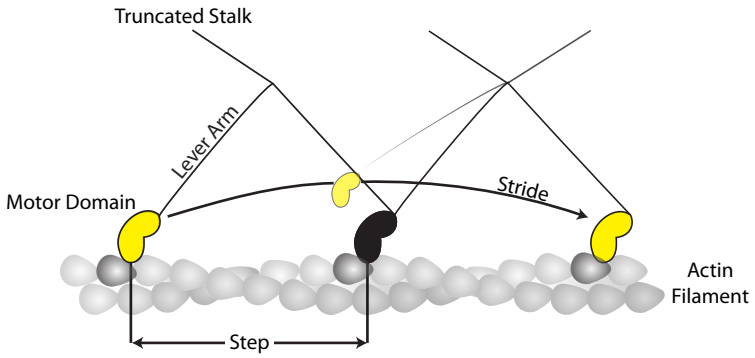


Figure 4.2: The definition of a step and a stride of Myosin 5a. A step is the distance between the two actin bound motor domains, a stride is the movement of the trailing motor domain to its new position on the actin as the leading motor domain. The construct shown is a schematic of that used in this work, with a truncation in the coiled-coil region.

The catalytic cycle of M5a during each stride is summarised in figure 4.3. When in its waiting state (A), M5a has both motor domains strongly bound to actin. Upon the rate limiting release of ADP from the trailing motor domain ($12\ s^{-1}$), it becomes weakly bound to actin and ATP can bind (B), ATP binding ($0.9\ \mu M^{-1}\ s^{-1}$) releases the trailing motor domain and forms a transient one motor domain bound state (C). The leading motor domain and lever arm then undergoes a 'powerstroke' in which the trailing motor domain translocates 74 nm to a position 37 nm in front of the other motor domain. ATP is then hydrolysed (D) and the motor domain becomes weakly bound to actin as the new leading motor domain, (E). After phosphate release the myosin motor domain re-enters a strongly bound state (A) and thus the mechanism can repeat in a processive manner.[67,81] Through coordination of the chemical cycles and the mechanical action of the domains of the protein, M5a can efficiently move along the actin filament.

Studies using optical trapping[70,82–85] or fluorescence microscopy,[66,86–90] have

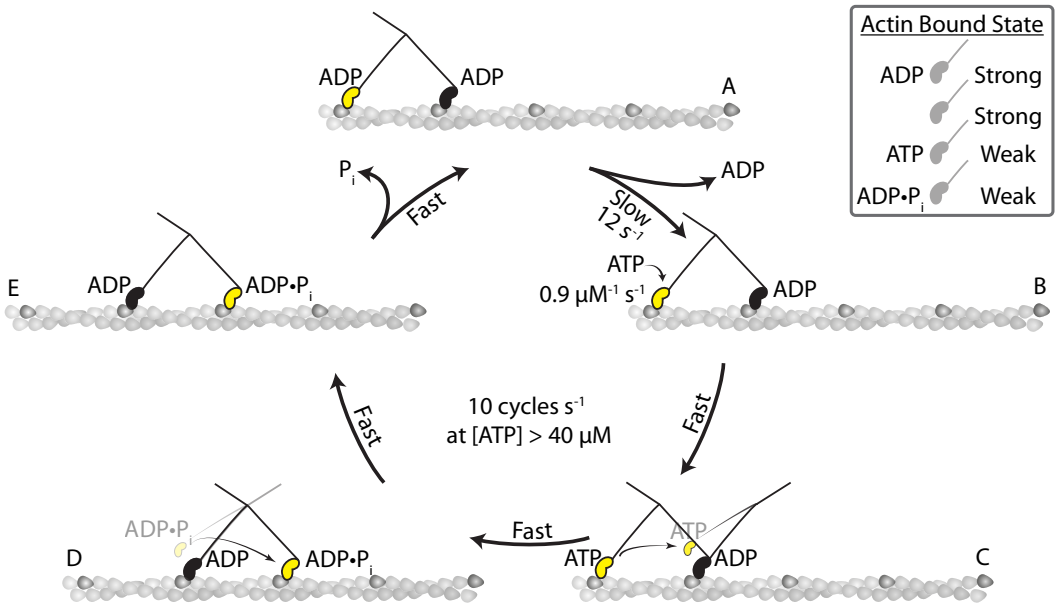


Figure 4.3: The kinetic cycle for Myosin 5a. The cycle completes 10 times s^{-1} at saturating ATP concentrations ([ATP] $>$ 40 µM). The inset identifies the actin binding state of the motor domain for different bound nucleotide species. This figure is reproduced with permission from R. D. Vale, Myosin V motor proteins: Marching stepwise towards a mechanism, *Journal of Cell Biology*, 2003, **163**, 445-450. ©Rockefeller University Press 2003[67]

attempted to produce a model to explain the dynamics and geometry of the unbound motor domain during the powerstroke. All models produced are comprised of a forward powerstroke followed by a Brownian search to find the next binding site.[71,85,90–92] In addition, high speed atomic force microscopy (AFM) experiments,[78,93] such as those by Kodera *et al.*,[94] have observed the newly binding leading motor domain to rapidly detach again, in a phenomenon that is termed a 'foot stomp'.

However, previous work by Andrecka *et al.*[63] has used iSCAT to localise the motor domain during a processive run of M5a, with a localisation precision of $<$ 4 nm at an imaging speed of 1000 frames/s and $<$ 1-2 nm at 100 frames/s. The study showed that during the stride, the detached motor domain occupies a constrained transient state approximately 40 nm to one side of the actin filament and around 24 $\pm$ 10 nm above, evidence that is contrary to the

idea of a free Brownian search.[85,91,95,96] This observation would suggest that there is more conformational rigidity within the M5a molecule than previously thought, and could provide a reason for the high directionality of M5a. The transient state was reproducibly observed in the majority of strides, being missed only when the dwell time in the transient dipped below the experiment's frame rate. It is also worth noting that very few ($\approx$ 3% of all strides at 1 µM ATP, $\approx$ 0.6% at 10 µM ATP and none at saturating ATP) of these 'foot stomp' events were observed in the iSCAT experiments with the motor domains remaining firmly bound to actin during the mechanochemical cycle, irrespective of whether the motor domain is leading or trailing. The observation of Kodera *et al.*,[94] of an increased occurrence of lead motor domain detachment and reattachment in their AFM studies, may have been due to a significantly lower ATP concentration or the non-negligible interaction of the AFM tip with the motor.

The iSCAT study also observed a conformational change at the motor domain of the leading motor during the powerstroke, allowing for the build up of tension in the leading motor domain for the next powerstroke to occur. This is a previously unobserved transition, formerly inferred only from structural simulation studies for myosins. It corresponds to a rotation at the N-terminus, showing a connection between the N-terminus and the lever arm. The observed N-terminus domain movement could thus be a signature of the release of strain within the molecule. This conformational change appears critical for the rearrangement of the nucleotide binding pocket and/or closure of the internal cleft, which would then allow for finalising the actomyosin energy transduction. This result also demonstrated that iSCAT is capable of showing incredibly small conformational changes in the motor domain (< 1 nm), as well as large (10s of nm) steps of M5a.

Through observations from simultaneous iSCAT and fluorescence measurements of the two motor domains, the position of the transient state together with what appears to be constrained diffusion suggests that myosin side steps along actin in a combined twisting and leaning motion, much more like a drawing compass rather than a freely jointed swivel or human-like gait, as shown in figure 4.4. In hindsight, such a mechanism has numerous advantages over a search based on full rotational diffusion. It generates a built-in bias for finding the correct binding site and ensures that the motor domain needs to travel and search only along one dimension to find the desired binding site defined by the torsion about the leading motor domain and neck linker, rather than a lower probability three-dimensional Brownian search. Even if the motor domain fails to bind strongly on first passage, it swings back and forth between the transient state and the desired actin site, until tight binding can occur. This suggests that the structure of myosin 5a facilitates and controls the motion of the unbound motor domain to achieve such high specificity in finding the desired binding site. Recent work by Ramaiya *et al.*[97] has shown a similar compass-like rotational model for kinesin-1 by coupling a birefringent bead to the kinesin and imaging with polarisation microscopy. The compass-like rotations observed for M5a and kinesin-1 allows for the fact that this may be a mechanism employed by processive motor proteins to ensure efficient movement.

To further understand how M5a structure facilitates the motions and mechanics discussed above, the work in this chapter was carried out by focusing on the other domains of the molecule and correlating them with the motor domain, in order to build a geometric picture of M5a's motion.

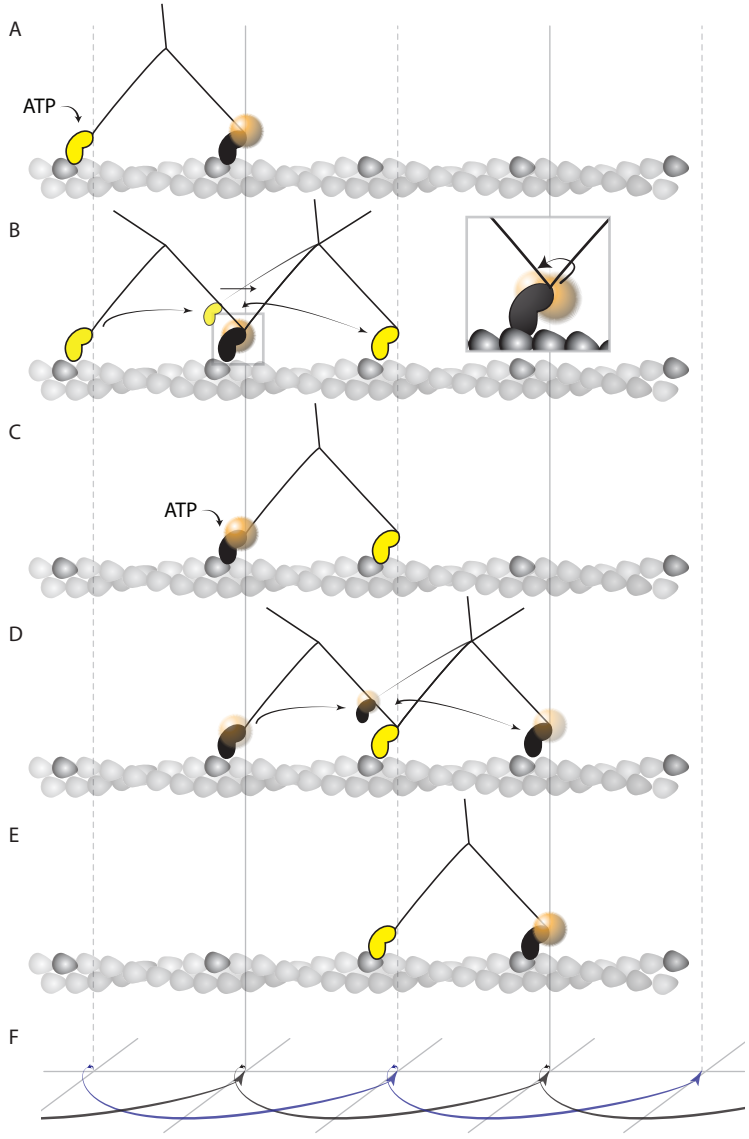


Figure 4.4: Current mechanism of the myosin step. **A** ATP binding to the trailing head (yellow) and its detachment releases strain stored in the molecule. **B** The bound head (black with a gold nanoparticle attached) performs its power stroke which is accompanied by the conformational transition (inset). The labelled head becomes a new trailing head **C** which detaches after ATP binding. **D** It moves forward in a partially twisting motion and occupies an off axis position (transient state). From this position, the head binds the desired binding site while ATP hydrolyses. **E** The step completes as the head binds actin and is repeated by the other head in the same direction dictated by the initial torsional strain. **F** Schematic representation of both heads' movement (lateral projection). Figure adapted from J. Andrecka, *et al.*, Structural dynamics of myosin 5 during processive motion revealed by interferometric scattering microscopy, eLife, 2015, **4**, 5413. (licensed under CC0 1.0)

4.2 Methods

Sample Preparation

The following sample preparation was carried out by myself with the exception of the globular actin preparation, the production of the truncated myosin construct, and the preparation of the biotinylated calmodulin. These were provided by the J. R. Sellers group at the NHLBI, NIH, Maryland.

Rabbit skeletal muscle actin was prepared as described[98] and stored in liquid nitrogen as globular actin (G-actin), until used. A 20 µM filamentous actin (F-actin) stock solution was prepared in polymerisation buffer (10 mM imidazole, 50 mM KCl, 1 mM $MgCl_2$, 1 mM EGTA (pH 7.3) containing 1.7 mM DTT, 3 mM ATP). Actin was diluted in motility buffer (MB; 20 mM MOPS pH 7.3, 5 mM $MgCl_2$, 0.1 mM EGTA) 20 times. Mouse myosin 5a heavy meromyosin (HMM) with a C-terminal eGFP (enhanced green fluorecent protein) was expressed in the presence of calmodulin (CaM) and purified as described.[99] In addition, the N-terminus was modified by the addition of a nucleotide sequence encoding an AviTag peptide (GLNDIFEAQKIEWHE) for site-specific biotinylation with BirA ligase (Avidity, Aurora, Colorado), and the coiled-coil stalk region truncated at amino-acid 1104, terminated in an eGFP molecule. After biotinylation, the sample was aliquoted, flash frozen in 20 µl drops and stored at −80 °C. Before labelling, the myosin sample was diluted in MB containing 40 mM KCl, 5 mM DTT, 0.1 mg ml^{-1} BSA and 5 µM calmodulin.

For motor domain labelled samples, gold nanoparticles of 20 nm in diameter conjugated with streptavidin were purchased from BBI (UK) and directly mixed with biotinylated M5a sample in a 4:1, gold to myosin ratio, consistent with one or zero myosin molecules per gold particle. The mixture was incubated on ice for at least 15 min (sample volume 50 µl, final concentration of myosin 300 pM).

The same procedure was used for double gold/Qdot labelling. The quantum dots (emission maximum 565) conjugated with anti-mouse IgG were purchased from Invitrogen (Lifetechnologies, UK). The myosin was first conjugated with a mouse anti-GFP antibody, allowing the Qdot conjugate to bind.

Lever arm labelled samples were prepared as described.[100] Briefly, CaM with a Q135C mutation was biotinylated by transferring into biotinylation buffer (5 mM $CaCl_2$, 20 mM imidazole; pH 7.5) using a Micro Bio-Spin 6 buffer exchange column and diluted to a final protein concentration of $6.7\,\mathrm{mg\,ml^{-1}}$. Biotin-maleimide was added to a final concentration of 0.5 mM, the mixture was incubated for 1 h at 22 °C and then dialysed against dialysis buffer (0.5 M DTT, 0.5 M EGTA, 10 mM imidazole; pH 7.5) overnight at 4 °C. The biotinylated CaM (biotCaM) was aliquoted and stored at −80 °C.

A mixture of wild type and biotCaM in exchange buffer (25 mM imidazole pH 7.5, 25 mM KCl, 4 mM $MgCl_2$) was made, with a final concentration of 0.75 µM each. This was incubated in a 10:1 biotin to myosin ratio for 2 minutes at 20 °C, and $CaCl_2$ was added to a final concentration of 1 mM and incubated for 5 minutes at 20 °C. Afterwards, the mixture was quenched with EGTA at a final concentration of 8 mM. The myosin - biotCaM conjugate was then incubated with 20 nm gold nanoparticles as above.

For stalk labelled samples, a non-biotinylated M5a sample was mixed with anti-GFP antibody in a 3:1 ratio in MB. The antibody conjugated myosin was then mixed with 20 nm gold nanoparticles in a 4:1 gold to myosin ratio. The mixture was incubated on ice for at least 15 min (sample volume 50 µl, final concentration of myosin 300 pM).

The flow cell used to create an actin network, and in which to measure the motility assay, was prepared as described.[100] It was first rinsed with $1\,\mathrm{mg\,ml^{-1}}$ solution of poly(ethylene glycol)-poly-l-lysine (PEG-PLL) branch

copolymer (Surface Solutions SuSoS, Switzerland) in PBS and incubated for 30 min at 20 °C. Next, it was washed twice with MB before adding the actin solution. After 5 min of incubation, the chamber was washed with MB and the surface was blocked by adding 1 mg ml^{-1} BSA in MB. Finally, the chamber was inspected and myosin-gold conjugate solution containing ATP was added to a final concentration of 10 µM. This concentration is below saturating ATP concentrations (40 µM) to prolong dwell times after each step. All assays were performed at 20 °C.

Experimental Setup Details

The correlative iSCAT and fluorescence setup is adapted from that described previously.[59] The layout of the experimental setup used is detailed in section 3.2.

For iSCAT, a 662 nm diode laser (Coherent Obis) is used with a 2 mm beam diameter, under filling the back aperture of the objective to generate a focal spot of ≈ 1 µm. A Photonfocus (MV-D1024-160-CL-8) (CMOS) camera was used with a pixel size of 10.6 µm with an imaging lens of 750 mm. The effective magnification was 250× and pixel size was 42.4 nm px^{-1}.

For TIRF, a 462 nm diode laser (Lasertack) is used. The beam is focused onto the back focal plane with a 400 mm lens, to generate a wide-field illumination spot with FWHM of ≈ 15 µm. The beam is reflected off both a 505 nm long-pass and a 605 nm long-pass dichroic mirror, which passes the 662 nm beam so that both beams are overlapped, when entering the objective. Fluorescence in the 505 to 605 nm window is separated from both the reflected 662 nm beam and 473 nm beams by the two dichroic mirrors and, after passing through a 550 nm long-pass filter, is imaged onto an EMCCD camera (Andor iXon X3 860) with a pixel size of 24 µm using a 750 mm lens. The effective

magnification was 250× and pixel size was 96 nm px^{-1}.

Localisation precisions for each tracking experiment are quoted in the results section as the standard deviation of localisations when the molecule is in the two motor bound state. It is worth noting that the actual localisation precision of the experiments is around 1 nm, as measured on static beads bound to the glass surface. Any value quoted higher than this is due to the Brownian motion of the particle.

Image Processing

Sample-specific images with shot-noise limited sensitivity were obtained by flat fielding the image as described in section 2.2. The flat field reference image was produced by first recording 2000 images while moving the sample stage with a piezo-driven XY translation stage. The resulting image stack was temporally averaged to 100 frames and each pixel of the flat field reference image was computed as the temporal median value of the frame sequence. Each frame of the acquired movie was then divided by this reference image. Removal of sample specific constant background, thereby increasing the image signal to noise ratio, was achieved by obtaining the static background from the sample. This was achieved by averaging at least 10 frames that lacked a signal from the processive myosin 5a molecule labelled with a gold nanoparticle of interest. Localisation of labelled myosin 5a in each frame was achieved by non-linear least square fitting of the point spread function to a two-dimensional Gaussian and then 2D trajectories constructed across the movie.

Data Analysis

For the distance vs. time traces, the centre of the first dwell period of the labelled head was subtracted from all localisations of the particle to provide

a zero point reference. Localisation precision was calculated by taking the standard deviation of the particle position during a stationary dwell state.

For the 2D density estimate of the lever arm data, the dwell states of the lever arm were isolated from the distance-time traces and split into times before and after the small forward motion was observed. The centres of the localisations before the forward step were aligned on top of each other and a 2D contour plot was calculated.

For the 2D density estimate of stalk localisations, individual strides were isolated from the distance-time traces by taking 20 data points from the dwell states before and after the stride. Each trace is separated into time points before, during and after the stride and then oriented along the x-axis by fitting a line through the centres of the dwell states, before and after the stride. The strides were then rescaled to the zero reference, again by subtracting the centre of the first dwell state from subsequent strides and a 2D contour plot was calculated.

The dwell times of the transient states of both the stalk and motor domain were fit with an exponential equation corrected for instrument dead time (t_0), the time taken to acquire a single frame at the slowest fame rate used (500 Hz). This corrects for potential under-sampling of short lived states.

$$f(t) = ke^{-k(t-t_0)}; \quad \tau = \frac{1}{k} \tag{4.1}$$

4.3 Results and Discussion

The experiments detailed in this chapter require a label to be attached to different domains of M5a in order to accurately localise them throughout a processive run. For this work, gold nanoparticles were used in iSCAT tracking experiments due to their high scattering cross section, as discussed in section

2.2. To limit any possible hindrance to the movement of M5a, we used 20 nm particles, the smallest size without reducing our localisation precision due to low SNR. For fluorescence measurements, Qdots were used due to their large fluorescence signal, ease of conjugation to the myosin through surface modification, and reduced tendency to bleach as compared to fluorescent dye molecules or proteins.

Lever Arm Experiments

Labelling Considerations

The labelling of the lever arm, by substituting a labelled calmodulin, poses a problem in that it is possible that the introduction of a label would hinder the movement of the myosin molecule. In order to successfully label the CaM, it must first be biotinylated which requires a mutation to the amino acid sequence to introduce a cystein at the required labelling site (position 135 Q →C (Q143C)). This calmodulin mutation follows a precedent first executed by Churchman *et al.*[101] for CaM-labelling with fluorescent Cy3 and Cy5-maleimide dyes for M5a tracking by single-molecule high-resolution colocalisation. Dunn and Spudich[71] used the same CaM mutant for a biotin-maleimide reaction to provide an attachment point for streptavidin-coated 40 nm gold nanoparticles for M5a tracking via darkfield light scattering. The site was determined to be (1) surface and thus solvent accessible, (2) unlikely to create structural conflict with the motor domain, (3) distant from the acto-myosin binding site and (4) reasonably distant from any CaM-CaM interaction regions. Due to these assumptions, we implicitly assumed that the motile properties of myosin 5a with the mutant CaM bound will be unchanged.

Dunn and Spudich[71] tracked the lever arm of M5a using darkfield microscopy observing typical processive movement with a 40 nm gold nanoparticle attached

to the lever arm. This indicates that our use of 20 nm gold nanoparticles should also not be considered to overly influence the molecules' movements and we can assume that the motile properties of myosin 5a will be unchanged.

Lever Arm Localisation

By labelling calmodulin with 20 nm gold nanoparticles and allowing for free exchange of the labelled subunits with the unlabelled subunits on the lever, we can track the position of the lever arm as a function of time at an imaging speed of 100 frames/s. Our localisation precision of the particle was on the order of

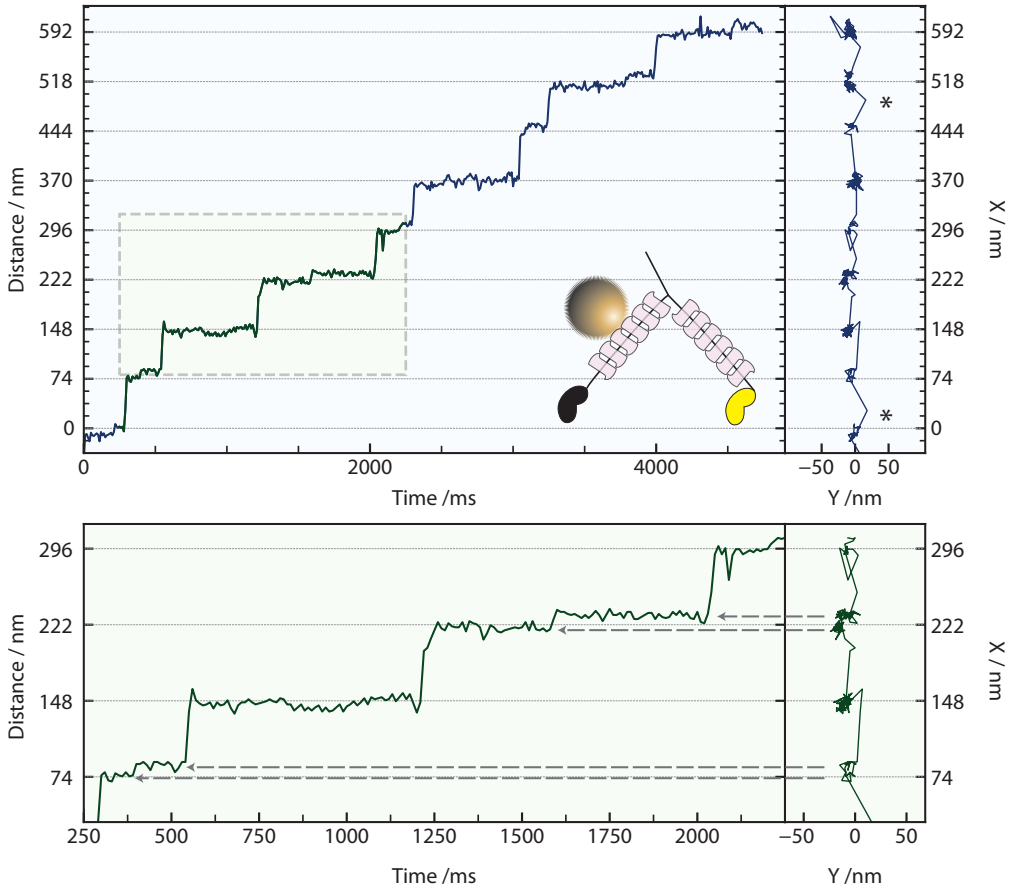


Figure 4.5: A typical trace from a lever arm tracking experiment (top). The asterisks denote instances where the motor domain was occupying the transient side state reported in Andrecka *et al.* (2015). (Bottom) An enlarged segment of the trace with the small forward step marked to show the point where the unlabelled lever arm steps forward.

≈ 3 nm at this imaging speed. We observed two distinct particle displacements during a processive run of lever arm labelled M5a, 58.5 ± 0.31 nm and 16.6 ± 0.71 nm (S.E.M.), corresponding to the labelled lever arm and the unlabelled lever arm translocating respectively (figure 4.5). The average displacement after both the labelled and unlabelled lever arm have translocated is 75.2 ± 0.49 nm, in keeping with the literature value of ≈ 74 nm. It should also be noted that similar to the motor domain experiments reported by Andrecka *et al.*[63] we observe a transient state with the lever arm, denoted by an asterisk in figure 4.5, with similar frequencies of occurrence at 100 frames/s imaging speed.

To further investigate the particle's trajectory during the smaller displacement, a 2D density estimate of particle localisations can be plotted as shown in figure 4.6. Whilst the unlabelled lever arms moves, the label on the other lever arm also moves forward, along the actin filament and 6.65 ± 0.46 nm laterally to the actin filament.

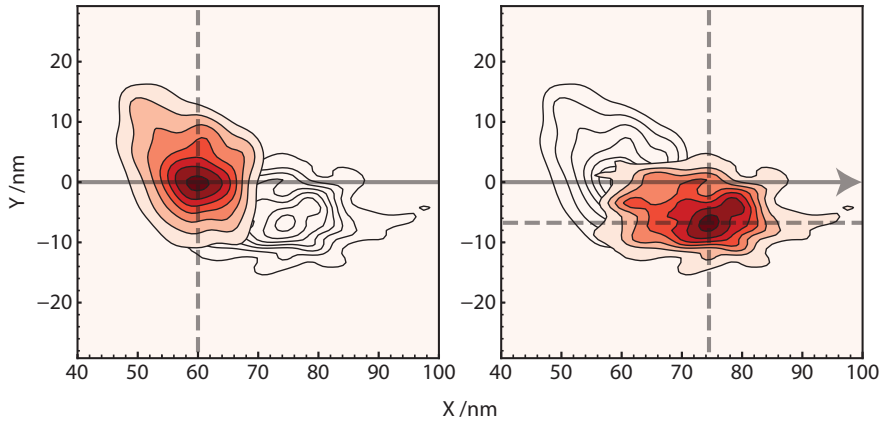


Figure 4.6: A 2D density estimate of lever arm label localisations before (left) and after (right) the unlabelled lever arm steps. The arrow denotes the direction of travel along the actin filament. Sample size: 12 traces giving 28 steps.

The forward movement indicates that the lever arm swings forward as it transitions from the leading state to the trailing state, pre-powerstroke. The

lateral movement suggests that we are able to see some rotational movement of the labelled lever arm as the unlabelled lever arm moves, something which has not been probed to date. The step sizes in the data shown here suggest that the labelled CaM unit is that closest to the motor domain, since the step size is close to that expected for the motor domain. If a CaM unit further up the lever arm were to be the one that was labelled, one would expect a smaller first step and larger second step, similar in size to each other.

Stalk Domain Experiments

Labelling Considerations

Labelling the stalk domain of our M5a construct involves conjugating a scattering label to the eGFP via either one or two antibodies. One would not consider this to be a hindrance to the motion of M5a, as the wild-type protein would bind cargo at the globular tail for transport of vescicles. The 20 nm gold nanoparticles and Qdots that we conjugate to the molecule are significantly smaller than the vesicles that wild-type M5a would be transporting inside the cell.[102]

Stalk Domain Localisation

To further probe conformational changes in M5a, we also labelled the truncated stalk domain with a 20 nm gold nanoparticle and tracked it at imaging speeds of either 500 or 1000 frames/s. Our localisation precision of the particle was on the order of ≈ 6 nm at these imaging speeds. We observed that at the beginning of each stride, the tip of the stalk is briefly localised at a position 32.5 ± 0.75 nm ahead of the post-power stroke dwell position, as if 'leaning forward' along the longitudinal axis of the actin filament, as shown in figure 4.7.

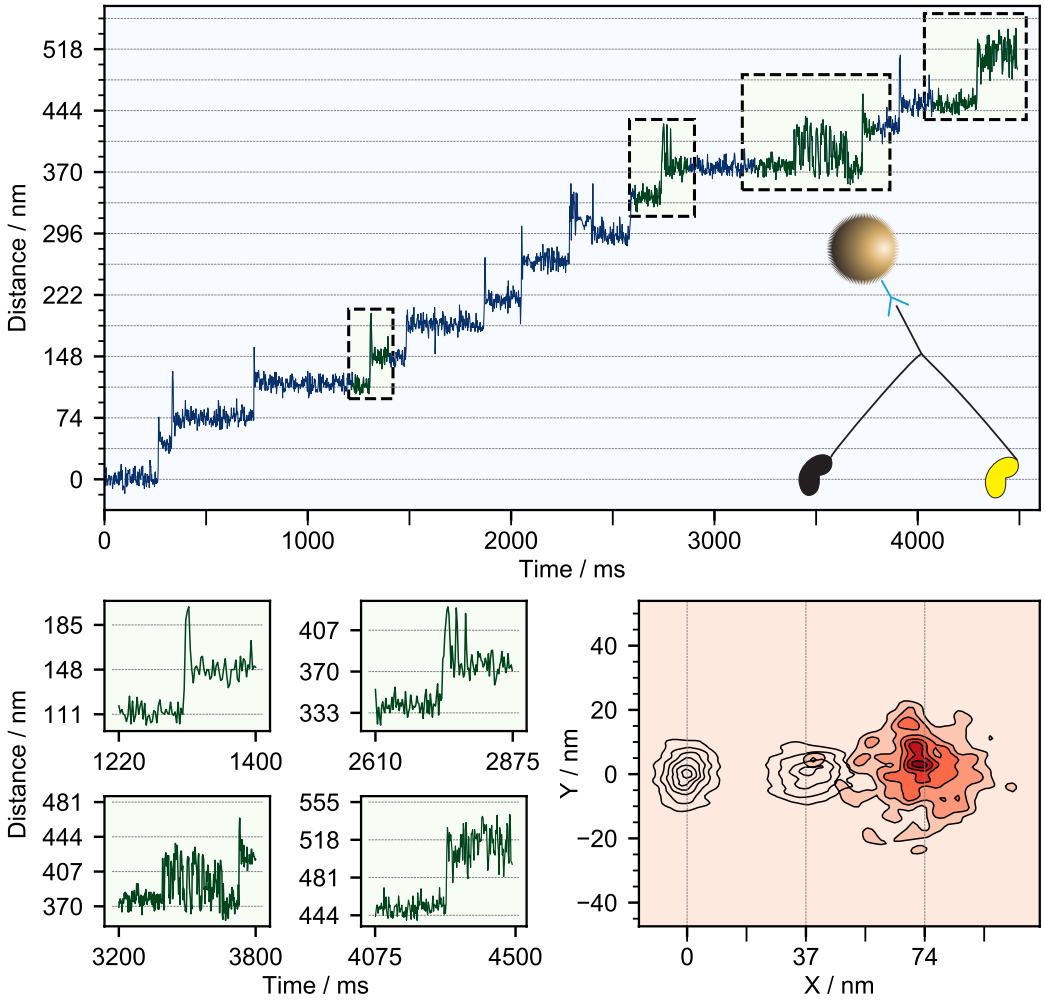


Figure 4.7: A typical trace from a stalk tracking experiment (top). (Bottom-left) Enlarged segments of the the trace highlighting a short-lived transient, a transient which oscillates back and forth, a period of increased movement due to the molecule being bound by only one motor domain and a similar period which then leads to detachment. (Bottom-right) A 2D density estimate of stalk label localisations. The non-shaded densities signifies the localisations before (left) and after (right) the step is taken. The shaded density is the localisations of the label whilst in the transient 'overshoot' state. Sample size: 126 traces giving 317 steps.

During certain strides, the stalk domain can be seen to move back and forth along the longitudinal axis of the actin between the transient position and the final post-power stroke dwell position. Moreover, at the end of a processive run, the stalk is observed to undergo an extended period of this back and forth motion that can easily be attributed to an extended period of the molecule in a one head bound state, prior to detachment from the actin filament.

A 2D kernel density estimate of localisations of the label shows that the stalk transient is constrained along the longitudinal axis of the actin filament with a standard deviation of 18.7 nm. This is comparable to the standard deviation for the MD transient side state 19.5 nm suggesting that the stalk domain may be more rigid than previously thought and tightly coupled through the lever arm to the motor domain.

Correlation of Motor - Stalk Domain Localisation

We next labelled the stalk domain with a Qdot and the motor domain with a 20 nm gold nano particle, in order to track both domains simultaneously with correlative iSCAT and fluorescence (1000 frames/s and 250 frames/s respectively). Our localisation precision of the particles in both iSCAT and TIRF was on the order of ≈ 5 nm at these imaging speeds. Again we observed, with high reproducibility, the forward leaning transient of the stalk domain and this occurred synchronously with the transient detached state observed for the detached labelled motor domain (figure 4.8). The stalk domain transient can be seen even when the unlabelled head is taking a stride. We also observed occasions when the detached motor domain returns to its transient location, instead of binding to the post powerstroke binding location. When this occurs, the stalk domain can be seen to return to its transient location for equal duration, as denoted by the asterisk in the bottom panel of figure 4.8.

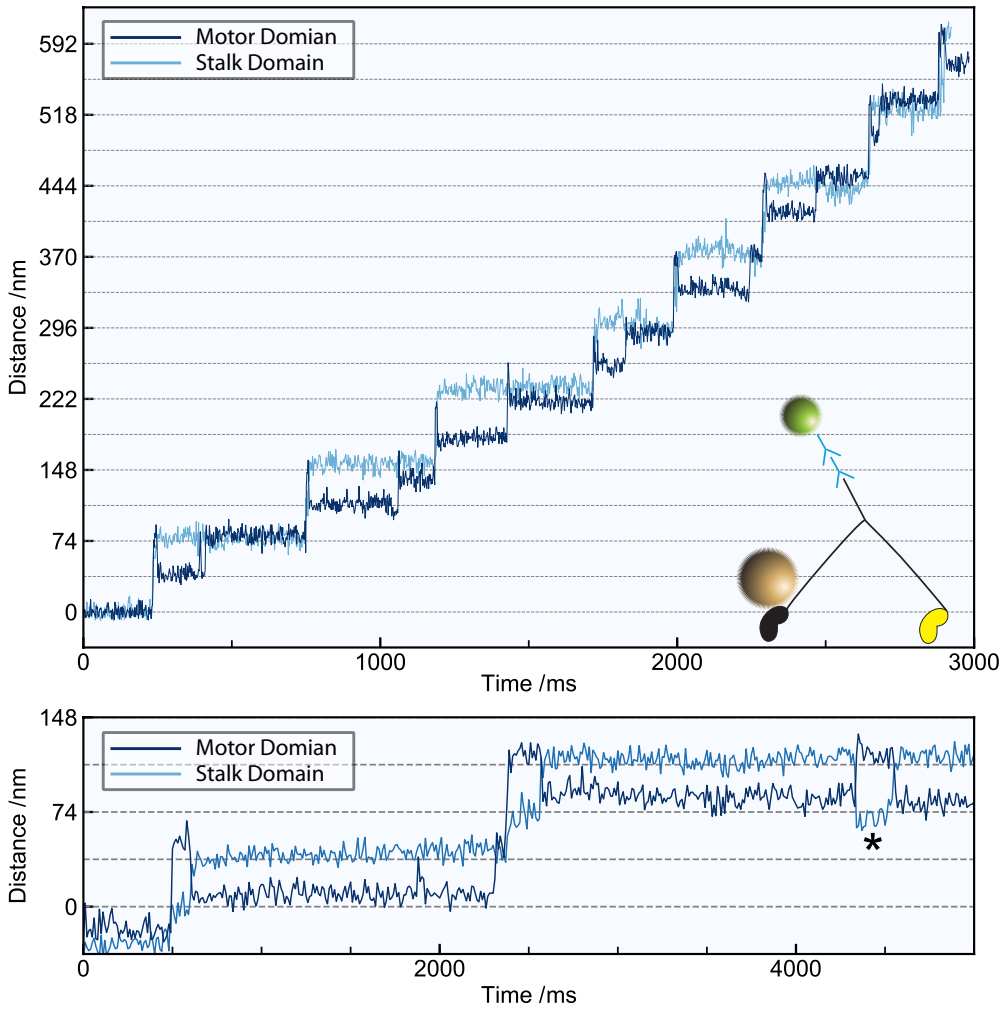


Figure 4.8: Traces from a dual labelled motor - stalk M5a experiment. The stalk transient can be seen reproducibly on nearly every step. The asterisk in the bottom panel highlights an instance when the stalk and motor domain simultaneously return to their transient states.

Dwell Time Analysis

Dwell time analysis of the transient state of the stalk yields a lifetime (τ) of 8.96 $\pm$ 0.41 ms, whilst that for the transient state of the motor domain was 16.57 $\pm$ 0.33 ms. This suggests that the tail relaxes prior to the motor domain binding back to the actin filament.

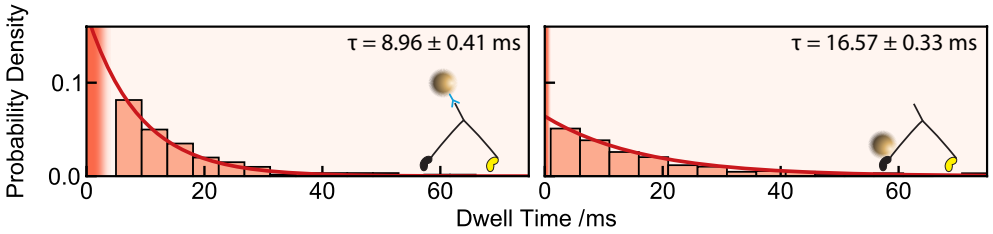


Figure 4.9: Dwell time analysis of the stalk (left) and the motor (right) domains' transient states. The lifetime (τ) of the stalk is shorter than that for the motor, suggesting the stalk relaxes prior to the the motor domain re-binding to the actin filament. The shaded dark red regions are the length of instrument dead time accounted for in the fit to reduce the effects of under-sampling of short dwell times. Stalk domain: N = 138, motor domain: N = 256.

4.4 Conclusions and Outlook

The work in this chapter has demonstrated iSCAT's ability to probe structural and geometric questions regarding the motion of a motor protein such as myosin 5a.

By tracking the lever arm we were able to observe the small swing forward, as the leading domain transitions to become the trailing lever arm domain. Using iSCAT's high spatial and temporal precision one could repeat this experiment, in order to build higher numbers of events recorded. This would allow us to identify the probability of each of the six calmodulin units being labelled, which would translate into differing ratios of the two step sizes observed. This information would not only help us understand the calmodulin exchange process but also, by identifying similarities or differences in the label's lateral motion

to the actin during the smaller step, let us probe the rotation of the lever arm at varying points along the distance between the motor and the stalk domains. This further provides use of the combination of iSCAT and fluorescence imaging as a technique to provide structural dynamic transitions at different domains of a protein.

We also showed the stalk region occupies a transient state constrained to a region along the line of travel and ahead of the post-powerstroke dwell position. The synchronicity and similarities between standard deviation of the two domains' transient states suggests that the stalk domain may be more rigid than previously thought and tightly coupled through the lever arm to the motor domain. The stalk's transient state has not been observed before, probably due to either low temporal resolution in the case of fluorescence or high load at the the stalk as in the case of trapping experiments. The fact that M5a is a cargo transporter suggests that this 'overshoot' we observe is a product of force generation in the molecule. Furthermore, this transient motion of the stalk may be relevant for the efficient motion of the cargoes attached to M5a. This data also provides evidence that the conformational change at the motor domain is coupled to the motion of the M5a at the C-terminal end, ≈35 nm away, indicating the possibility that the M5a is 'rigid' during translocation on the actin filament. The results presented here therefore allow us to correlate the force generation of the stalk domain with the motion of the motor domains. The next step to understanding these results is to discern how the conformational changes observed at each domain aids the force generation in the molecule.

Chapter 5

Type IV Pili Movements of *Pseudomonas aeruginosa*

The following chapter is adapted with permission from:

> L. Talà, A. Fineberg, P. Kukura and A. Persat, Pseudomonas aeruginosa orchestrates twitching motility by sequential control of type IV pili movements, *Nature Microbiology*, 2019, **4**, 774-780.[103]

The experimental setup used to acquire the data in this chapter was built by myself in the Persat Lab, EPFL, as was the LabView software used to acquire the data. Small changes to both the microscope and software were carried out by Lorenzo Talà in remote consultation with myself. Sample preparation and data acquisition was carried out by Lorenzo Talà and Alex Persat. Image processing and data analysis was performed by Lorenzo Talà in consultation with myself and the manuscript above, which this chapter is adapted from, was compiled and edited by all four authors, including myself.

5.1 Introduction

A major challenge that pathogenic bacteria face when establishing an infection is attachment to the target host cell. The net negative charge at the bacterial surface and target host cell's surface results in repulsion and prevents adhesion and infection. This is overcome by localisation of the adhesion site at the tip of long hair-like appendages known as pili or fimbriae. Pili have been discovered to play a role in a number of bacterial mechanisms including phage binding, DNA transfer, biofilm formation, cell aggregation, host cell invasion and motility.

In Gram-negative bacteria there are five known classes of pili: chaperone-usher pili, facilitating host-pathogen interactions; type IV pili, enabling cell adhesion and biofilm formation; conjugative type IV secretion pili, enabling exchange of genetic material between bacteria; type V pili, enabling cell adhesion and biofilm formation in oral bacteria; and curli fibres, enabling biofilm formation in enteric bacteria.

Type IV pili (TFP) in *Pseudomonas aeruginosa*, the focus of this chapter, are oligomeric structures, ranging between 6 to 9 nm in diameter, that span both the inner and outer membrane of the bacterial cell, reaching several micrometres in length. In *P. aeruginosa*, the type IV pili generate motile forces, allowing the cell to adhere to and move along surfaces.[104,105] The term to describe this motion, twitching, was derived from the observation that cells move in a jerky fashion. Twitching motility is the means employed by certain species of bacteria to rapidly colonise a surface and is independent from flagella movement, which is employed more during swimming motility. *P. aeruginosa* performs successive rounds of motor-driven TFP extension and retraction in order to power twitching motility and regulate virulence through mechano-sensing.[106–108]

Pseudomonas aeruginosa is an opportunistic pathogen that causes lung damage in immuno-compromised and cystic fibrosis patients. *P. aeruginosa* is the most commonly studied bacteria for twitching motility due to ease of use in the laboratory, having a strong history of genetic analysis and an easily scored macroscopic phenotype for identifying twitching-impaired mutants.[109–111]

The TFP assembly complexes in *P. aeruginosa* can be thought of as consisting of four subcomplexes, functioning independently, as shown in figure 5.1. First is the outer membrane subcomplex consisting of a dodecamer of PilQ subunits and its lipoprotein pilotin, PilF, together forming the secretin.

PilF ensures the correct localisation and oligomerisation of PilQ in the outer membrane.[112] The secretin provides an outer membrane channel for the pilus fibre to exit the cell.[113]

Second, the motor subcomplex is situated in the inner membrane. The exact composition of the motor subcomplex in *P. aeruginosa* has not been defined but it is thought to comprise of PilB, PilC, PilT, and PilU[114–116] as well as regulatory proteins. PilB, PilT and PilU are ATPases with PilB predicted to provide energy for pilus assembly[117] and PilT and PilU aiding depolymerisation of the TFP. PilD processes prepilins into mature pilins by cleaving a short sequence from their N termini and N-methylating their new termini.[118]

Third, the alignment subcomplex, also situated in the inner membrane, is thought to connect the inner membrane motor and outer membrane secretin subcomplexes to ensure that the highly flexible growing pilus filament is positioned correctly as it extends through the periplasm. In *P. aeruginosa* the alignment subcomplex is thought to consist of the PilMNOP proteins[119] and FimV.[120] PilM is an actin-like protein bound to the N-terminus of PilN.[121] Recent studies have shown PilP, PilN and PilO to form stable heterotrimers, protecting the three individual proteins from degradation by shielding their reactive sites.[122] FimV is required for correct formation of the PilQ secretin complex.[120] It is thought to enable the secretin to pass through the peptidoglycan layer and anchor the assembly to the cell wall.[123] It is not known what the function of the cytoplasmic domain of FimV is, but it may be involved in pilus biogenesis.[124]

The fourth subcomplex is the pilus itself, which extends away from the outer membrane. Composed predominantly of PilA,[125] together with the minor pilins FimU, PilVWX, and PilE,[126,127] it is the most dynamic of the subcomplexes, as it is repeatedly assembled and disassembled. Like PilA, the minor pilins are

processed by PilD. The majority of a pilus fibre consists of PilA, however the minor components are also present at surface exposed pili.[128,129] The question of whether the tip of a pilus complex in *P. aeruginosa* has PilA or a minor pilin is still an open and important question in the field, as understanding this can help better understand the pilus' interaction with surfaces like the membrane of a host cell.[106,130]

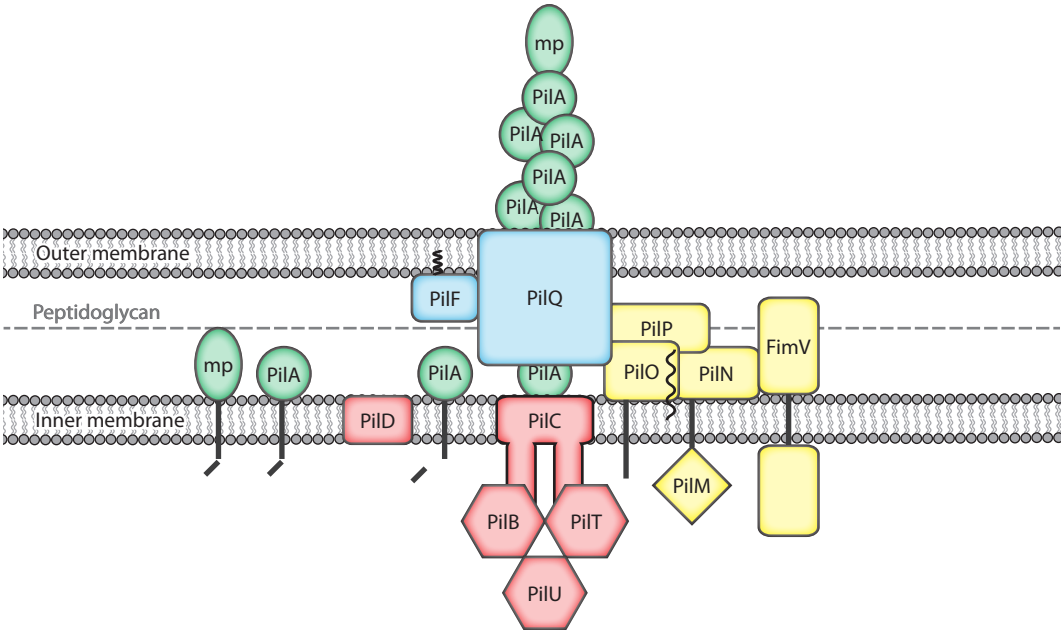


Figure 5.1: Type IVa pili assembly and subcomplex components. The TFP assembly system consists of four interacting subcomplexes. The outer membrane subcomplex (blue - PilF, PilQ), the inner membrane motor subcomplex (red - PilC, PilD, PilT, PilU), the alignment subcomplex (yellow - PilM, PilN, PilO, PilP, FimV), and the pilus subcomplex (green - the minor pilins (mp) [FimU, PilV, PilW, PilX, PilE], and the major pilin (PilA)). This figure is reproduced with permission from L. L. Burrows, Pseudomonas aeruginosa Twitching Motility: Type IV Pili in Action, *Annual Review of Microbiology*, 2012, **66**, 493-520. ©Annual Reviews 2012[106]

Pili retraction motors can generate forces up to 100 pN but how this mechanism works is still largely unknown.[131,132] To answer this question, the distribution of individual pili around single cells has been indirectly inferred from tracking of cell body displacements.[133] Also, labelling strategies have largely helped not only in the visualisation of extension and retraction events, but also

in deciphering the function of TFP in horizontal gene transfer and mechanosensing.[134,135] These methods are powerful but remain invasive, and are limited by labelling robustness during high-speed or long-term imaging of TFP. As a result, changes in TFP length, number, and extension-retraction frequencies, which ultimately regulate bacterial interaction with the environment, are difficult to measure during the course of motility. Understanding this connection therefore rests on our ability to visualise and monitor the dynamics of individual TFP on short timescales of extension-retraction (subseconds) and on longer timescales of surface colonisation (minutes to hours).

This chapter discusses the work done in collaboration with the Persat group in EPFL to adapt the iSCAT microscope in order to visualise TFP without fluorescent labelling and with low phototoxicity to the cells. This, therefore, allows us to better understand the functions of PilT and PilU and thereby suggest a model for understanding how *P. aeruginosa* effectively uses TFP to generate forces for cell displacement.

5.2 Methods

Bacterial Strains

Strains and plasmids used in this work were described previously.[136] Double-deletion mutant *pilTU*$^{-}$ *fliC*$^{-}$ was generated by conjugation of *pilTU*$^{-}$ mutants with the plasmid pJB215 using a standard mating protocol[137] by the Persat group.

Glass Coverslip Preparation

Glass coverslips (22 × 40 mm^2 No. 1.5, Marienfeld) were cleaned as described.[8] Briefly, coverslips were washed sequentially with Mili-Q, ethanol, Mili-Q, isopropanol, Mili-Q, ethanol and Mili-Q, with excess water removed by a stream

of nitrogen. For visualisation we used two platforms. In the first, we plasma-bonded polydimethylsiloxane (PDMS) micro-channels (width - 500 µm; depth - 90 µm) fabricated using standard photolithography methods. In the second platform, we deposited PDMS gaskets on clean coverslips. PDMS gaskets were obtained using biopsy punches of diameter 3 or 6 mm.

Sample Preparation

Single colonies of each strain were grown in Luria-Bertani (LB) medium overnight at 37 °C. Cultures were diluted 1:500 and grown to early exponential phase before visualisation. For motility visualisation, cells in early exponential phase were plated on plain LB agar plates for 4 h, harvested by gentle flushing with LB medium followed by dilution to absorbance A600 < 0.05. Cells were loaded into either a microfluidic chip or PDMS gaskets. Microfluidic chips were first loaded with plain LB medium. After attaching tubing to the chips, exhaust tubes were dipped in bacterial culture and cells were loaded by aspiration using a syringe pump (Crpump, No. ZS100). The gaskets were loaded with 20 µl of bacterial culture at A600 < 0.05, then washed twice with fresh LB after 5-10 min incubation at room temperature (if a higher A600 was used). When the loading process was complete, gaskets were sealed with a small coverslip to prevent liquid evaporation that would have generated fluctuations on iSCAT images.

Experimental Setup Details

The correlative iSCAT and brightfield setup is adapted from that described previously.[53] The details of the experimental setup with modifications to reduce phototoxicity to allow live-cell visualisation during long acquisition times are discussed in section 3.2.

For iSCAT, a 635 nm diode laser (Coherent Obis) is spatially filtered through a 50 µm pinhole and recollimated. A Photonfocus (MV-D1024-160-CL-8) (CMOS) camera was used with a pixel size of 10.6 µm with an imaging lens of 1000 mm . The effective magnification was 333× and pixel size was 31.8 nm px^{-1}.

For the brightfield channel, a white LED (Thorlabs, No. WFA1010) is positioned above the sample and imaged onto a CMOS camera (PointGrey, CM3-U3-31S4M) with a pixel size of 3.45 µm using a 400 mm lens. The effective magnification was 133× and pixel size was 25.9 nm px^{-1}.

As detailed in 3.2, the focus stabilisation used a cyto-compatible system with a weak infrared laser (850 nm, 3.5 mW; Thorlabs, No. CPS850). A CMOS camera (Thorlabs, No. DCC1545M) was used to detect total infrared light reflected by the glass-water interface.

Twitching Motility Assays

Motility assays were performed by stabbing and pipetting a 0.5% agarose LB plate with 2 µl of stationary-phase *P. aeruginosa* culture at the gel-plastic interface of the plate. The plates were incubated for 24 h at 30 °C before removal of agarose and staining of the plastic dish with a 0.1% solution of crystal violet in water. We performed microscopic twitching visualisations by pipetting 0.5 µl of exponentially growing cells (A = 0.1 at 600 nm) on a 0.5% agarose LB pad. These were then flipped onto a glass-bottomed dish (Mattek, No. 1.5 coverslip) and incubated at 30 °C for 5 h. The leading edges of the expanding colonies were then visualised for 2 min at 1 frames/ s by phase contrast microscopy on a Nikon TiE equipped with a 100×, numerical aperture 1.45 objective and a Hamamatsu Orca R2 camera.

Image Processing

To reveal the interferometric component of the signal, each frame of a given sequence was divided by a reference. This reference image was generated by computing the median of each pixel value throughout the entire stack of images. To improve visualisation, we applied a band pass filter to dampen the contributions of small and large structures (smaller than 1 pixel and larger than 13 pixels) with the FFT plugin of ImageJ.[138] To reduce slight temporal variation in illumination, each frame was divided by its mean pixel grey value.

Image Analysis of Pili Dynamics Quantification

To extract time delays between attachment and retraction of the TFP to a state where they are rigid and tensed, we manually recorded the frame-number of pili tip attachment (appearance of a stationary dark spot at the tip) and that of pili under tension (without pili fluctuations), where these events were clearly visible and could be measured with accuracy. Time delays were obtained by multiplying the frame difference by the acquisition frame time (frame rate, 200 frames/ s). We measured tension times with 20 wild-type (WT) cells (27 retractions), 23 *fliC*$^{-}$ cells (54 events), and 30 *pilU*$^{-}$ *fliC*$^{-}$ cells (47 events) from data acquired on a minimum of three separate days. Similarly, dwell times were obtained by manually measuring the time difference between attachment and detachment of each pilus from the same cells with the addition of 14 *pilT*$^{-}$ *fliC*$^{-}$ cells (45 events). Intensity measurement of attachment, tension and detachment was manually extracted by plotting the intensity profile along pili using plot profile, an ImageJ built-in tool. We performed intensity peak detection from the recorded profile for tip attachment, and tension using MatLab. Pili length was measured from the tip attachment point to the middle of the first fringe of the cell body diffraction pattern from the same dataset. Retraction frequency

was computed by counting all obvious retractions within a movie but discarding those pili already tensed in the initial frames. The total number of retractions was then divided by the movie time for 30 *fliC*$^{-}$ and 23 *pilU*$^{-}$ *fliC*- cells from at least three biological replicates. Pili were counted on 20 wild-type, 15 *fliC*$^{-}$, 18 *fliC*$^{-}$ complemented, 19 *pilA*-, 22 *pilA*- complemented, 11 *pilT*$^{-}$ *fliC*$^{-}$, 15 *pilT*$^{-}$ *fliC*$^{-}$ complemented, 18 *pilU*$^{-}$ *fliC*$^{-}$, and 17 *pilU*$^{-}$ *fliC*$^{-}$ complemented cells from the same strain culture. Flagella were counted from 52 wild-type, 51 *fliC*$^{-}$, and 50 *fliC*$^{-}$ complemented cells from at least three biological replicates.

Image Analysis of Cell Motility with iSCAT

Cell motility movies were acquired at 10 frames/ s and binned ten times to obtain a final movie rate of 1 frames/ s. The leading pole of the cell, defined as the centre of the white spot in the middle of the circular fringes of the cell body, was manually tracked during cell displacement. Only those cell displacements where no change in contrast of the leading pole was observed were recorded, to assess the effective influence of pili retraction on displacement and to discard Brownian motion effects when cells were not in contact with the glass surface. We note that some cells appeared to hover on the surface by Brownian motion, using TFP to maintain proximity to the surface. We recorded the number of visible retractions along each track. In total, 14 tracks were recorded for wild-type, 13 for *fliC*$^{-}$ and 15 for *pilU*$^{-}$ *fliC*$^{-}$ from the same strain culture.

Statistical Analysis

As the time delay and tension time data were not normally distributed, we chose median as an indicator of the central tendency of distribution. Statistical analysis was performed using the bootstrap method in MatLab to resample the data of each strain into 300 different groups; and to compute the median of the medians of each bootstrap group, to obtain a more robust estimate of

population behaviour. We computed the 95% confidence interval by taking the highest and lowest values of the bootstrap median dataset after removing the top and bottom 2.5% of the data points. The same approach was used to determine retraction frequency, pili length and displacement per retraction. Pili numbers in complementation analysis were computed by taking the mean of the bootstrap medians and the bootstrap 95% confidence interval as stated previously. A difference between the two groups was defined as statistically significant when their 95% confidence intervals did not overlap.

5.3 Results and Discussion

Phototoxicity

The first consideration when imaging bacterial cells with iSCAT is the trade-off between high illumination intensity to increase scattering contrast and photo-damage to the cells, impeding their function. In the extreme, high laser intensity focused onto the sample causes cell lysis through a combination of photothermal and photochemical damage.[139–142] However, even at illumination intensities low enough not to cause lysis, cell damage was observed as a complete loss of motility. In order to prevent cell damage the experimental setup was modified as discussed in section 3.2. Specifically, these were: the use of a red wavelength for imaging, the use of an infrared wavelength for focus stabilisation rather than ultra-violet as previously used, the installation of a shutter to minimise the duration of sample illumination, and the implementation of a brightfield channel to locate cells before the iSCAT illumination was used.

Visualising Bacterial Filaments

Under brightfield illumination, wild-type *P. aeruginosa* appeared to be rod-shaped with no visible surface structures (figure 5.2a). Simultaneous iSCAT

images of the same cell revealed micrometre-long extracellular filaments and shorter structures with alternating intensity extending from the cell body (figure 5.2b). Cells of in-frame deletion mutants in the pilin subunit gene pilA displayed no such slender structures, suggesting that these were TFP (figure 5.2c). A deletion of the flagellin gene *fliC* removed structures with periodic pattern, suggesting that this signal was generated by a single helical flagellum with a periodicity of $1.4 \pm 0.1\,\mu m$ (standard error, n = 10), consistent with previous measurements for helical pitch[143] (figure 5.2d). Quantification of filaments showed that the wild-type cells had approximately one pilus per cell (cells from the same culture n=20) and $pilA^-$ had no TFP (n=19) but WT levels are restored in the complemented strain (n=22). $fliC^-$ mutant cells had about five (n=15), which decreases to WT level in the complemented strain (n=18) (figure 5.2e). As expected, most wild-type cells had one flagellum and $fliC^-$ had zero. We attribute the hyperpiliation of $fliC^-$ to our sample preparation process, which first selects for cells that reach and remain on the surface. This loading process induces positive selection for more piliated cells that attach more strongly to the coverslip.

Measurements of attached TFP length distributions in WT (combined number of pili from cells imaged in at least three biological replicates n=27) and $fliC^-$ (n=54) shows that the flagellum-less mutant has no defect in TFP length (figure 5.2f).

Live-cell iSCAT can capture multiple successive extension-retraction events while monitoring cell body displacements. This allows for the quantification of attachment-retraction frequencies whilst monitoring cell body displacement. Since the signal generated from the flagellum was stronger than that from TFP, and because swimming may interfere with twitching motility, we sought to perform most dynamic visualisations on a $fliC^-$ background. We tested whether

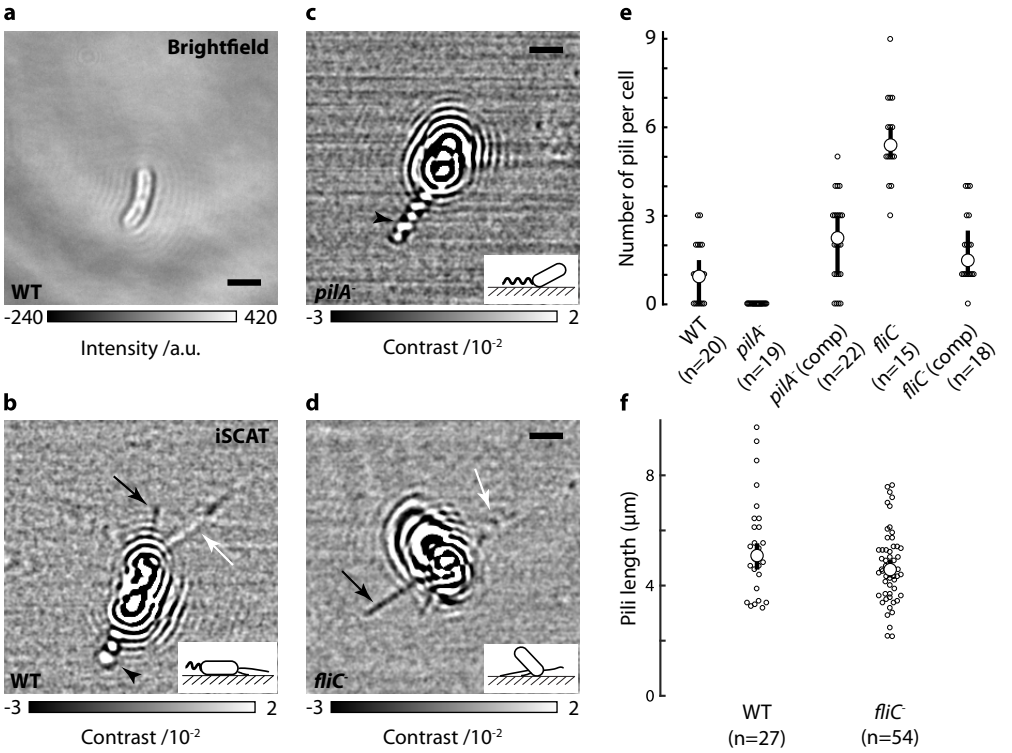


Figure 5.2: **a**, Brightfield and **b**, iSCAT images of a single wild-type (WT) *P. aeruginosa* cell. The brightfield image shows only the rod-shaped body of the bacterium, while multiple extracellular structures are visible in iSCAT. Flagellum (black arrowhead) and type IV pili with constant (black arrow) or spatially varying contrast (white arrow). **c**, A deletion mutant of the pilin gene *pilA* displayed no extracellular slender structures. **d**, A mutant in the flagellin subunit gene *fliC* had no polar filaments with alternating contrast. Inserted illustrations in iSCAT images show the position of cell and filaments relative to the coverslip surface. Scale bars: 2 µm. **e**, Quantification of mean TFP per cell with iSCAT. **f**, Attached TFP length distribution in WT and *fliC*$^{-}$. **e-f**, Small circles represent individual measurements, large circles are bootstrap medians and error bars bootstrap 95% confidence interval.

this would affect TFP dynamics, and found that there were no distinguishable differences in either cell displacement per retraction or retraction frequencies between wild-type cells and the flagellum-less mutant (figure 5.3).

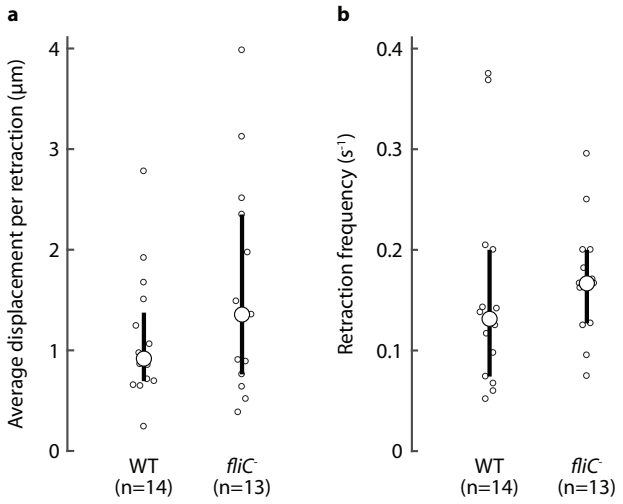


Figure 5.3: **a** Average displacement per retraction measured at 1 fps in WT (number of tracks n = 14) and fliC^{-} (n = 13) mutant cells. **b** Retraction frequencies measured from the same movies as in **a**. Small circles correspond to individual measurements, large circles to medians of bootstrap medians and error bars to bootstrap 95% confidence interval.

Filament Morphology

We observed three distinct patterns generated by TFP on iSCAT images: straight dark filaments, straight filaments with alternating black and white contrast, and curved filaments with fainter contrast (figure 5.4). Changes in the contrast of a fibre are a manifestation of the shift from constructive to destructive interference, with a full phase change corresponding to a spatial shift of $\lambda/2n$, where λ is the illumination wavelength and n the index of refraction of the medium.[23] Intensity values can thus be used as a proxy for in-depth position of TFP.[144] For example, TFP of uniform intensity lay flat against the surface. Those exhibiting successive positive and negative intensity values along their length are at an angle. As a result, single iSCAT images

provide us with the position and orientation of single TFP in three dimensions, thereby allowing quantitative inference of spatial position on and away from the attachment surface. We could, for example, observe differences in TFP positioning of standing versus horizontal cells.[145] TFP of standing cells, which orient vertically on the surface attached by one pole, were mostly (79%) flat against the surface. In contrast, in crawling horizontal cells, TFP were in most cases (81%) oriented at an angle between the glass surface and the cell pole. In summary, iSCAT provides the ability to probe TFP dynamics at high spatial and temporal resolution in three dimensions, without obstructing native biological functions.

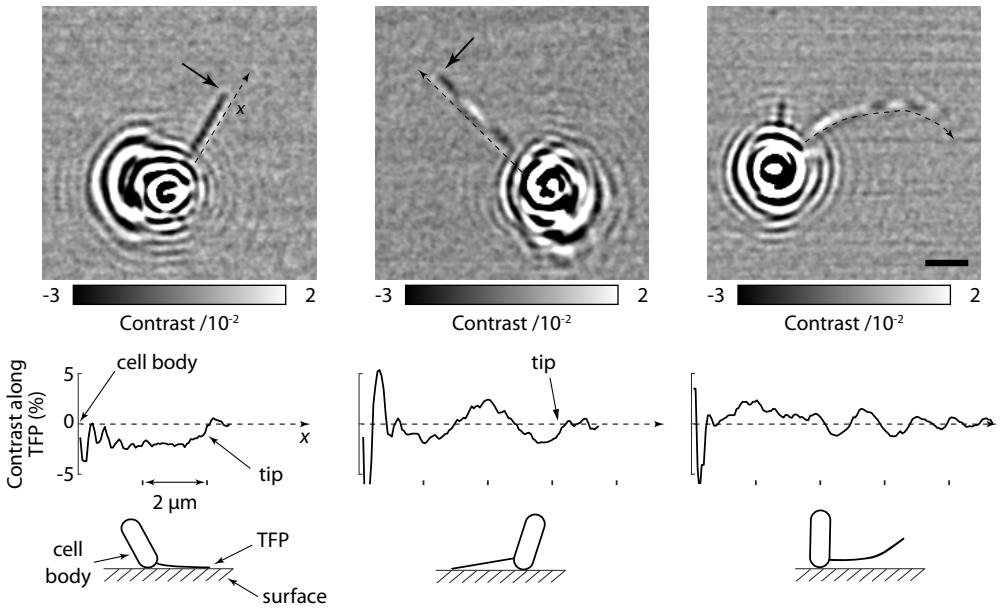


Figure 5.4: **a** Images of three representative TFP positions and orientations visualised by iSCAT. TFP that have constant contrast lie flat on the surface (left panel), those with alternating contrast form a finite angle with the coverslip (middle panel), while curved fibres with oscillating and irregular contrast are defined as floppy (right panel). Below each image, a plot of the pixel contrast value along the pilus allows determination of whether the pili lie flat, at an angle, or are fluctuating. The illustration represents the putative three-dimensional orientation of the pilus and cell body. Scale bar: 2 µm.

The images in figure 5.5 highlight two distinct TFP morphologies and dynamics: straight-stationary and curved-fluctuating filaments. We verified that

the straight conformation was a result of tension generated during retraction. At the molecular level, the extension motor PilB polymerises PilA subunits to drive TFP growth. The two retraction motors, PilT and PilU, drive retraction by depolymerising PilA back into the periplasm, but whether their functions are redundant remains unclear.[106,136] *fliC*⁻ cells displayed both fluctuating curved and straight-stationary TFP. In contrast, a *pilTU*⁻ *fliC*⁻ mutant had only curved TFP that were fluctuating. Tensed, floppy, flat, and angled pili were observed with similar results in all our retractile strains (WT, *fliC*⁻ and *pilU*⁻ *fliC*⁻), whereas only floppy pili were observed in our *pilT*⁻ *fliC*⁻. This demonstrates that straight TFP are under tension during retraction.

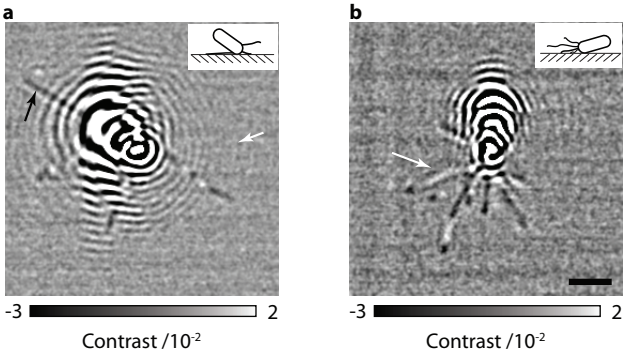


Figure 5.5: **a** TFP of *fliC* deletion mutant cells exhibit all three morphologies. **b** Cells lacking retraction motor genes *pilT* and *pilU* show only floppy TFP. We encountered these features throughout all our visualisations. Tensed (black arrows), floppy (white arrows). Scale bar: 2 µm.

TFP Dynamic Activity

Given the lack of a clear function for the two retraction motors in *P. aeruginosa*, we sought to identify functional differences between PilT and PilU by visualising TFP dynamics in respective mutants. Both *pilT*⁻ and *pilU*⁻ mutants lost their ability to twitch in a typical agar stab assay, and have been reported as being hyperpiliated.[116] In *Neisseria gonorrhoeae*, PilU has no apparent role in twitching motility.[146] In our visualisations (figure 5.6a), whilst *pilT*⁻ *fliC*⁻

could not trigger retraction in the timescales of our visualisations, a *pilU*⁻ *fliC*⁻ deletion mutant could still transition to a tensed state, demonstrating its ability to retract TFP. In addition, *pilU*⁻ *fliC*⁻ tends to have fewer, not more, TFP compared to *fliC*⁻, in contrast to *pilT*⁻ *fliC*⁻ (figure 5.6b). Thus, although cells lacking pilU can retract TFP, they do not migrate in typical twitching assays where colonies spread at the interface between a plastic dish and agar.[136]

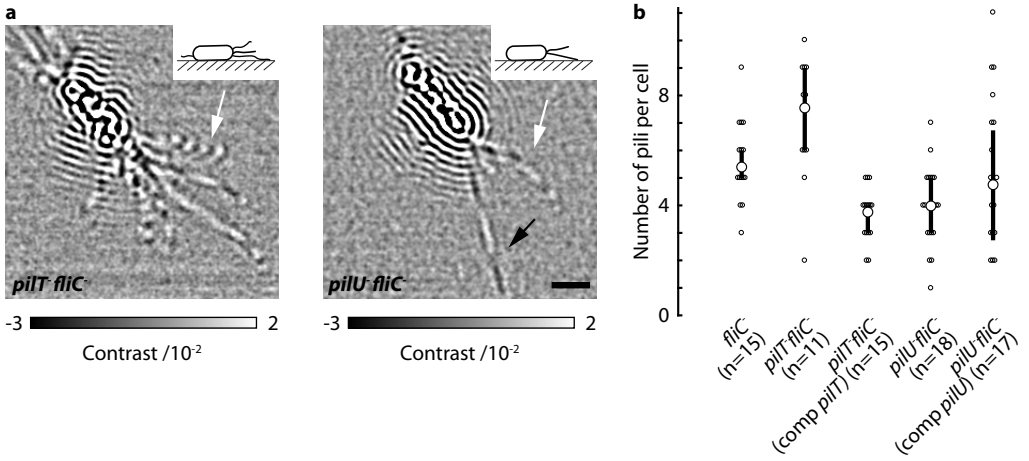


Figure 5.6: a, iSCAT images of mutants *pilT*⁻ *fliC*⁻ and *pilU*⁻ *fliC*⁻. The black arrow indicates a tensed pilus; the white arrows indicate floppy pili. Scale bar: 2 µm. **b**, Number of TFP in motor mutants and their corresponding complementation strains. Large circles are means of bootstrap medians and error bars are bootstrap 95% confidence intervals. Small circles are individual measurements.

We sought to elucidate this paradox by examining TFP dynamic activity (figure 5.7). We first found that TFP length was identical between *fliC*⁻, *pilU*⁻ *fliC*⁻, and *pilT*⁻ *fliC*⁻, demonstrating that extension is not affected. Although retraction frequency was slightly decreased in *pilU*⁻ *fliC*⁻ compared to *fliC*⁻, this could not explain the total loss of motility observed in twitching assays. Finally, measurement of displacements in free solution on glass showed that each retraction generates an approximately similar displacement in *fliC*⁻ and *pilU*⁻ *fliC*⁻. This demonstrated that TFP in cells lacking pilU do not lose their ability to generate displacements.

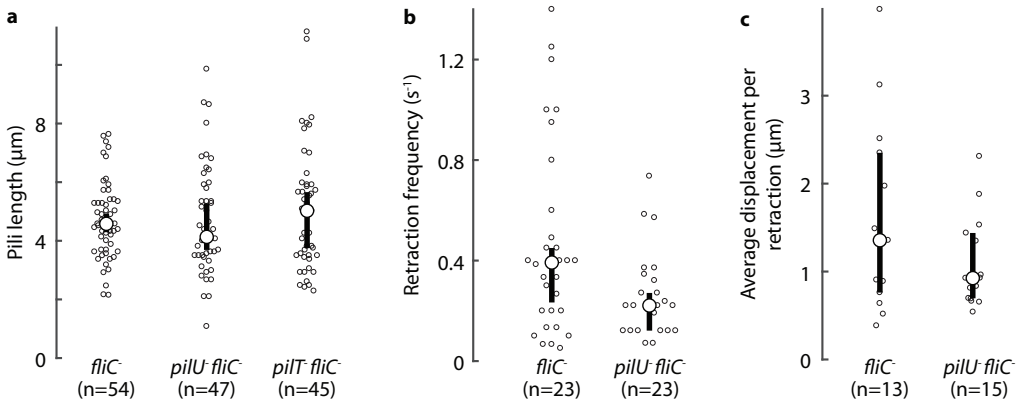


Figure 5.7: **a**, Average lengths of TFP that attached to the glass surface in *fliC*⁻, *pilU*⁻ *fliC*⁻ and *pilT*⁻ *fliC*⁻. **b**, Retraction frequencies for *pilU*⁻ mutant compared to *fliC*⁻. **c**, Average displacement per retraction for *fliC*⁻ and *pilU*⁻ *fliC*⁻. Small circles correspond to individual measurements, large circles are medians of bootstrap medians and error bars are bootstrap 95% confidence interval.

Since dynamics were not grossly affected by the absence of PilU in free solution we sought to highlight a potential role of PilU in generating retraction force. We visualised twitching motility at the leading edge of colonies sandwiched between glass and agarose surfaces by phase contrast microscopy (we could not implement iSCAT because the gel provides too large a scattering background). We reasoned that friction between the cell body and substrate during locomotion in this configuration is higher than in free solution, thus requiring greater forces to generate displacements during retraction. *fliC*⁻ cells at the leading edge of expanding twitching colonies were highly motile between glass and 0.5% agarose gel. In this same configuration, *pilU*⁻ and *pilU*⁻ *fliC*⁻ were barely motile, consistent with twitching assays. We could repeat this defect in *fliC*⁻ by increasing the friction of the cell body with the surface using a higher agarose concentration, which requires a higher retraction force to generate similar displacement. Taken together, this suggests that PilU contributes to increasing TFP retraction force in conjunction with PilT, rather than acting as an independent retraction motor. By analogy with the torque-dependent recruitment of flagellar motors, PilU could be activated when

PilT reaches a threshold force,[147] consistent with the fact that PilU localises at the leading poles of twitching cells.[114] Alternatively, PilU could regulate PilT activity for example, either through direct interaction or by mediating the function of minor pilins inserted in TFP.[148] In summary, *P. aeruginosa* uses one motor, PilT, to twitch in a low-friction environment, but leverages the companion ATPase PilU to power displacements when friction increases.

TFP Dwell Time Analysis

A key question arising from these movies of random attachment and detachment events is how *P. aeruginosa* orchestrates force generation to drive motility. To optimally generate displacements, cells must coordinate TFP retraction with attachment and detachment.[149] To answer whether cells coordinate this or whether extension and retraction is random, we performed visualisations of each step involved in individual TFP cycles (figure 5.8b). We found that the tip of extended TFP occasionally appeared as a stationary dark spot while the remainder of the fibre fluctuated, indicating initial attachment. The same

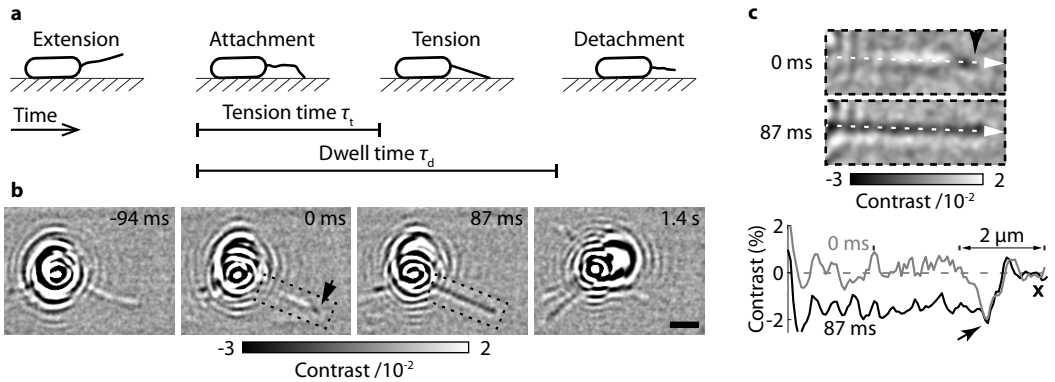


Figure 5.8: **a**, An illustration of the optimal sequence of events for TFP function. **b**, Successive events from **a**, visualised with iSCAT. The attached pilus tip appears as a stationary dark signal at 0 ms (black arrow). The entire fibre transitions into lower-intensity values at $\tau_t = 87$ ms, before detaching at $\tau_d = 1.4$ s. Scale bar: 2 µm. **c**, Close-up view of attachment and tension from **b** with corresponding intensity profile along the pilus. A dip in intensity is observed at the tip at 0 ms (black arrow on image and graph), transitioning to a uniform low value at τ_t.

fibre then transitioned to a straight stationary line, indicating retraction and tension, before eventually detaching (figure 5.8c). We could thus time the transitions between attachment, retraction, and detachment of single fibres.

We first measured the dwell time, τ_d, defined as the residence time of the pilus on the glass surface from tip attachment to detachment. The TFP of the retraction-less mutant *pilT*$^-$ *fliC*$^-$ could still attach, with a median dwell time of 75 ms (65-90 ms; median and 95% bootstrap confidence interval), which is a measurement of the intrinsic residence time of passive fibres on the surface (figure 5.9).

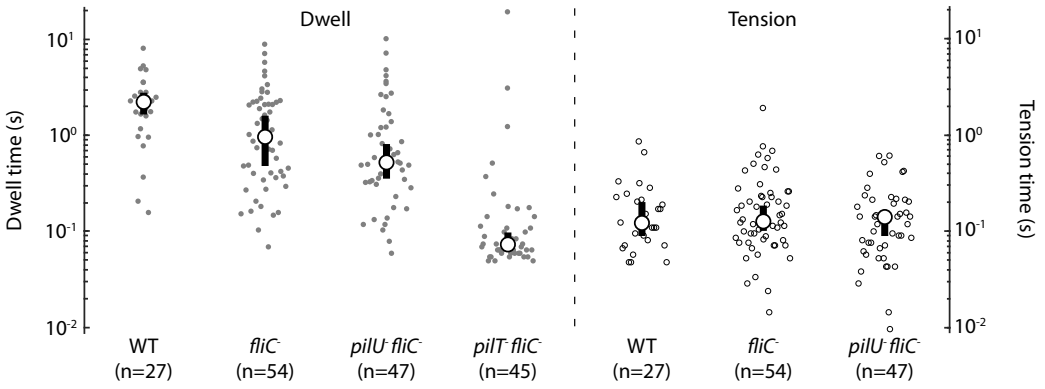


Figure 5.9: Measurement of dwell and tension times in wild-type (WT), *fliC*$^-$, *pilU*$^-$ *fliC*$^-$, and *pilT*$^-$ *fliC*$^-$ cells. Small circles correspond to individual measurements, large circles to median and error bars to bootstrap 95% confidence intervals.

Given that the retraction speed of TFP is about $1\,\mu\mathrm{m\,s^{-1}}$, this would enable only a short 70 nm displacement per retraction.[134] Surprisingly, the dwell time in cells capable of retraction was, however, much longer: 2,315 ms (1,710-2,635 ms) in wild-type, 997 ms (590-1,795 ms) in *fliC*$^-$ and 540 ms (405-840 ms) in *pilU*$^-$ *fliC*$^-$. This indicates that tension force during retraction enhances TFP adhesion, increasing surface attachment time and thereby improving effective displacements of the cell body. In analogy with the formation of catch-bonds by the adhesin FimH in *Escherichia coli*, tension

force may induce a conformational change in the structure of TFP, thereby increasing the strength of its attachment to the surface.[150,151] We also note that dwell times are typically less than 3 s, thereby facilitating TFP release for subsequent extension-retraction cycles, and that *pilU*$^{-}$ *fliC*$^{-}$ had slightly decreased dwell time, possibly as a consequence of lower retraction strength.

The short dwell time of relaxed TFP on the surface suggests that retraction must take place rapidly after attachment. To achieve this, retraction must occur at high frequency or systematically after initial pilus contact with the surface. The first scenario would lead to inefficient conversion of force to displacement, while the second suggests that cells sense contact with their TFP. To identify the strategy used by *P. aeruginosa* to coordinate TFP retraction with attachment, we directly measured tension time, τ_t, defined as the delay between tip attachment and pilus tension. We found that TFP became tensed 130 ms (95-215 ms) after tip attachment in wild-type and 135 ms (105-198 ms) in *fliC*$^{-}$, which is close to the dwell time of relaxed TFP on the surface of *pilT*$^{-}$ *fliC*$^{-}$. Also, *pilU*$^{-}$ *fliC*$^{-}$ had a similar reactivity (τ_t = 150 ms (90-155 ms)) (figure 5.9), showing that PilT motors engage rapidly, optimising retraction efficiency and subsequently increasing the dwell time of TFP on surfaces. This finding also hints at the possibility that cells sense tip attachment, which rapidly initiates retraction. Measuring the proportion of TFP retraction without attachment further supports this hypothesis: most extended TFP did not retract during the course of visualisation unless their tip attached to the surface (figure 5.10a). This demonstrates that TFP attachment stimulates retraction, and that motors respond to a signal generated by contact of the tip with the surface. Thus, *P. aeruginosa* uses a high-efficiency sensing strategy to deploy and coordinate TFP, rather than being reliant on random motor activation.

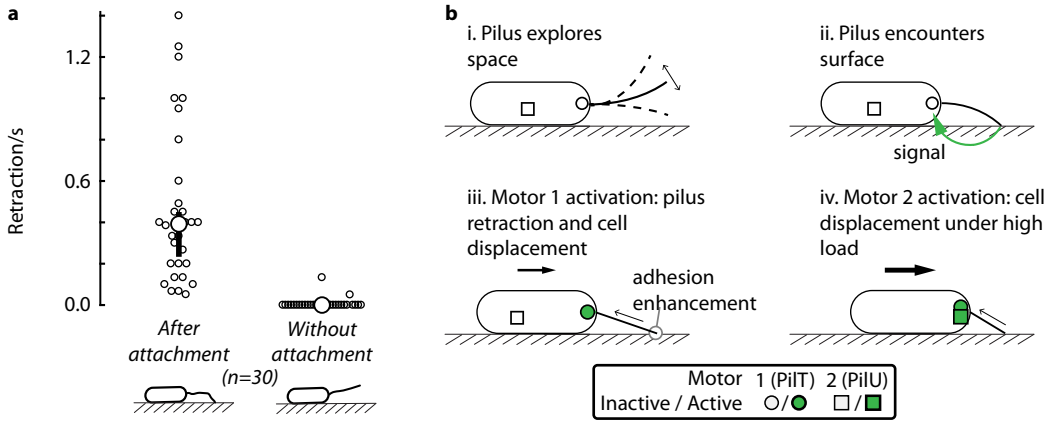


Figure 5.10: a, TFP retraction frequencies for attached and unattached TFP in *fliC*$^{-}$. TFP retract mostly only after their tips touch the surface, indicating that attachment stimulates retraction. Small circles correspond to individual measurements, large circles to median and error bars to bootstrap 95% confidence intervals. **b**, Proposed model for sequential control of TFP motion. During spatial fluctuations **(i)**, attachment of TFP tip to the surface generates a signal activating PilT **(ii)**. This causes pilus retraction and tension, reinforcing attachment and resulting in longer dwell times and cell displacement **(iii)**. PilU engages with power cell displacement under strong loads, for example, in environments with increased friction on the cell body **(iv)**.

5.4 Conclusion and Outlook

The work in this chapter is the first to be able to visualise TFP dynamics label-free with such a high frame rate so as to be able to achieve a high temporal resolution. This has allowed us to quantify dwell time statistics for TFP and further our understanding of the role PilT and PilU play in retraction.

Our measurements indicate that *P. aeruginosa* precisely coordinates TFP motorised activity with attachment, by successively sensing surface contact, initiating retraction by a first motor, improving surface attachment during retraction through a catch-bond, and triggering a second motor to generate displacement under high load (figure 5.10b). In the same manner as animal locomotion, the sequential control of pili movements could be coupled to sensory feedback enabling transformation into cell displacements, thereby increasing the efficiency of conversion of chemical energy into mechanical work. For

example, animals use multiple sensory inputs such as mechano-sensation and proprioception to control and synchronise limb motion during locomotion.[152,153] Here, we suspect that tip contact generates a mechanical signal read by sensory components that triggers TFP retraction by PilT, and subsequent activation of PilU during twitching under high load. Combining visualisations of bacterial surface structure dynamics with molecular characterisations will eventually generate a holistic understanding of their functions, ultimately helping us to understand how microbes physically interact with their environment and highlighting shared strategies among seemingly distant living organisms.[107]

Since the publication of this work,[103] further works by Adams *et al.*[154] and Chlebek *et al.*[155] have sought to clarify the role of PilU in TFP retraction using, along with other methods, visualisation through epifluorescence microscopy. They found that PilU requires the presence of PilT to facilitate TFP retraction and is necessary for maximal retraction force for the competence pilus in *V. cholerae*.[155] It was also commented that the PilT dependence of PilU is found in several other species of bacteria.[154] This leads to the idea that the PilT dependence is a conserved feature. Adams *et al.*[154] speculates that the coupling between PilU and PilT allows bacteria to function under a wide range of loads without the need for several, separate motors of varying strength. To do this, the two motors must always be coordinated. These publications, together with the results detailed in this chapter, help to explain the purpose of PilU with respect to PilT and highlights iSCAT's ability to measure TFP dynamics to provide mechanistic insight into underlying protein complexes' function.

Improvements to the microscope setup would allow one to further understand how TFP function. The first most obvious hurdle to overcome is to suppress the fringes emanating from the cell body. This could potentially be achieved through further improvements to scanning techniques like rotating coherent

illumination[156] or 'smart scanning'.[157]

Rotating coherent illumination is achieved by coupling the laser into the back focal plane of the objective at a numerical aperture just under the critical angle. This illuminates the sample at a high polar angle exciting spherical wavefronts from two nearby scatterers with a phase difference of $\Delta\varphi = \pi$, thus improving resolution. Coupling this, by scanning the oblique illumination through the full range of azimuthal angles (ϕ), averages the coherent illumination over the scatterer, in theory reducing the diffraction rings produced in the image. The increase in resolution coupled with the reduction in ringing would dramatically improve the image quality and allow for more in depth quantification of the image.

'Smart scanning' relies on the use of a feedback loop within the hardware of the microscope to detect where the cell body is and prevent illumination of that area of the sample. This can be enabled through the use of a well registered brightfield channel and a field-programmable-gate-array (FGPA) card, producing a rapid feedback loop between illumination, detection and scanning system to detect the cell body and selectively not illuminate the cell body. This should reduce the interference produced by the cell body and improve image quality.

Chapter 6

Assembly Kinetics of a Gold-Coordinated Protein Cage

The following chapter is adapted with permission from:

> A. D. Malay, N. Miyazaki, A. Biela, S. Chakraborti, K. Majsterkiewicz, I. Stupka, C. S. Kaplan, A. Kowalczyk, B. M. A. G. Piette, G. K. A. Hochberg, D. Wu, T. P. Wrobel, A. Fineberg, M. S. Kushwah, M. Kelemen, P. Vavpetič, P. Pelicon, P. Kukura, J. L. P. Benesch, K. Iwasaki and J. G. Heddle, An ultra-stable gold-coordinated protein cage displaying reversible assembly, *Nature*, 2019, **569**, 438-442.[158]

The experimental setup used in this chapter was built by myself. The TRAP protein samples were provided by Karolina Majsterkiewicz from the Heddle Lab in the Malopolska Centre of Biotechnology. All the data discussed in the results section was acquired and analysed by myself. The above publication was written by the Heddle Lab with contributions and edits from all of the listed authors as appropriate. The introduction to this chapter has been adapted from the manuscript and discusses the results contributed by the other authors.

6.1 Introduction

Self-assembled, three dimensional symmetrical protein cages have evolved to fulfil many diverse roles in nature such as compartmentalisation and cargo delivery.[159–166] These include, virus-like particles,[167,168] ferritins,[169,170] chaperonins[171] and heat shock proteins.[172] Usually, they are formed from a single monomer unit that self-assembles into a supramolecular structure with well-defined interior, exterior, and monomer interfacing surfaces.[173] A wide range of

cargos can be contained in molecular cages, varying from nucleic acids in virus particles,[168,174] to iron(III) oxide-hydroxide nanoparticles in ferritins.[175,176]

To date, designing new protein cages has used precisely oriented oligomeric protein fusions[177] or the computational design of novel protein-protein interfaces via the introduction of multiple hydrogen-bond and hydrophobic interactions.[178] These methods, however, are limited in the fact that the resulting assemblies are static, i.e. their assembly and disassembly cannot be modulated using an external stimulus. Recently, metal directed protein assembly, inspired by supramolecular coordination chemistry, has emerged as an alternative method to circumvent this limitation.[179] By designing the protein to coordinated metal ions between their surfaces, thereby avoiding protein-protein interactions, the design problem is simplified.[180] Although a wide variety of inducible metal-mediated protein oligomers and arrays have been successfully prepared in this manner,[180–183] the generation of novel three-dimensional cage-like assemblies remains challenging; the closest example prepared so far is an engineered ferritin that can recover the native cage architecture upon Cu^{II} binding at interfacial sites.[184]

Malay *et al.*[158] recently produced a protein cage that uses metal ion coordination for triggering assembly and disassembly. The work was carried out with a cysteine substituted variant of the bacterial ring-shaped protein: trp RNA-binding attenuation protein (TRAP),[185] a protein amenable to genetic modification.[186–188] The TRAP variant formed non-native shell architectures by reacting the protein with triphenylphosphine-derivatised gold nanoparticles through an unknown mechanism. Further investigation led to a double mutant TRAP bearing both a lysine-to-cysteine mutation at residue 35 (K35C), which generates 11 equally spaced thiol groups along the outer rim of the oligomeric ring, and an arginine-to-serine mutation at residue 64 (R64S), which neutralises

positive charges around the central cavity of the ring to prevent non-specific interactions with anionic groups[189] (TRAP(K35C/R64S) - Figure 6.1). By using monosulfonated chloro(triphenylphosphine)gold(I) (Au-TPPMS) as a source of Au^{I}, a simple reaction with TRAP(K35C/R64S) produced an efficient self-assembly of monodisperse spheres ('TRAP-cage'). These TRAP-cages were around 22 nm in diameter and appeared within minutes.

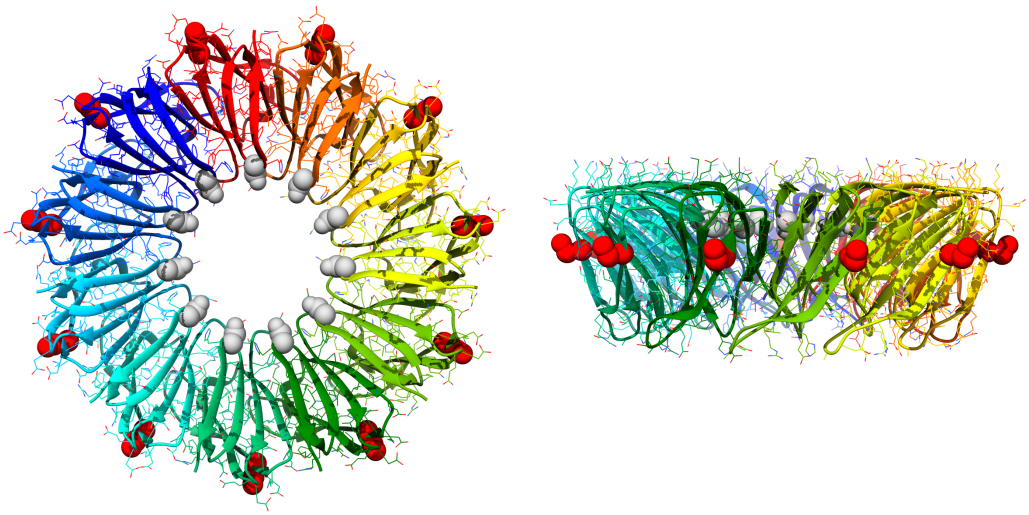


Figure 6.1: Structure of the TRAP(K35C/R64S) 11-mer ring building block, shown in two orthogonal views (based on PDB ID: 4V4F). Substituted residues Cys35 and Ser64 are modelled as red and grey spheres, respectively.[158]

Single particle analysis of cryo-electron micrographs of the TRAP-cages resulted in maps at 3.7 Å resolution showing cage structures with almost equal proportions of the expected left-handed and right-handed chiral structures based on particles counts at 46.5% and 53.5% respectively. The spherical cages showed an unusual structure of 24 uniform rings and six square apertures along three orthogonal axes. This arrangement forms a snub cube, a chiral polyhedron with octahedral symmetry, with each vertex being occupied by a ring. Each TRAP ring maintains its 11-fold rotational symmetry and is surrounded by five neighbouring rings and a gap that defines one side of a square aperture.

Further analysis showed that each TRAP ring was connected to another through two staple-like bridges. Ten of the eleven Cys35 side chains of each TRAP(K35C/R64S) ring aligns with the staple positions. The eleventh is left pointing towards the square aperture. The observed enlargement at the midpoint of the staple was deduced to be a Au^{I} ion linearly coordinated between the two proximal thiol ligands.[190] With the exceptions of the 120 staples per cage and some possible hydrogen bonding between the side chains of Asn18 and Asp37, no other ring-ring interactions were observed.

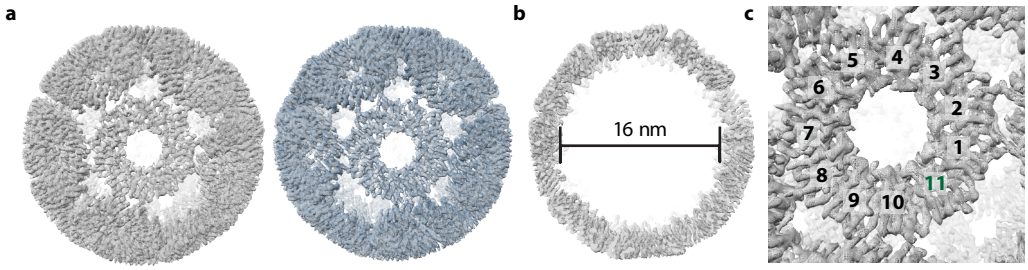


Figure 6.2: **a** Cryo-electron microscopy density maps of the left-handed and right-handed forms of TRAP-cage, refined to 3.7 resolution. **b** Cutaway view of the left-handed map, showing a hollow interior. **c** Magnified view of the left-handed map showing 11-fold rotational symmetry of ring elements and prominent density bridges connecting adjacent rings. Positions 1 to 10 make contacts with neighbouring rings, whereas 11 is unattached and defines the side of a square aperture.

Other metallic ions were tested to see whether the prediction that the resulting geometry of a supramolecular complex is dictated by the inherent symmetry of a protein oligomer together with coordination geometry of the interacting ion.[180] Other thiophilic transition metal ions were tested for their ability to induce cage assembly upon reaction with TRAP(K35C/R64S). Whereas the normally tetrahedrally-coordinated ions Au^{III}, Cu^{I}, and Zn^{II} produced little evidence of cage assembly, the addition of the linearly-coordinating Hg^{II} triggered the formation of uniform cages that were indistinguishable from their gold counterparts.

The TRAP-cages' stability was tested under varying conditions, from heat

to pH. The cages maintained their structure after incubation at 95 °C for 180 min. Similarly the cages remained stable at pHs ranging from 3 to 12 and in the presence of urea (2 to 7 M) and sodium dodecyl sulfate (0.5 to 5 %), consistent with other studies into the stabilising effects of metal coordination.[191,192] However, despite their stability, cage formation was fully reversible. The cages broke apart upon addition to millimolar levels of reducing agents, and it is thought that this is achieved through a ligand displacement mechanism.[193]

The study suggests a possible avenue for building large capsid-like proteins using homomeric components. TRAP-cages are large, shell structures built from a homo-oligomer, something that has been rarely reported.[194] By contrast, viruses build shells of more than 60 subunits,[195] requiring controlled switching between different oligomeric forms.[196] The general stability of the TRAP-cage and its controllable disassembly hints at potential applications as an intracellular delivery agent. To achieve this, more must be understood about the assembly and disassembly kinetics of the cage under a variety of conditions. This chapter presents preliminary experiments to probe the assembly kinetics of the TRAP cage using mass photometry experiments.

6.2 Methods

Gold Compounds

Chloro[diphenyl(3-sulfonatophenyl)phosphine]gold(I) sodium salt hydrate (Au-TPPMS) was purchased from STREM Chemicals UK and reconstituted in Mili-Q to 5 mM stock concentration or in 50 mM Tris-HCl, pH 7.9, 150 mM NaCl to 10 mM stock concentration before use.

Single-molecule Mass Photometry

The iSCAT setup with numerical aperture filtering was adapted from that described previously.[8] The details of the experimental setup capable of single molecule mass photometry are discussed in section 3.3.

Low Monomer Concentration Experiments (< 100 µM)

For iSCAT, a 445 nm diode laser (Lasertack) was used. A Point Grey (GS3-U3-23S6M-C) CMOS camera was used with a pixel size of 5.86 µm, a 4f ratio of 1.5 and an imaging lens of 500 mm. The effective magnification was 250× and pixel size was 23.4 nm px^{-1}.

High Monomer Concentration Experiments (100 µM)

For iSCAT, a 635 nm diode laser (Lasertack) was used. A Point Grey (GS3-U3-23S6M-C) CMOS camera was used with a pixel size of 5.86 µm, a 4f ratio of 1.75 and an imaging lens of 500 mm. The effective magnification was 291.7× and pixel size was 20.1 nm px^{-1}.

Data Acquisition and Analysis

Low Monomer Concentration Experiments (< 100 µM)

The camera was run at 1 kHz and the recorded images were time-averaged one hundred times and pixel-binned 5 × 5 before saving. This gives an effective frame rate of 10 Hz and pixel size of 117 nm. This ensured a sufficient SNR to detect the 90 kDa rings.

A sample of TRAP(K35C/R64S) protein in cage buffer was incubated at room temperature in a 1:1 ratio at various concentrations in the range of 0.1 to 1 µM and also in the absence of Au-TPPMS.

The incubated samples were introduced into a flow cell as described in chapter 4.2 and allowed to bind non-specifically to the glass surface. After

addition to the flow cell, the acquisition software was triggered and the sample was measured for 1 minute.

For the time series data, at various time points beginning 30 s after mixing the two components, the sample was flowed into a flow cell, the acquisition software was triggered, and the sample was measured for 1 minute.

High Monomer Concentration Experiments (100 µM)

The camera was run at 1 kHz and the recorded images were time-averaged twofold and pixel-binned 5 × 5 before saving. This gives an effective frame rate of 500 Hz and pixel size of 100 nm. At this imaging speed, the sensitivity was insufficient to detect individual 90 kDa subunits, producing a cut-off at 200 kDa for the smallest detectable objects.

A sample of TRAP(K35C/R64S) protein in cage buffer and Au-TPPMS was reacted at room temperature in a 1:1 ratio at 100 µM each. At various time points, beginning 30 s after mixing the two components, 5 µL of the mixture was diluted to 10 µM and immediately added to a well of a silicon gasket (3 mm diameter, 1 mm thickness) fixed to a microscope coverslip (#1.5, 24 mm × 52 mm, Menzel Glazer) already containing 15 µL of cage buffer and mixed with the volume of the 5 µL micro-pipette. Fifteen seconds after addition of sample to the well, the acquisition software was triggered and the sample was measured for 30 s.

Image Analysis

Image analysis was performed using the method described in chapter 3.3 to extract the masses of the observed particles. Kernel density estimates for each sample were generated using a Gaussian kernel with a fixed bandwidth.

6.3 Results and Discussion

Mass Photometry Measurement of TRAP(K35C/R64S)

Initially, the distribution of TRAP rings was measured in the absence of Au-TPPMS. As expected, we found a distribution with the majority of species at 90 kDa - the mass expected for a single 11-mer ring. Increasingly small peaks were observed corresponding to higher oligomers (dimers, trimers etc.). To determine whether these were aggregates or properly cysteine coordinated oligomers, a reducing agent, tris(2-carboxyethyl)phosphine (TCEP), was added in excess. As figure 6.3 shows, the higher oligomers did not change on addition of reducing agent, indicating that there is an inherent population of aggregates present at a given concentration, and that these are not early oligomers in the cage formation process.

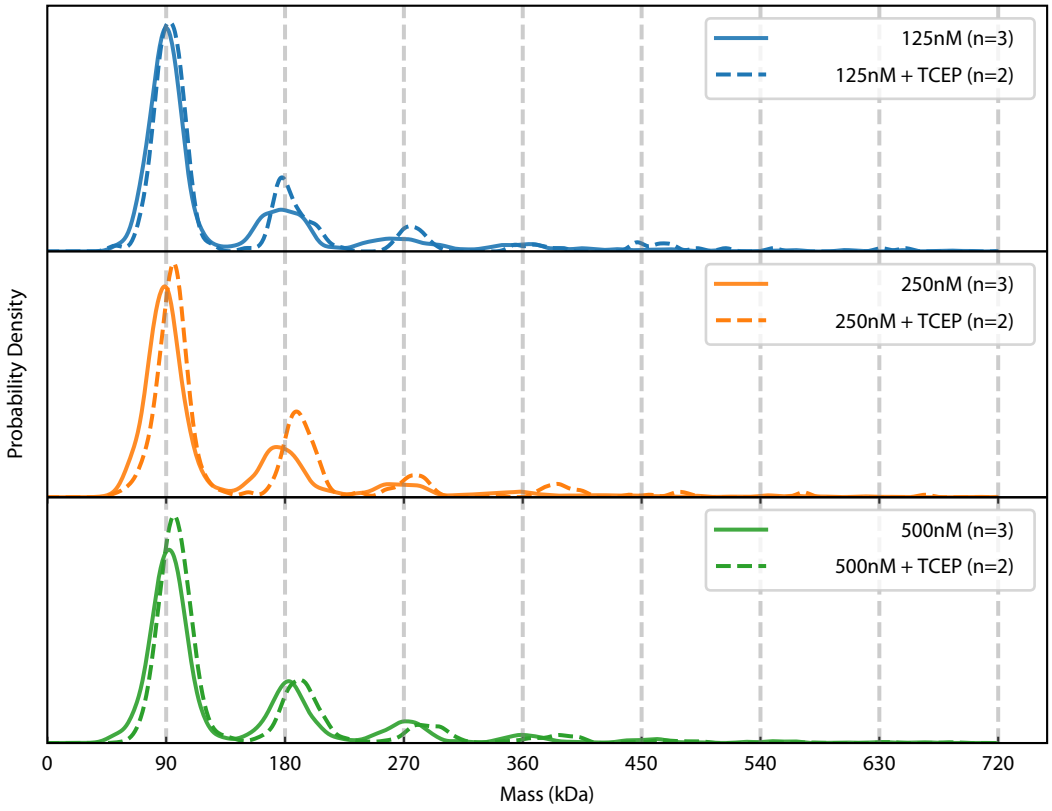


Figure 6.3: Mass kernel density estimates for TRAP(K35C/R64S) without Au. Increasing concentration of monomer from top to bottom. Bandwidth fixed at 5 kDa.

Monitoring Cage Formation

Next, Au-TPPMS was added to a sample of TRAP(K35C/R64S) in a 1:1 Au to TRAP monomer ratio. After incubation for 3 hours, there was no change in the relative populations of oligomers and no new larger species were formed. This was independent of monomer concentration between the range of 100 to 1000 nM.

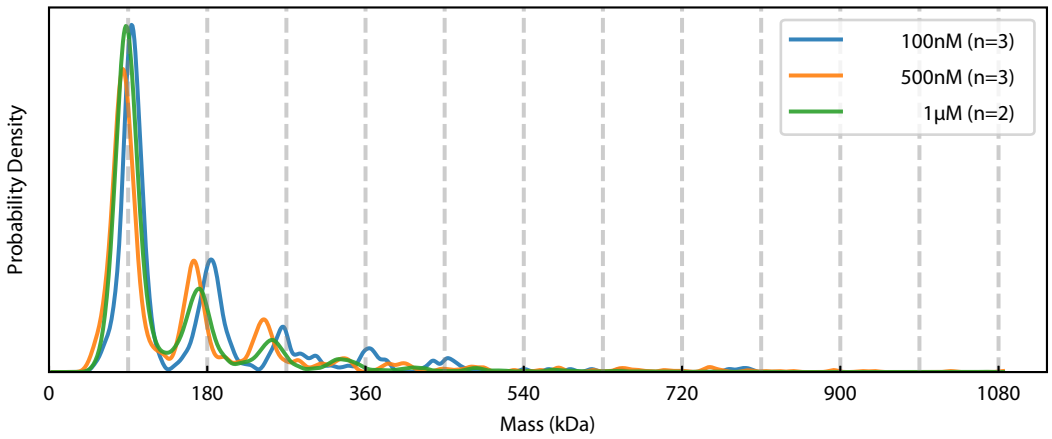


Figure 6.4: Mass kernel density estimates for TRAP(K35C/R64S) with Au in a 1:1 ratio. The distribution is independent of monomer concentration over the range 100 to 1000 nM. Bandwidth fixed at 5 kDa.

To determine whether there was any change in species distribution upon addition of Au-TPPMS at the low monomer concentration, 100 nM monomer was mixed in a 1:1 ratio with Au-TPPMS and measured at time intervals over half an hour. As shown in figure 6.5, each time interval has an identical distribution of species.

In contrast, the same experiment at a higher monomer concentration of 100 µM does show cage assembly. Within 30 s ± 15 s, an intermediate, partly assembled cage forms with a mass of ≈ 1080 kDa. Then, over the next 20 minutes this continues to assemble into the 2160 MDa assembled cage. To determine the proportion of formed cage with time, a Gaussian function constrained to the expected mass of the cage (μ = 2,160 kDa) and width for a

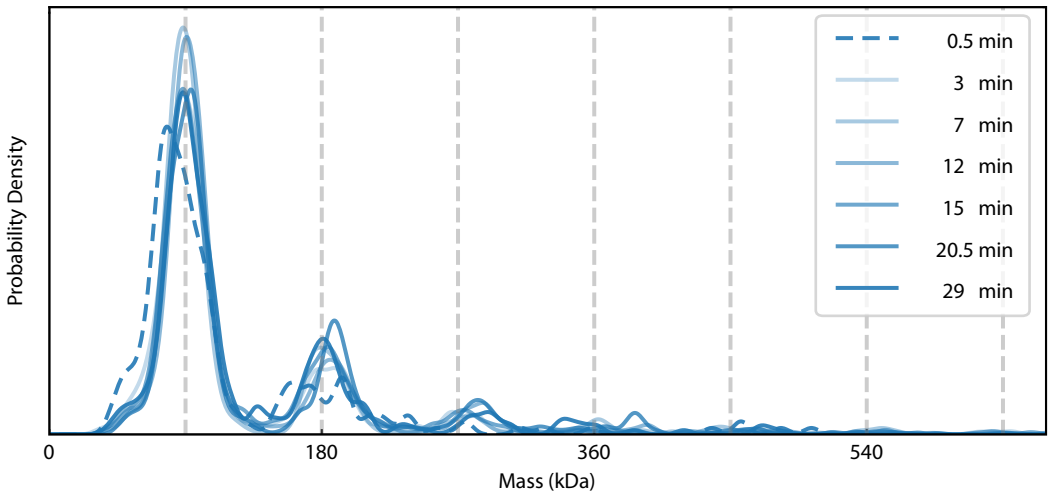


Figure 6.5: Mass kernel density estimates for TRAP(K35C/R64S) with Au over 30 minutes. The distribution is invariant over the time period. Bandwidth fixed at 5 kDa.

single species of that mass (σ = 110 kDa) was fit to a normalised histogram of each time point and the area taken. The σ value off 110 kDa was chosen through extrapolation of values for known calibrants.

The resulting plot of proportion of cage against time was fit to a global association rate fit:

$$f(t) = k(1 - e^{-kt}); \quad \tau = \frac{1}{k} \tag{6.1}$$

where k is the maximum proportion of cage and τ is the formation time.

From the global association fit, an exponential time constant (τ) is obtained with a value of 351 $\pm$ 66 s.

Taken together with the data from figure 6.5 this suggests that there is a critical concentration of TRAP required, below which the cage will not form. Above this critical concentration, the TRAP rings appear to rapidly assemble into an intermediate, partially formed cage, with the cage then forming from this intermediate.

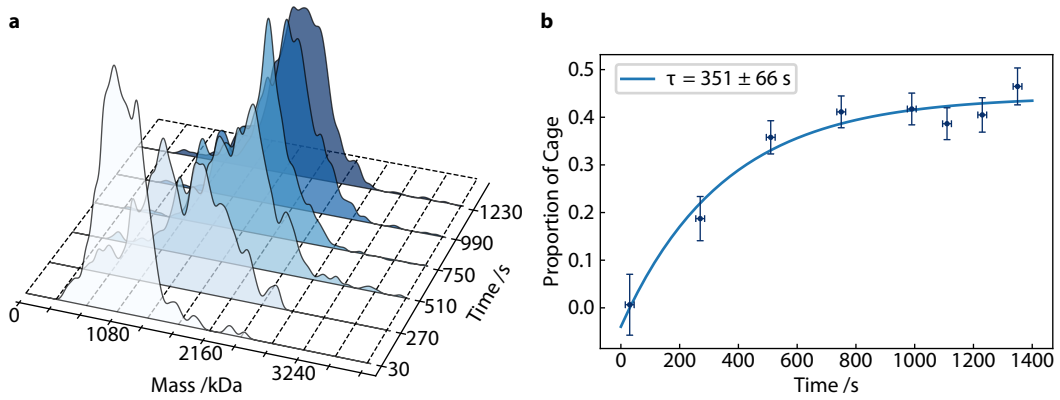


Figure 6.6: **a** Time series of cage formation at high TRAP(K35C/R64S) concentration. Bandwidth fixed at 40 kDa. **b** Extracted assembly kinetics. The horizontal error bars represent 15 s, as dictated by the length of a single measurement; the vertical error bars show the standard error on the area of Gaussian fit, calculated from the covariance matrix of the fit parameters.

6.4 Conclusion and Outlook

The data presented in this chapter demonstrates iSCAT's ability to determine kinetic information from biological systems. It presents the first insight into the mechanism of assembly of TRAP cages by tracking intermediate formation over the time period of minutes. The observation of cage formation above 100 µM monomer concentration and the absence of cages at lower concentrations suggests there exists a critical concentration required for cage formation. The obvious next step would be to determine this concentration, which we know must lie in the range 1 to 100 µM.

The initial intermediate at 1080 kDa forms rapidly within 30 s at 100 µM monomer concentration. Through careful assay optimisation, iSCAT may be able to see the steps taken to form this intermediate and thereby further deduce kinetic information about this system.

Another question of interest is how the cage size varies with varying TRAP:Au ratios. The work to date has always had a 1:1 ratio; iSCAT would be able to determine whether, if by reducing the available gold, smaller cages

can be made to form, or if we just see partially formed cages.

Chapter 7

Determining the Dissociation Constant of a Dimeric System with Mass Photometry

7.1 Introduction

Protein-protein interactions are an essential aspect of biological function and communication, both at the cellular and systems level.[197] These interactions can be roughly grouped into two classes: homologous interactions, such as homo-oligomerisation, and heterologous interactions, such as enzyme-substrate or antibody-antigen interactions.[198] In order to attain a more in-depth understanding of the complex molecular relationships in living systems, one needs a better understanding of protein-protein interactions, and therefore a reliable technique to quantify them is required.

Historically, ligand-receptor binding assays were performed by labelling the ligand with radioactive isotopes.[199] As early as the 1960's, these radioligand binding assays were being used in pharmacology studies.[200] Based on occupation theory,[201] radioligand binding assays would measure binding competition between labelled and unlabelled ligand and compare the equilibrium displaced radioligand with that of samples with known concentrations of radioligand.[202] The key advantage of radioligand binding assays is their sensitivity. Tritiated ligands are reported to be detected down to pM concentrations and iodinated labels to fM.[202] The main drawback with these assays is the need for very careful design, and optimisation of each individual assay. This will eliminate

any substance with an affinity for the receptor that will interfere with the binding competition of the radioligand and the ligand being studied. The health risks and necessary precautions required when using radioactive samples should also be considered disadvantageous, although this is now circumvented, at the cost of sensitivity, through the use of fluorescent rather than radioactive labels.[202]

Another technique which uses fluorescence to measure protein-protein interactions is fluorescence anisotropy. The technique relies on a short lifetime of a fluorescent label compared to the labelled molecule's rotational motion.[203,204] By illuminating with plane polarised light one can excite the fluorescent dipole with a given polarity which will then lead to a change in polarisation of the emitted photon, relative to the illumination, as the dipole tumbles in solution. Slow rotation of a molecule in solution will lead to a highly anisotropic fluorescence emission, whereas fast tumbling will lead to a low isotropic emission.[6] From the level of anisotropy of the detected emission one can infer whether two proteins, one labelled and one unlabelled, are bound as the change in mass will lead to slower rotation in solution. Fluorescence anisotropy is a real-time, solution phase technique that should present very little interference to the protein binding. However, the technique is limited in measuring binding constants tighter than 1 nM, as the signal from such low concentrations of sample is too low to accurately measure.[203]

Nowadays, other biophysical methods are more commonly employed in order to quantify protein-protein interactions, including: analytical ultracentrifugation (AUC), isothermal titration calorimetry (ITC), surface plasmon resonance (SPR), and biolayer interferometry (BLI).

Analytical ultracentrifugation instrumentation consists of a centrifuge capable of measuring concentration gradients of proteins under centrifugal force,

typically with an optical absorption method.[206] There are two main modes of operation for AUC: sedimentation velocity and sedimentation equilibrium, as depicted in figure 7.1. Sedimentation velocity experiments operate at high rotor speeds, and each species within the sample forms boundaries based on its mass and shape. This enables the estimation of the sedimentation coefficient, diffusion coefficient, molecular weight, and ultimately equilibrium constants of interacting species.[207,208] Sedimentation equilibrium experiments operate at lower rotor speeds; this allows the centrifugal force to be opposed by and reach equilibrium with the diffusion of the species involved. The time-invariant exponential concentration gradient allows for the extraction of molecular weight, stoichiometry, binding affinity, and virial coefficient of interacting proteins from thermodynamic theory.[209]

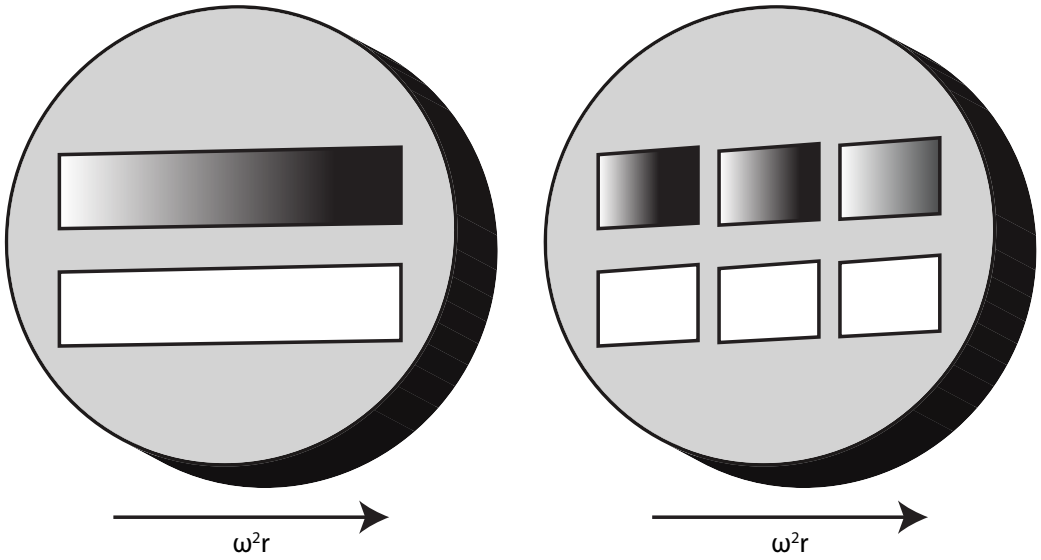


Figure 7.1: A schematic of the two modes of AUC. In sedimentation velocity experiments (left) a two-sector cell is used: one with sample and one as a reference. The sample is measured at regular time intervals. In sedimentation equilibrium experiments (right), a six-sector cell with three loading concentrations is usually employed. The sample is centrifuged for a fixed period of time. ω is the angular velocity and r is the radius of the rotor. $\omega^2 r$ is the angular acceleration of the rotor. This figure is reproduced with permission from J. L. Cole, *et al.*, Analytical Ultracentrifugation: Sedimentation Velocity and Sedimentation Equilibrium, *Methods in Cell Biology*, 2008, **84**, 143-179. ©Elsevier 2008[205]

AUC is a label-free technique capable of measuring binding affinities in the range of 10 nM to 100 µM.[210] The technique can study molecules with molecular masses in the range of 1 to 100 kDa.[210] AUC's main disadvantage is the length of time taken for the experiment to run, typically between 12 to 16 h. This, together with experimental considerations of physical phenomena such as sedimentation, back diffusion, and viscosity, can make development of an AUC assay time consuming and costly.[211]

Isothermal titration calorimetry takes a direct measurement of heat change in molecular binding during a gradual titration, as shown in figure 7.2. Two sample cells, one with water and one with the receptor, are held inside an adiabatic jacket. The temperature difference between the two cells is maintained at 0 °C by two heaters. The instrument outputs the power required to maintain this zero temperature difference upon binding of ligands to the receptors.

From the heat change, an enthalpy of binding and dissociation constant can be calculated, and in turn, other thermodynamic properties, such as Gibb's energy of reaction and entropy change. The measurement is taken by injecting the sample into a cell which is equilibrated with a reference cell. The sample cell becomes warmer than the reference cell, leading to a downwards peak in the signal. The heat released is calculated by integrating the peaks.

ITC is a high sensitivity and high automation technique, making it suitable for many different samples.[200] It is also an *in situ* and non-destructive label-free method, so one doesn't need to worry about surface interactions, label effects, or loss of sample when taking the measurement.[213,214] ITC has been shown to have high precision and reproducibility, with error on the measurement of binding constants typically in the range of 5%.[215] Additionally, it can measure binding affinities in the range of 10 nM to 1 mM, heat effects as small as 0.1 µcal and heat rates as small as 0.1 µcal/s, making it a robust and sensitive technique.[216–218]

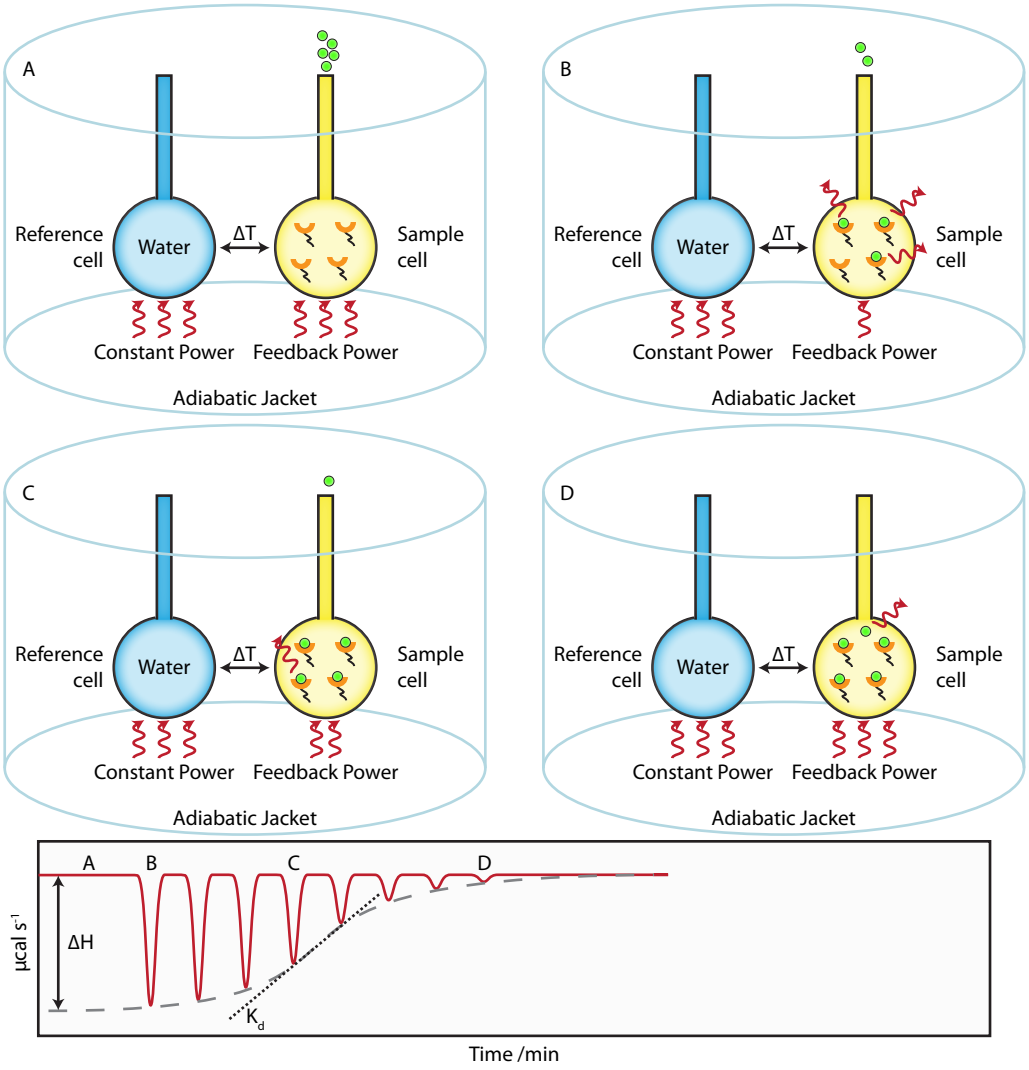


Figure 7.2: A schematic of an ITC experiment. **A** The initial setup of the reference and sample cells with a zero temperature difference ($\Delta T = 0$). **B-D** The change in temperature difference between the two cells induced as ligand is titrated against the receptor is converted into power required to maintain $\Delta T = 0$. As the titration proceeds, the receptors become saturated with the ligand, so that fewer interactions occur and, consequently, the heat change decreases, until the receptor is saturated and the instrument detects only heat change due to ligand dilution. The figure is adapted with permission from A. Saponaro, Isothermal Titration Calorimetry: A Biophysical Method to Characterize the Interaction between Label-free Biomolecules in Solution. *Bio-protocol*, **8**, e2957.[212]

ITC, however, requires relatively large sample volumes, limiting its use for molecules that are difficult to prepare.[214] It is also difficult to measure complex formation when the binding enthalpy is low, resulting in low SNR, and when the binding process is very slow.

Surface plasmon resonance measures the change in the refractive index as the molecules bind to the surface of a biosensor, as shown in figure 7.3. It is a label-free, optical based method and enables real-time quantification of binding kinetics and affinities.[220] In the most commonly used SPR instruments,[221–223] the sensor surface is coated in a thin layer of gold, to which the protein receptor molecules are immobilised. A continuous flow of aqueous medium flows through the sample and the ligand is injected into the solution. As the ligand binds to the receptor proteins the refractive index at the surface increases. This is quantified in response units (RU) by measuring a change in reflection angle (θ_{spr}) between the normal and the sharp resonant dip in the intensity of p-polarised light totally internally reflected at the surface. After all binding sites are occupied, a blank solution is flowed through and the bound ligands dissociate causing a decrease in RU. The RU curves produced are then used to extract association and dissociation rate constants, and thereby also binding constants.[224]

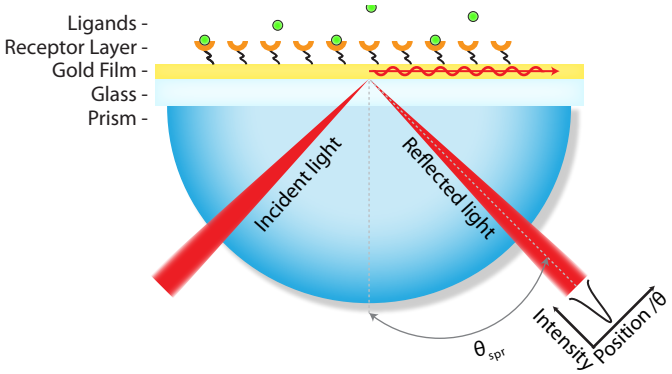


Figure 7.3: A schematic of a typical SPR experiment. A beam of p-polarised light is focused and totally internally reflected at a gold film. When surface plasmon resonance occurs, a sharp dip in the reflected light is observed at a defined angle (θ_{spr}). As ligands bind to the receptors immobilised on the surface, the refractive index changes, causing time dependent changes in θ_{spr}. This figure is adapted with permission from G. De Crescenzo, *et al.*, Kinetic Characterization by Surface Plasmon Resonance-Based Biosensors: Principle and Emerging Trends, *Cellular and Molecular Bioengineering*, 2008, **1**, 204-215. ©Springer Nature 2008[219]

SPR is an effective method to measure real-time binding. However, as it relies on measuring association and dissociation kinetics, if either of these processes are too fast ($> 10^{-6}$ $M^{-1}\,s^{-1}$) or slow (longer than the timescale of the experiment), the technique becomes unreliable.[225,226] SPR can also measure higher binding affinities than ITC, typically in the range of 1 pM to 10 µM.[214] Due to SPR's ability to measure kinetic parameters of the system, it can also differentiate between interactions with similar binding affinities but different kinetics, providing more information about the interaction than other binding assays. SPR, however, is not typically suited to high throughput assays.[225] It is also reliant on surface immobilisation of the receptor protein, which in most cases would have some effect on the binding of the ligand through changes of conformational, translational, and rotational entropies.[227]

Another method that uses a biosensor is bio-layer interferometry. BLI, an optical technique, measures the interference pattern generated when white light reflects from two surfaces on the biosensor: the immobilised receptor layer and an internal reference layer. As figure 7.4 shows, when ligands bind to the the layer of receptors, the optical thickness of that layer increases, leading to a wavelength shift in the reflected intensity. Compared to SPR, BLI offers

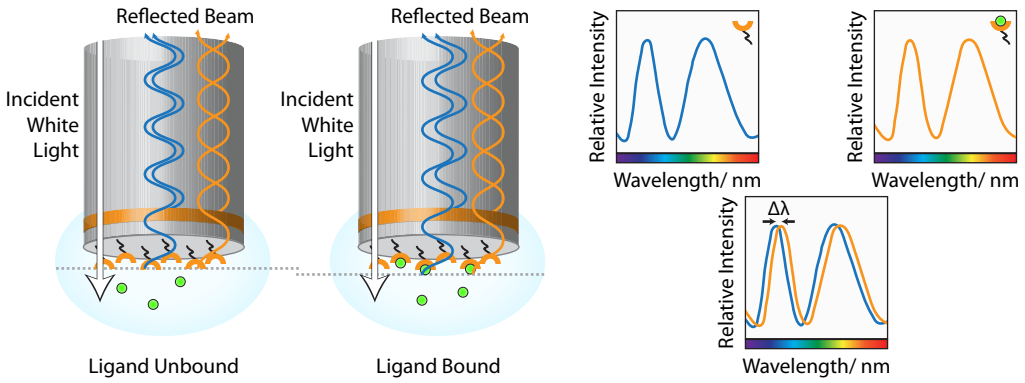


Figure 7.4: A schematic of a typical BLI experiment. When the ligand binds to the receptor, the optical depth of the sample changes, causing a wavelength shift ($\Delta\lambda$) in the interferometric reflected light. Figure adapted from public domain content.

a much higher throughput due to the ability to run the experiment using 96-well plates and without micro-fluidics.[228] BLI also allows for the recovery of the sample, an important factor for many applications. Again, however, BLI requires immobilisation of the protein to the biosensor surface.

The techniques mentioned above each have their own advantages and limitations. This chapter will discuss work carried out to test mass photometry's suitability as an alternative method to quantify physical properties of protein-protein interactions. Like the above techniques, mass photometry is an entirely label-free method, however it does have the advantage of being a truly single molecule technique. By being able to measure all species present in the sample, at the single molecule level, mass photometry has the added benefit of offering information about the individual species within the population rather than just an ensemble average. Similarly to SPR and BLI, mass photometry measurements operate at a substrate surface. However this measurement is taken at the point of the species binding to the glass surface, from solution. Therefore it is reasonable to assume that this should not overly interfere with the measurement. Mass photometry also requires very little sample, typically requiring around 15 µl of sample at concentrations in the high pM to low nM range.

To lay the groundwork for mass photometry's development as a tool for quantifying protein-protein interactions, we opted to measure the dissociation constant of a simple monomer-dimer equilibrium: that of $\alpha\beta$-tubulin. Tubulin is a GTP hydrolysing heterodimer, consisting of an α and a β tubulin monomer. The α and β tubulins share 40% amino acid sequence and their structures are essentially identical, with each monomer being formed by a core of two β-sheets surrounded by α-helices.[229] Conveniently, the two tubulins have near-identical mass (55 kDa), and as our experiments identify species by mass determination,

we will, for the purpose of this work, refer to the two tubulins as the monomer population for the remainder of this chapter.

The choice to study the tubulin monomer-dimer equilibrium was based on several factors. The primary reason is tubulin's biological relevance. Tubulin dimers oligomerise to form microtubules, large tube like structures that play essential roles in cellular structure, division, and transport.[230] An essential aspect of microtubule function is their ability to switch between polymerisation and depolymerisation stochastically, a process based on nucleotide binding and hydrolysis at the dimer level.[230] Each monomer of tubulin binds one GTP molecule; α tubulin is non-exchangeable, while β tubulin is exchangeable. A better understanding of the nature of the dimer's stability will help us to understand the stability of the microtubule as a whole. In addition to its biological relevance, tubulin is thought to have a dissociation constant in the nM range.[231] Despite this fact however, the literature still reports values over

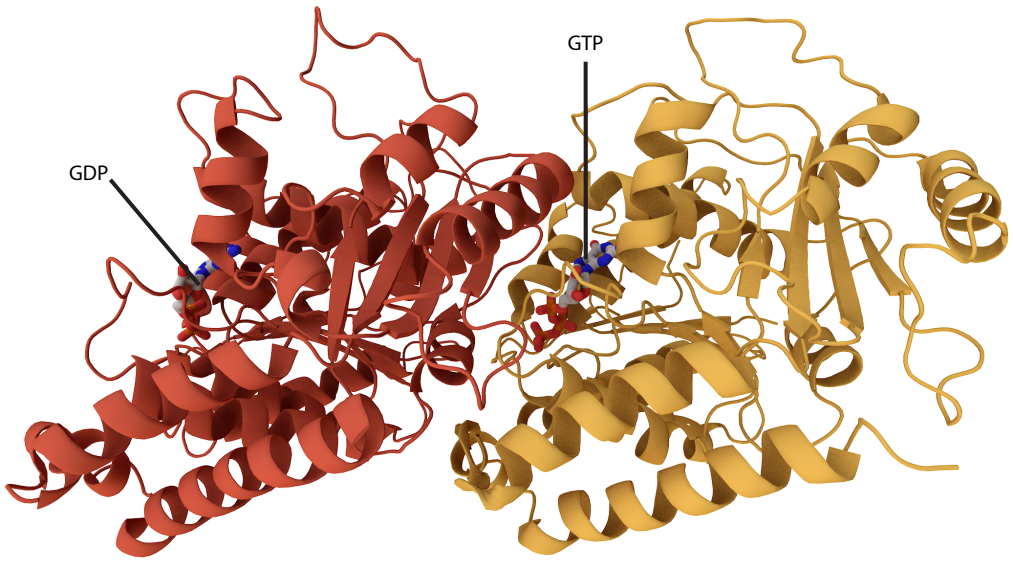


Figure 7.5: Ribbon diagram of the tubulin dimer. α tubulin (yellow) has GTP bound in the non-exchangeable site. β tubulin (red) has GDP bound in the exchangeable site. Figure adapted from content by Thomas Splettstoesser (licensed under CC BY-SA 4.0), original content based on PDB ID: 1JFF. Structure produced by Löwe *et al.*.[230]

a range of two orders of magnitude.[232–240] Lastly, tubulin was chosen due to the simplicity of the protein-protein interaction involved: two proteins that are technically different, but with similar masses, dimerising with no larger oligomeric species forming in the absence of GTP.

7.2 Methods

Tubulin Purification

Tubulin was purified from porcine brain by the Surrey group, Francis Crick Institute, as described.[241]

Single-molecule Mass Photometry

The iSCAT setup with numerical aperture filtering was adapted from that described previously.[8] The details of the experimental setup capable of single molecule mass photometry are discussed in section 3.3. For iSCAT, two setups, one with a blue laser and one with a green, were used. The green setup used a 520 nm diode laser (Lasertack). A Point Grey (GS3-U3-23S6M-C) CMOS camera was used with a pixel size of 5.86 µm, a 4f ratio of 1.2 and an imaging lens of 500 mm. The effective magnification was 200× and pixel size was 29.3 nm px^{-1}.

The blue setup used a 445 nm diode laser (Lasertack). A Point Grey (GS3-U3-23S6M-C) CMOS camera was used with a pixel size of 5.86 µm, a 4f ratio of 1.5 and an imaging lens of 500 mm. The effective magnification was 250× and pixel size was 23.4 nm px^{-1}.

Sample Preparation

A sample of 33 µM tubulin was diluted in Brinkley BR buffer 1980 (BRB80) (80 mM K-PIPES, 1 mM $MgCl_2$, 1 mM EGTA, titrated to pH 6.8 with KOH)

to concentrations in the range of 1 to 40 nM total monomer concentration ($[M]_{TOT}$). All dilutions were left on ice to equilibrate for 20 min. 15 µL of the equilibrated samples were added to a well of a silicon gasket (3 mm diameter, 1 mm thickness) fixed to a microscope coverslip (#1.5, 24 mm × 52 mm, Menzel Glazer) and allowed to bind non-specifically to the glass surface. After addition to the gasket, the acquisition software was triggered and the sample was measured for 2 min. Each concentration was repeated several times.

Acquisition Parameters

The camera was run at 1 kHz and the recorded images were time-averaged 25-fold and pixel-binned 3 × 3 before saving. This gave an effective frame rate of 40 Hz and pixel size of 87.9 nm. This ensured a sufficient SNR to detect the 55 kDa monomers.

Image Analysis

Image analysis was performed using the method described in chapter 3.3 to extract the masses of the observed particles. Measurements whose ratiometric movies were deemed to be too noisy (monomer SNR < 2.5) were discarded. For data visualisation, kernel density estimates were generated using a Gaussian kernel with a fixed bandwidth of 5 kDa. Histograms of particle masses were generated and a sum of two 1D Gaussians fit to the two peaks. Histograms with poorly resolved monomer and dimer peaks, due to either too high binding density or mechanical noise, were discarded. The number of counts of monomer and dimer under the two peaks were extracted. The counts were converted to concentrations and a K_d was calculated for each experiment run, as discussed below. For each concentration measured, the number of measurements included in the results ranged from 3 to 7, with a total of 36 measurements.

7.3 Results and Discussion

Determining the Dissociation Constant

Samples of tubulin were equilibrated over a range of concentrations and the distributions of monomer and dimer of each, in the absence of GTP, were measured using mass photometry. As figure 7.6 shows, at a total monomer concentration ($[M]_{TOT}$) around 1 to 2 nM the majority of species detected are monomer. When $[M]_{TOT} = 40$ nM, the monomer and dimer populations are nearly equal.

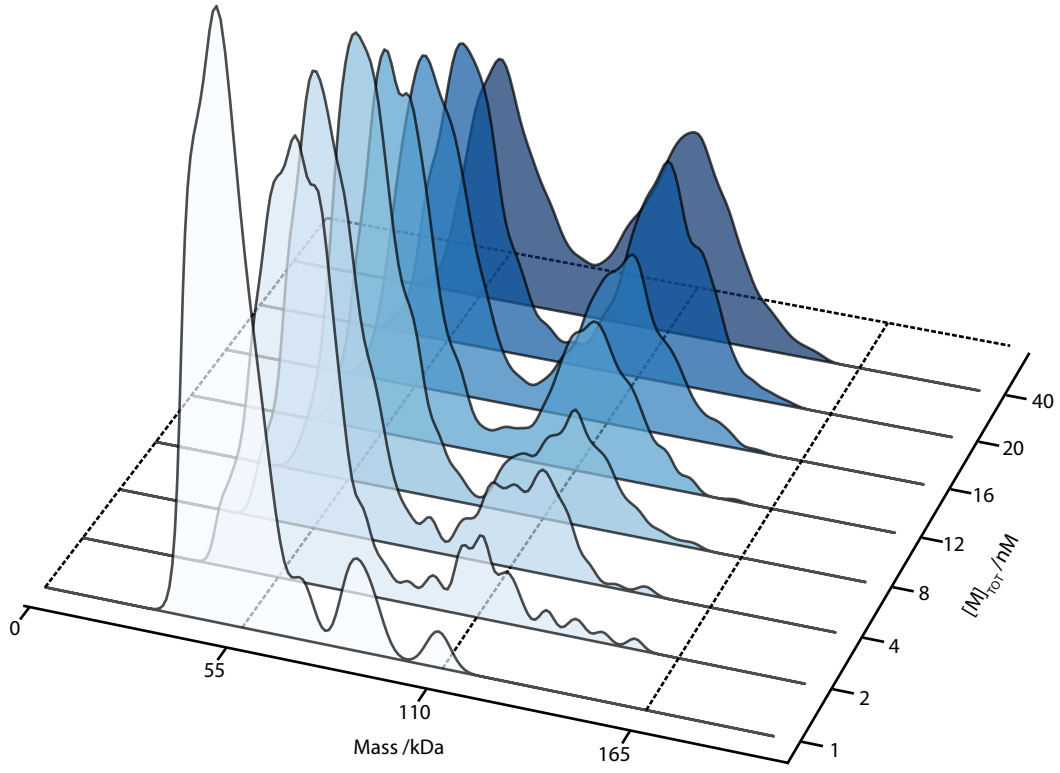


Figure 7.6: Mass kernel density estimates for tubulin at varying concentrations. At low monomer concentration, the majority of species detected are monomeric tubulin (55 kDa). At monomer concentrations of 40 nM, the monomer and dimer peaks are of nearly equal area.

For the following equilibrium between monomer (M) and dimer (D):

$$M + M \rightleftharpoons D \tag{7.1}$$

an equilibrium dissociation constant (K_d) is defined as:

$$K_d = \frac{[M]^2}{[D]} \tag{7.2}$$

For a dimeric system such as this, it can be deduced that the K_d will equal the monomer concentration at which there is a 2:1 ratio of monomer to dimer at equilibrium.

Mass photometry's ability to detect all species present in a sample allowed us to determine the K_d for each sample by simply substituting the concentrations of monomer and dimer into equation 7.2. To convert the number of monomer and dimer species detected (N_M and N_D respectively) from counts into concentrations, we assumed that a constant of proportionality exists equal for both the monomer and the dimer. This assumption requires that the binding events captured in the experiments are representative of the equilibrium populations of monomer and dimer in solution.[8] The constant of proportionality, c, can be determined because we know that the total monomer concentration used is equal to the concentration of monomer plus twice the concentration of dimer:

$$[M]_{TOT} = 2[D] + [M] \tag{7.3}$$

$$[M]_{TOT} = c(2N_D + N_M) \tag{7.4}$$

$$c = \frac{[M]_{TOT}}{2N_D + N_M} \tag{7.5}$$

Once c is calculated for a given sample, a K_d can be determined (detailed in table 7.1):

$$K_d = \frac{cN_M^2}{N_D} \tag{7.6}$$

Figure 7.7 shows the distributions of K_d calculated for different $[M]_{TOT}$. For each individual concentration measured, a similar K_d value was obtained,

with small variations of only a few nM. The global K_d calculated was 8.55 ± 1.21 nM.

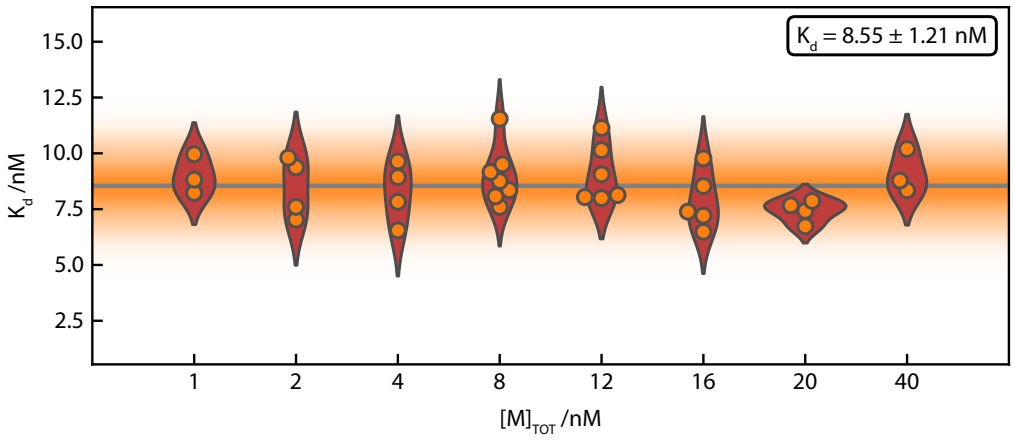


Figure 7.7: K_d measurements of tubulin over a range of concentrations. The grey line indicates the global K_d and the orange shaded area is a Gaussian shading with mean 8.55 and standard deviation 1.21 nM.

7.4 Conclusion and Outlook

At low nM, the K_d for the tubulin dimer makes evolutionary sense. It is thought that monomeric tubulin in the cell can be toxic above low µM concentrations.[242] It is also evident from literature that the source of the tubulin has an effect on its K_d, with porcine, bovine, chicken, rat and human tubulins all being studied.[243]

The data presented in this chapter demonstrates iSCAT's ability to quantify thermodynamic properties of simple protein-protein interactions through a mass photometry measurement. In order to continue this work, more complex systems should be measured, such as antibody-antigen interactions or systems with more than two species present at a given time. Mass photometry's main limitations at this moment are the measurable low mass range and resolution, the concentration limits, and its measurement time. The experiments

carried out can only detect species higher in mass than 30 kDa, preventing the measurement of smaller proteins. The mass resolution limit as discussed in chapter 2 also limits measurement of binding assays when the ligand is of low mass. In terms of measurement time, if the binding or unbinding of interacting species is faster than the timescale of the measurement, error will be introduced due to small fluctuations in local concentrations near the glass surface. The experiments are also still relatively low throughput, but this can be improved in a similar way to SPR or BLI through the use of microfluidics or automatically filled well plates.

Regardless of these current limitations, mass photometry has the potential of becoming a universal analytical tool for quantifying protein-protein interactions.

$[M]_{TOT}$ /nM	N_D	N_M	c /nM	K_d /nM
1	6	70	0.012195122	9.959349593
	8	84	0.01	8.82
	9	89	0.009345794	8.225337487
2	32	158	0.009009009	7.028153153
	28	180	0.008474576	9.8062954
	20	124	0.012195122	9.375609756
	20	105	0.013793103	7.603448276
4	128	359	0.006504065	6.548831301
	108	344	0.007142857	7.826455026
	120	445	0.005839416	9.636253041
	175	614	0.004149378	8.93885003
8	285	551	0.007136485	7.602259887
	157	344	0.012158055	9.163920779
	229	588	0.007648184	11.54722085
	83	167	0.024024024	8.072361518
	138	284	0.014285714	8.349482402
	199	447	0.009467456	9.505943921
	104	221	0.018648019	8.757575758
12	131	201	0.025917927	7.993207261
	487	927	0.006312467	11.13857507
	341	567	0.009607686	9.057963086
	328	587	0.009654063	10.14174009
	78	121	0.0433213	8.131630103
	248	382	0.013667426	8.041957528
16	803	979	0.006189555	7.387700379
	1150	1670	0.004030227	9.77382543
	932	1049	0.005492619	6.485068415
	259	311	0.019300362	7.207530122
	192	256	0.025	8.533333333
20	1021	1027	0.006516781	6.732064253
	703	765	0.009212345	7.668981984
	657	701	0.009925558	7.423788859
	628	694	0.01025641	7.866013392
40	1362	1033	0.010646793	8.341464997
	1466	1250	0.009564802	10.19440818
	4144	3238	0.003470415	8.780420563

Table 7.1: The number of monomer and dimer counts (N_M and N_D), the calculated constant of proportionality (c) between counts and concentration, and the resulting calculated K_d for each equilibrated monomer concentration.

Chapter 8
Summary and Outlook

8.1 Summary

Until now, the major aspect of work using iSCAT has been based around the technical development of the microscope. The intention of this work was to explore the applicability and unique capabilities of iSCAT, applying it to a broad range of questions and biological systems. This work has discussed the implementation of several modifications to the iSCAT microscope, and has shown how they have aided in answering biological questions pertaining to protein interactions and functions.

Beginning with a demonstration of iSCAT's high temporal and spatial precision, we performed single particle tracking on myosin 5a. We observed transient states in the different domains of the molecule, and by combining iSCAT with fluorescence, have correlated their movements. This has provided us with a better understanding of the structural and geometric picture of myosin 5a and we were able to correlate force generation of the stalk domain with the motor domain, furthering our understanding of the role that conformational changes play within the catalytic cycle of the molecule.

We next moved to iSCAT's ability to make label-free measurements. We visualised, with high temporal and spatial resolution, type IV pili extending from the bacteria *Pseudomonas aeruginosa*. To do this, we were required to reduce the phototoxicity of the imaging to the bacterial cells. By shifting the wavelength of light to the red end of the visible spectrum and minimising laser exposure to the cells, we were able to quantify how pili are used to generate

force, and sense the environment around the bacterial cell. We were able to gain insight into how the proteins PilT and PilU participate in the type IV pili mechanism, and suggest a potential sequence of events carried out by the pili when moving under low and high friction conditions.

Following this, we implemented numerical aperture filtering in order to push the sensitivity of label-free detection further. To this end, we were able to track the assembly kinetics of gold coordinated capsid-like protein cages in real time, by monitoring the masses of species in solution. Our measurements were able to extract a global association time constant for the cage formation, and suggested that there exists a critical concentration for assembly to occur.

Lastly, we were able to push iSCAT's size sensitivity lower, in order to measure the distribution of tubulin monomers and dimers in equilibrium at a range of different concentrations. From this, we were able to extract a dissociation constant for the equilibrium and we demonstrated the reproducibility of the technique in making this measurement. By extracting this basic thermodynamic property from this system, we demonstrated iSCAT's ability, in the solution phase, to analyse and quantify protein-protein interactions label-free, at the single molecule level.

8.2 Outlook

The single particle tracking of myosin 5a in *chapter 4* elucidates a structural transition in a motor protein in a dynamic assay. The results presented highlight the benefits of the microscope's high temporal and spatial precision, something which many *in vitro* single molecule assays would benefit from. Through careful optimisation, many other motility assays can be adapted for use on iSCAT and similar structural transitions can be identified.

The results of *chapter 5* are the first to visualise type IV pili, label-free, with high temporal resolution. The ability to quantify the behaviour of extracellular appendages has huge implications in the field of virulence, as these appendages are the first point of contact between the bacterium and host membranes. Through further technical refinement, one will be able to visualise appendages that only extend a short distance from the cell body and, perhaps in combination with mass photometry, cellular excretion can be explored in more depth.

The work set out in *chapters 6 and 7* are some of iSCAT's first steps in measuring kinetic and thermodynamic parameters of biological systems. In addition, the TRAP and tubulin systems span a large range of protein sizes, from 55 kDa to the MDa scale. This highlights the microscope's potential to monitor and quantify the assemblies of highly oligomeric protein systems, from the monomer level to the full assembled complex. A tool with the ability to do this would be an invaluable addition to most biophysical studies, as many biological functions are indeed carried out by macromolecular assemblies.

The different aspects of biophysical systems explored throughout this work demonstrate the potential that iSCAT has as a universal tool to probe biophysical systems. By overcoming the remaining challenges laid out in each chapter of this work, we can probe further the biophysics of the nanoscopic world.

References

1. N. Lane, The unseen World: Reflections on Leeuwenhoek (1677) Concerning little animals', *Philosophical Transactions of the Royal Society B: Biological Sciences*, 2015, **370**, 20140344.

2. A. V. Leeuwenhoek, Observations, communicated to the publisher by Mr. Antony van Leewenhoeck, in a dutch letter of the 9th Octob. 1676. here English'd: concerning little animals by him observed in rain-well-sea- and snow water; as also in water wherein pepper had lain infused, *Philosophical Transactions of the Royal Society of London*, 1677, **12**, 821–831.

3. A. J. Wollman, R. Nudd, E. G. Hedlund and M. C. Leake, From animaculum to single molecules: 300 years of the light microscope, *Open Biology*, 2015, **5**, 150019.

4. K. Thorn, A quick guide to light microscopy in cell biology, *Molecular Biology of the Cell*, 2016, **27**, 219–222.

5. C. A. Combs, Fluorescence microscopy: a concise guide to current imaging methods, *Current protocols in neuroscience*, 2010, **Chapter 2**, Unit2.1.

6. C. P. Toseland, Fluorescent labeling and modification of proteins, *Journal of Chemical Biology*, 2013, **6**, 85–95.

7. G. Young and P. Kukura, Interferometric Scattering Microscopy, *Annual Review of Physical Chemistry*, 2019, **70**, 301–322.

8. G. Young, N. Hundt, D. Cole, A. Fineberg, J. Andrecka, A. Tyler, A. Olerinyova, A. Ansari, E. G. Marklund, M. P. Collier, S. A. Chandler, O. Tkachenko, J. Allen, M. Crispin, N. Billington, Y. Takagi, J. R. Sellers, C. Eichmann, P. Selenko, L. Frey, R. Riek, M. R. Galpin, W. B. Struwe, J. L. Benesch and P. Kukura, Quantitative mass imaging of single biological macromolecules, *Science*, 2018, **360**, 423–427.

9. M. Choi, S. J. Kwok and S. H. Yun, In vivo fluorescence microscopy: Lessons from observing cell behavior in their native environment, *Physiology*, 2015, **30**, 40–49.

10. S. Uphoff, in *Methods in Molecular Biology*, Humana Press Inc., 2016, vol. 1431, pp. 221–234.

11. S. Shashkova and M. C. Leake, Single-molecule fluorescence microscopy review: shedding new light on old problems, *Bioscience reports*, 2017, **37**, 4.

12. F. Rost, in *Encyclopedia of Spectroscopy and Spectrometry*, ed. J. C. Lindon, Elsevier, Oxford, 1999, pp. 565–570.

13. M. Renz, Fluorescence microscopy-A historical and technical perspective, *Cytometry Part A*, 2013, **83**, 767–779.

14. R. M. Dickson, A. B. Cubittt, R. Y. Tsient and W. E. Moerner, On/off blinking and switching behaviour of single molecules of green fluorescent protein, *Nature*, 1997, **388**, 355–358.

15. E. C. Jensen, Use of Fluorescent Probes: Their Effect on Cell Biology and Limitations, *The Anatomical Record: Advances in Integrative Anatomy and Evolutionary Biology*, 2012, **295**, 2031–2036.

16. R. Alford, H. M. Simpson, J. Duberman, G. C. Hill, M. Ogawa, C. Regino, H. Kobayashi and P. L. Choyke, Toxicity of Organic Fluorophores Used in Molecular Imaging: Literature Review, *Molecular Imaging*, 2009, **8**, 7290.2009.00031.

17. V. Magidson and A. Khodjakov, Circumventing Photodamage in Live-Cell Microscopy, *Methods in Cell Biology*, 2013, **114**, 545–560.

18. N. Ji, J. C. Magee and E. Betzig, High-speed, low-photodamage nonlinear imaging using passive pulse splitters, *Nature Methods*, 2008, **5**, 197–202.

19. L. C. Zanetti-Domingues, C. J. Tynan, D. J. Rolfe, D. T. Clarke and M. Martin-Fernandez, Hydrophobic Fluorescent Probes Introduce Artifacts into Single Molecule Tracking Experiments Due to Non- Specific Binding, *PLoS ONE*, 2013, **8**, e74200.

20. H. Amartely, O. Avraham, A. Friedler, O. Livnah and M. Lebendiker, Coupling Multi Angle Light Scattering to Ion Exchange chromatography (IEX-MALS) for protein characterization, *Scientific Reports*, 2018, **8**, 6907.

21. A. P. Minton, *Recent applications of light scattering measurement in the biological and biopharmaceutical sciences*, 2016.

22. P. J. Wyatt, *Light scattering and the absolute characterization of macromolecules*, 1993.

23. J. Ortega-Arroyo and P. Kukura, Interferometric scattering microscopy (iSCAT): new frontiers in ultrafast and ultrasensitive optical microscopy, *Physical Chemistry Chemical Physics*, 2012, **14**, 15625.

24. A. A. Deniz, S. Mukhopadhyay and E. A. Lemke, Single- molecule biophysics: at the interface of biology, physics and chemistry, *Journal of The Royal Society Interface*, 2008, **5**, 15–45.

25. J. J. Lister and P. M. Roget, XIII. On some properties in achromatic object-glasses applicable to the improvement of the microscope, *Philosophical Transactions of the Royal Society of London*, 1830, **120**, 187–200.

26. H. Siedentopf and R. Zsigmondy, Uber Sichtbarmachung und Größenbestimmung ultramikoskopischer Teilchen, mit besonderer Anwendung auf Goldrubingläser, *Annalen der Physik*, 1902, **315**, 1–39.

27. S. H. Gage, Modern Dark-Field Microscopy and the History of Its Development, *Transactions of the American Microscopical Society*, 1920, **39**, 95.

28. A. S. G. Curtis, The Mechanism Of Adhesion Of Cells To Glass, *The Journal of Cell Biology*, 1964, **20**, 199–215.

29. J. S. Ploem, *Reflection-contrast microscopy as a tool for investigation of the attachment of living cells to a glass surface*, Blackwell, Oxford, 1975.

30. P. Kukura, M. Celebrano, A. Renn and V. Sandoghdar, Imaging a Single Quantum Dot When It Is Dark, *Nano Letters*, 2009, **9**, 926–929.

31. P. Kukura, H. Ewers, C. Mü ller, A. Renn, A. Helenius and V. Sandoghdar, High-speed nanoscopic tracking of the position and orientation of a single virus, *Nature Methods*, 2009, **6**, 923–927.

32. S. Nishikawa, I. Arimoto, K. Ikezaki, M. Sugawa, H. Ueno, T. Komori, A. H. Iwane and T. Yanagida, Switch between Large Hand-Over-Hand and Small Inchworm-like Steps in Myosin VI, *Cell*, 2010, **142**, 879–888.

33. H. Ueno, S. Nishikawa, R. Iino, K. V. Tabata, S. Sakakihara, T. Yanagida and H. Noji, Simple Dark-Field Microscopy with Nanometer Spatial Precision and Microsecond Temporal Resolution, *Biophysical Journal*, 2010, **98**, 2014–2023.

34. K. J. Mickolajczyk and W. O. Hancock, in *Methods in molecular biology (Clifton, N.J.)*, Humana Press Inc., 2018, vol. 1805, pp. 123–138.

35. G. I. Mashanov, D. Tacon, A. E. Knight, M. Peckham and J. E. Molloy, Visualizing single molecules inside living cells using total internal reflection fluorescence microscopy, *Methods*, 2003, **29**, 142–152.

36. G. Mie, Beiträge zur Optik trüber Medien, speziell kolloidaler Metallösungen, *Annalen der Physik*, 1908, **330**, 377–445.

37. T. Wriedt, in *Mie theory: A review*, ed. W. Hergert and T. Wriedt, Springer Berlin Heidelberg, Berlin, Heidelberg, 2012, vol. 169, pp. 53–71.

38. P. A. Baron and K. Willeke, *Aerosol measurement : principles, techniques, and applications*, Wiley, New York, N.Y.; Chichester, 2nd edn., 2001, p. 463.

39. V. Amendola, R. Pilot, M. Frasconi, O. M. Maragò and M. A. Iatì, Surface plasmon resonance in gold nanoparticles: a review, *Journal of Physics: Condensed Matter*, 2017, **29**, 203002.

40. Y. Yang, S. Zhong, K. Wang and J. Huang, Gold nanoparticle based fluorescent oligonucleotide probes for imaging and therapy in living systems, *Analyst*, 2019, **144**, 1052–1072.

41. S. Unser, I. Bruzas, J. He and L. Sagle, Localized Surface Plasmon Resonance Biosensing: Current Challenges and Approaches, *Sensors*, 2015, **15**, 15684–15716.

42. J. Ortega Arroyo, J. Andrecka, K. M. Spillane, N. Billington, Y. Takagi, J. R. Sellers and P. Kukura, Label-free, all-optical detection, imaging, and tracking of a single protein, *Nano Letters*, 2014, **14**, 2065–2070.

43. M. Abercrombie and G. Dunn, Adhesions of fibroblasts to substratum during contact inhibition observed by interference reflection microscopy, *Experimental Cell Research*, 1975, **92**, 57– 62.

44. C. S. Izzard and L. R. Lochner, *Cell-to-substrate Contacts In Living Fibroblasts: An Interference Reflexion Study With An Evaluation Of The Technique*, 1, 1976.

45. J. P. Heath and G. A. Dunn, *Cell To Substratum Contacts Of Chick F1broblasts And Their Relation To The Microfilament System. A Correlated Interference-reflexion And High-voltage Electron-microscope Study*, 1978.

46. L. A. Amos and W. B. Amos, The bending of sliding microtubules imaged by confocal light microscopy and negative stain electron microscopy., *Journal of cell science. Supplement*, 1991, **14**, 95–101.

47. O. Avci, N. L. Ünlü, A. Y. Özkumur and M. S. Ünlü, Interferometric Reflectance Imaging Sensor (IRIS)–A Platform Technology for Multiplexed Diagnostics and Digital Detection., *Sensors (Basel, Switzerland)*, 2015, **15**, 17649–65.

48. T. Fujiwara, K. Ritchie, H. Murakoshi, K. Jacobson and A. Kusumi, Phospholipids undergo hop diffusion in compartmentalized cell membrane, *The Journal of Cell Biology*, 2002, **157**, 1071–1082.

49. K. Lindfors, T. Kalkbrenner, P. Stoller and V. Sandoghdar, Detection and Spectroscopy of Gold Nanoparticles Using Supercontinuum White Light Confocal Microscopy, *Physical Review Letters*, 2004, **93**, 37401.

50. V. Jacobsen, P. Stoller, C. Brunner, V. Vogel and V. Sandoghdar, Interferometric optical detection and tracking of very small gold nanoparticles at a water-glass interface, *Optics Express*, 2006, **14**, 405.

51. H. Ewers, V. Jacobsen, E. Klotzsch, A. E. Smith, A. Helenius and V. Sandoghdar, Label-free optical detection and tracking of single virions bound to their receptors in supported membrane bilayers, *Nano Letters*, 2007, **7**, 2263–2266.

52. J. Andrecka, J. Ortega Arroyo, K. Lewis, R. A. Cross and P. Kukura, Label-free Imaging of Microtubules with Sub-nm Precision Using Interferometric Scattering Microscopy, *Biophysical Journal*, 2016, **110**, 214–217.

53. J. Ortega Arroyo, D. Cole and P. Kukura, Interferometric scattering microscopy and its combination with single- molecule fluorescence imaging, *Nature Protocols*, 2016, **11**, 617–633.

54. D. Cole, G. Young, A. Weigel, A. Sebesta and P. Kukura, Label-Free Single-Molecule Imaging with Numerical- Aperture-Shaped Interferometric Scattering Microscopy, *ACS Photonics*, 2017, **4**, 211–216.

55. M. A. Lieb, J. M. Zavislan and L. Novotny, Single-molecule orientations determined by direct emission pattern imaging, *Journal of the Optical Society of America B*, 2004, **21**, 1210.

56. K. G. Lee, X. W. Chen, H. Eghlidi, P. Kukura, R. Lettow, A. Renn, V. Sandoghdar and S. Götzinger, A planar dielectric antenna for directional single-photon emission and near-unity collection efficiency, *Nature Photonics*, 2011, **5**, 166–169.

57. M. Liebel, J. T. Hugall and N. F. van Hulst, Ultrasensitive Label-Free Nanosensing and High-Speed Tracking of Single Proteins, *Nano Letters*, 2017, **17**, 1277–1281.

58. K. Häußermann, G. Young, P. Kukura and H. Dietz, Dissecting FOXP2 Oligomerization and DNA Binding, *Angewandte Chemie - International Edition*, 2019, **58**, 7662–7667.

59. G. de Wit, J. S. H. Danial, P. Kukura and M. I. Wallace, Dynamic label-free imaging of lipid nanodomains, *Proceedings of the National Academy of Sciences*, 2015, **112**, 12299–12303.

60. R. Parthasarathy, Rapid, accurate particle tracking by calculation of radial symmetry centers, *Nature Methods*, 2012, **9**, 724–726.

61. B. Zitová and J. Flusser, Image registration methods: a survey, *Image and Vision Computing*, 2003, **21**, 977–1000.

62. L. Yang, R. Parton, G. Ball, Z. Qiu, A. H. Greenaway, I. Davis and W. Lu, An adaptive non-local means filter for denoising live-cell images and improving particle detection, *Journal of Structural Biology*, 2010, **172**, 233–243.

63. J. Andrecka, J. Ortega Arroyo, Y. Takagi, G. de Wit, A. Fineberg, L. MacKinnon, G. Young, J. R. Sellers and P. Kukura, Structural dynamics of myosin 5 during processive motion revealed by interferometric scattering microscopy, *eLife*, 2015, **4**, 5413.

64. K. M. Trybus, Myosin V from head to tail, *Cellular and Molecular Life Sciences*, 2008, **65**, 1378–1389.

65. S. L. Reck-Peterson, D. W. Provance, M. S. Mooseker and J. A. Mercer, Class V myosins, *Biochimica et Biophysica Acta - Molecular Cell Research*, 2000, **1496**, 36–51.

66. A. Yildiz, J. N. Forkey, S. A. McKinney, T. Ha, Y. E. Goldman and P. R. Selvin, Myosin V walks hand-over-hand: Single fluorophore imaging with 1.5-nm localization, *Science*, 2003, **300**, 2061–2065.

67. R. D. Vale, Myosin V motor proteins: Marching stepwise towards a mechanism, *Journal of Cell Biology*, 2003, **163**, 445–450.

68. J. R. Sellers and C. Veigel, Walking with myosin V, *Current Opinion in Cell Biology*, 2006, **18**, 68–73.

69. J. A. Hammer and J. R. Sellers, Walking to work: Roles for class v myosins as cargo transporters, *Nature Reviews Molecular Cell Biology*, 2012, **13**, 13–26.

70. A. D. Mehta, R. S. Rock, M. Rief, J. A. Spudich, M. S. Mooseker and R. E. Cheney, Myosin-V is a processive actin-based motor, *Nature*, 1999, **400**, 590–593.

71. A. R. Dunn and J. A. Spudich, Dynamics of the unbound head during myosin V processive translocation, *Nature Structural and Molecular Biology*, 2007, **14**, 246–248.

72. J. A. Spudich, The myosin swinging cross-bridge model, *Nature Reviews Molecular Cell Biology*, 2001, **2**, 387–392.

73. T. J. Purcell, C. Morris, J. A. Spudich and H. L. Sweeney, Role of the lever arm in the processive stepping of myosin V, *Proceedings of the National Academy of Sciences of the United States of America*, 2002, **99**, 14159–14164.

74. R. E. Cheney, R. E. Larson, M. V. Coelho, M. S. Mooseker, M. K. O'Shea, J. S. Wolenski, P. Forscher, J. E. Heuser and E. M. Espreafico, Brain myosin-V is a two-headed unconventional myosin with motor activity, *Cell*, 1993, **75**, 13–23.

75. T. Sakamoto, M. R. Webb, E. Forgacs, H. D. White and J. R. Sellers, Direct observation of the mechanochemical coupling in myosin Va during processive movement, *Nature*, 2008, **455**, 128–132.

76. D. Köhler, C. Ruff, E. Meyhöfer and M. Bä hler, Different degrees of lever arm rotation control myosin step size, *The Journal of Cell Biology*, 2003, **161**, 237–241.

77. Y. Sun and Y. E. Goldman, Lever-arm mechanics of processive myosins., *Biophysical journal*, 2011, **101**, 1–11.

78. T. Ando, T. Uchihashi and N. Kodera, *High-Speed AFM and Applications to Biomolecular Systems*, 2013.

79. X. D. Li, H. S. Jung, K. Mabuchi, R. Craig and M. Ikebe, The Globular Tail Domain of Myosin Va Functions as an Inhibitor of the Myosin Va Motor, *Journal of Biological Chemistry*, 2006, **281**, 21789 –21798.

80. W. Yang and H. D. Holland, The Hekpoort paleosol profile in strata 1 at Gaborone, Botswana: Soil formation during the great oxidation event, *American Journal of Science*, 2003, **303**, 187 –220.

81. M. L. Walker, S. A. Burgess, J. R. Sellers, F. F. Wang, J. A. Hammer III, J. Trinick, P. J. Knight, J. A. Hammer, J. Trinick and P. J. Knight, Two-headed binding of a processive myosin to F-actin, *Nature*, 2000, **405**, 804–807.

82. M. Rief, R. S. Rock, A. D. Mehta, M. S. Mooseker, R. E. Cheney and J. A. Spudich, Myosin-V stepping kinetics: A molecular model for processivity, *Proceedings of the National Academy of Sciences*, 2000, **97**, 9482 –9486.

83. G. Cappello, P. Pierobon, C. Symonds, L. Busoni, J. Christof, M. Gebhardt, M. Rief and J. Prost, Myosin V stepping mechanism, *Proceedings of the National Academy of Sciences*, 2007, **104**, 15328 – 15333.

84. H. Lu, G. G. Kennedy, D. M. Warshaw and K. M. Trybus, Simultaneous observation of tail and head movements of myosin v during processive motion, *Journal of Biological Chemistry*, 2010, **285**, 42068–42074.

85. C. Veigel, F. Wang, M. L. Bartoo, J. R. Sellers and J. E. Molloy, The gated gait of the processive molecular motor, myosin V, *Nature Cell Biology*, 2002, **4**, 59–65.

86. G. E. Snyder, T. Sakamoto, J. A. Hammer, J. R. Sellers and P. R. Selvin, Nanometer localization of single fluorescent proteins: Evidence that myosin V walks hand-over- hand via telemark configuration, *Biophysical Journal*, 2004, **87**, 1776–1783.

87. J. N. Forkey, M. E. Quinlan, M. A. Shaw, J. E. Corrie and Y. E. Goldman, Three-dimensional structural dynamics of myosin V by single- molecule fluorescence polarization, *Nature*, 2003, **422**, 399–404.

88. J. F. Beausang, D. Y. Shroder, P. C. Nelson and Y. E. Goldman, Tilting and wobble of Myosin v by high-speed single-molecule polarized fluorescence microscopy, *Biophysical Journal*, 2013, **104**, 1263–1273.

89. M. Ohmachi, Y. Komori, A. H. Iwane, F. Fujii, T. Jin and T. Yanagida, Fluorescence microscopy for simultaneous observation of 3D orientation and movement and its application to quantum rod- tagged myosin V, *Proceedings of the National Academy of Sciences*, 2012, **109**, 5294–5298.

90. Y. Komori, A. H. Iwane and T. Yanagida, Myosin-V makes two brownian 90° rotations per 36-nm step, *Nature Structural and Molecular Biology*, 2007, **14**, 968– 973.

91. P. Karagiannis, Y. Ishii and T. Yanagida, Molecular Machines Like Myosin Use Randomness to Behave Predictably, *Chemical Reviews*, 2014, **114**, 3318–3334.

92. K. Shiroguchi, H. F. Chin, D. E. Hannemann, E. Muneyuki, E. M. de la Cruz and K. Kinosita, Direct observation of the myosin va recovery stroke that contributes to unidirectional stepping along actin, *PLoS Biology*, 2011, **9**, e1001031.

93. N. Kodera and T. Ando, Direct imaging of walking myosin V by high-speed atomic force microscopy, *Methods in Molecular Biology*, 2018, **1805**, 103–122.

94. N. Kodera, D. Yamamoto, R. Ishikawa and T. Ando, Video imaging of walking myosin V by high-speed atomic force microscopy, *Nature*, 2010, **468**, 72–76.

95. T. Okada, H. Tanaka, A. H. Iwane, K. Kitamura, M. Ikebe and T. Yanagida, The diffusive search mechanism of processive myosin class-V motor involves directional steps along actin subunits, *Biochemical and Biophysical Research Communications*, 2007, **354**, 379– 384.

96. K. Shiroguchi, K. Kinosita Jr. and K. Kinosita, Myosin V walks by lever action and Bownian motion, *Science*, 2007, **316**, 1208–1212.

97. A. Ramaiya, B. Roy, M. Bugiel and E. S. äffer, Kinesin rotates unidirectionally and generates torque while walking on microtubules, *Proceedings of the National Academy of Sciences*, 2017, **114**, 10894–10899.

98. J. A. Spudich and S. Watt, The regulation of rabbit skeletal muscle contraction. I. Biochemical studies of the interaction of the tropomyosin-

troponin complex with actin and the proteolytic fragments of myosin., *Journal of Biological Chemistry*, 1971, **246**, 4866–4871.

99. F. Wang, L. Chen, O. Arcucci, E. V. Harvey, B. Bowers, Y. Xu, J. A. Hammer, J. R. Sellers, J. A. Hammer III, J. R. Sellers, J. A. Hammer and J. R. Sellers, Effect of ADP and ionic strength on the kinetic and motile properties of recombinant mouse myosin V, *Journal of Biological Chemistry*, 2000, **275**, 4329–4335.

100. A. R. Dunn and J. A. Spudich, Single-molecule gold-nanoparticle tracking, *Cold Spring Harbor Protocols*, 2011, **6**, 1498–1506.

101. L. S. Churchman, Z. Ökten, R. S. Rock, J. F. Dawson and J. A. Spudich, Single molecule high-resolution colocalization of Cy3 and Cy5 attached to macromolecules measures intramolecular distances through time, *Proceedings of the National Academy of Sciences*, 2005, **102**, 1419–1423.

102. K. E. Miller and M. P. Sheetz, Characterization of Myosin V Binding to Brain Vesicles, *Journal of Biological Chemistry*, 2000, **275**, 2598–2606.

103. L. Talà, A. Fineberg, P. Kukura and A. Persat, Pseudomonas aeruginosa orchestrates twitching motility by sequential control of type IV pili movements, *Nature Microbiology*, 2019, 1.

104. T. R. D. Costa, A. Meir, M. S. Prevost, M. Trokter, G. Waksman, C. Felisberto-Rodrigues and A. Redzej, Secretion systems in Gram-negative bacteria: structural and mechanistic insights, *Nature Reviews Microbiology*, 2015, **13**, 343–359.

105. A. Persat, Bacterial mechanotransduction, *Current Opinion in Microbiology*, 2017, **36**, 1–6.

106. L. L. Burrows, Pseudomonas aeruginosa Twitching Motility: Type IV Pili in Action, *Annual Review of Microbiology*, 2012, **66**, 493–520.

107. A. Persat, C. D. Nadell, M. K. Kim, F. Ingremeau, A. Siryaporn, K. Drescher, N. S. Wingreen, B. L. Bassler, Z. Gitai and H. A. Stone, The Mechanical World of Bacteria, *Cell*, 2015, **161**, 988–997.

108. A. J. Merz, M. So and M. P. Sheetz, Pilus retraction powers bacterial twitching motility, *Nature*, 2000, **407**, 98–102.

109. J. S. Mattick, Type IV Pili and Twitching Motility, *Annual Review of Microbiology*, 2002, **56**, 289–314.

110. R. A. Alm and J. S. Mattick, Genes involved in the biogenesis and function of type-4 fimbriae in Pseudomonas aeruginosa, *Gene*, 1997, **192**, 89–98.

111. A. B. Semmler, C. B. Whitchurch and J. S. Mattick, A re-examination of twitching motility in Pseudomonas aeruginosa, *Microbiology*, 1999, **145**, 2863–2873.

112. J. Koo, S. Tammam, S.-Y. Ku, L. M. Sampaleanu, L. L. Burrows and P. L. Howell, PilF is an outer membrane lipoprotein required for multimerization and localization of the Pseudomonas aeruginosa Type IV pilus secretin., *Journal of bacteriology*, 2008, **190**, 6961–9.

113. M. Wolfgang, Components and dynamics of fiber formation define a ubiquitous biogenesis pathway for bacterial pili, *The EMBO Journal*, 2000, **19**, 6408–6418.

114. P. Chiang, M. Habash and L. L. Burrows, Disparate subcellular localization patterns of Pseudomonas aeruginosa Type IV pilus ATPases involved in twitching motility., *Journal of bacteriology*, 2005, **187**, 829–39.

115. C. B. Whitchurch, M. Hobbs, S. P. Livingston, V. Krishnapillai and J. S. Mattick, Characterisation of a Pseudomonas aeruginosa twitching motility gene and evidence for a specialised protein export system widespread in eubacteria, *Gene*, 1991, **101**, 33–44.

116. C. B. Whitchurch and J. S. Mattick, Characterization of a gene, pilU, required for twitching motility but not phage sensitivity in Pseudomonas aeruginosa, *Molecular Microbiology*, 1994, **13**, 1079–1091.

117. P. Chiang, L. M. Sampaleanu, M. Ayers, M. Pahuta, P. L. Howell and L. L. Burrows, Functional role of conserved residues in the characteristics secretion NTPase motifs of the Pseudomonas aeruginosa type IV pilus motor proteins PilB, PilT and PilU, *Microbiology*, 2008, **154**, 114– 126.

118. M. S. Strom, D. N. Nunn and S. Lory, A single bifunctional enzyme, PilD, catalyzes cleavage and N-methylation of proteins belonging to the type IV pilin family., *Proceedings of the National Academy of Sciences*, 2006, **90**, 2404–2408.

119. V. Pelicic, Type IV pili: e pluribus unum?, *Molecular Microbiology*, 2008, **68**, 827–837.

120. H. Wehbi, E. Portillo, H. Harvey, A. E. Shimkoff, E. M. Scheurwater, P. L. Howell and L. L. Burrows, The peptidoglycan-binding protein FimV promotes assembly of the Pseudomonas aeruginosa type IV pilus secretin., *Journal of bacteriology*, 2011, **193**, 540–50.

121. V. Karuppiah and J. P. Derrick, Structure of the PilM-PilN inner membrane type IV pilus biogenesis complex from Thermus thermophilus., *The Journal of biological chemistry*, 2011, **286**, 24434–42.

122. S. Tammam, L. M. Sampaleanu, J. Koo, P. Sundaram, M. Ayers, P. Andrew Chong, J. D. Forman-Kay, L. L. Burrows and P. L. Howell, Characterization of the PilN, PilO and PilP type IVa pilus subcomplex, *Molecular Microbiology*, 2011, **82**, 1496–1514.

123. E. M. Scheurwater and L. L. Burrows, Maintaining network security: how macromolecular structures cross the peptidoglycan layer., *FEMS microbiology letters*, 2011, **318**, 1–9.

124. N. B. Fulcher, P. M. Holliday, E. Klem, M. J. Cann and M. C. Wolfgang, The Pseudomonas aeruginosa Chp chemosensory system regulates intracellular cAMP levels by modulating adenylate cyclase activity, *Molecular microbiology*, 2010, **76**, 889–904.

125. W. Paranchych, P. A. Sastry, L. S. Frost, M. Carpenter, G. D. Armstrong and T. H. Watts, Biochemical studies on pili isolated from Pseudomonas aeruginosa strain PAO, *Canadian Journal of Microbiology*, 2010, **25**, 1175 –1181.

126. R. A. Alm and J. S. Mattick, Identification of two genes with prepilin-like leader sequences involved in type 4 fimbrial biogenesis in Pseudomonas aeruginosa., *Journal of bacteriology*, 1996, **178**, 3809–17.

127. R. A. Alm, J. P. Hallinan, A. A. Watson and J. S. Mattick, Fimbrial biogenesis genes of Pseudomonas aeruginosa: pilW and pilX increase the similarity of type 4 fimbriae to the GSP protein-secretion systems and pilY1 encodes a gonococcal PilC homologue., *Molecular microbiology*, 1996, **22**, 161–73.

128. C. L. Giltner, M. Habash and L. L. Burrows, Pseudomonas aeruginosa minor pilins are incorporated into type IV Pili, *Journal of Molecular Biology*, 2010, **398**, 444–461.

129. H. L. Howie, S. L. Shiflett and M. So, Extracellular signal-regulated kinase activation by Neisseria gonorrhoeae downregulates epithelial cell proapoptotic proteins Bad and Bim, *Infection and Immunity*, 2008, **76**, 2715–2721.

130. R. T. Irvin, P. Doig, K. K. Lee, P. A. Sastry, W. Paranchych, T. Todd and R. S. Hodges, Characterization of the Pseudomonas aeruginosa pilus adhesin: confirmation that the pilin structural protein subunit contains a human epithelial cell-binding domain., *Infection and immunity*, 1989, **57**, 3720–6.

131. B. Maier, L. Potter, M. So, C. D. Long, H. S. Seifert and M. P. Sheetz, Single pilus motor forces exceed 100 pN., *Proceedings of the National Academy of Sciences of the United States of America*, 2002, **99**, 16012–7.

132. A. Beaussart, A. E. Baker, S. L. Kuchma, S. El-Kirat-Chatel, G. A. Otoole and Y. F. Dufrêne, Nanoscale adhesion forces of Pseudomonas aeruginosa type IV pili, *ACS Nano*, 2014, **8**, 10723–10733.

133. F. Jin, J. C. Conrad, M. L. Gibiansky and G. C. L. Wong, Bacteria use type-IV pili to slingshot on surfaces, *Proceedings of the National Academy of Sciences*, 2011, **108**, 12617–12622.

134. J. M. Skerker and H. C. Berg, Direct observation of extension and retraction of type IV pili, *Proceedings of the National Academy of Sciences*, 2001, **98**, 6901–6904.

135. C. K. Ellison, J. Kan, R. S. Dillard, D. T. Kysela, A. Ducret, C. Berne, C. M. Hampton, Z. Ke, E. R. Wright, N. Biais, A. B. Dalia and Y. V. Brun, Obstruction of pilus retraction stimulates bacterial surface sensing, *Science (New York, N.Y.)*, 2017, **358**, 535–538.

136. J. J. Bertrand, J. T. West and J. N. Engel, Genetic analysis of the regulation of type IV pilus function by the Chp chemosensory system of Pseudomonas aeruginosa, *Journal of Bacteriology*, 2010, **192**, 994–1010.

137. L. R. Hmelo, B. R. Borlee, H. Almblad, M. E. Love, T. E. Randall, B. S. Tseng, C. Lin, Y. Irie, K. M. Storek, J. J. Yang, R. J. Siehnel, P. L. Howell, P. K. Singh, T. Tolker-Nielsen, M. R. Parsek, H. P. Schweizer and J. J. Harrison, Precision-engineering the Pseudomonas aeruginosa genome with two-step allelic exchange, *Nature Protocols*, 2015, **10**, 1820–1841.

138. J. Schindelin, I. Arganda-Carreras, E. Frise, V. Kaynig, M. Longair, T. Pietzsch, S. Preibisch, C. Rueden, S. Saalfeld, B. Schmid, J.-Y. Tinevez, D. J. White, V. Hartenstein, K. Eliceiri, P. Tomancak and A. Cardona, Fiji: an open-source platform for biological-image analysis, *Nature Methods*, 2012, **9**, 676 –682.

139. A. Vogel and V. Venugopalan, Mechanisms of pulsed laser ablation of biological tissues, *Chemical Reviews*, 2003, **103**, 577–644.

140. A. Vogel, J. Noack, G. Hüttman and G. Paltauf, Mechanisms of femtosecond laser nanosurgery of cells and tissues, *Applied Physics B: Lasers and Optics*, 2005, **81**, 1015–1047.

141. K. R. Rau, P. A. Quinto-Su, A. N. Hellman and V. Venugopalan, Pulsed laser microbeam-induced cell lysis: Time-resolved imaging and analysis of hydrodynamic effects, *Biophysical Journal*, 2006, **91**, 317–329.

142. M. Gazor, S. S. A. Talesh, A. Kavianpour, M. Khatami, A. Javidanbardan and S. N. Hosseini, A Novel Cell Disruption Approach: Effectiveness of Laser-induced Cell Lysis of Pichia pastoris in the Continuous System, *Biotechnology and Bioprocess Engineering*, 2018, **23**, 49–54.

143. L. Ping, J. Birkenbeil and S. Monajembashi, Swimming behavior of the monotrichous bacterium *Pseudomonas fluorescens* SBW25, *FEMS Microbiology Ecology*, 2013, **86**, 36–44.

144. M. Krishnan, N. Mojarad, P. Kukura and V. Sandoghdar, Geometry-induced electrostatic trapping of nanometric objects in a fluid, *Nature*, 2010, **467**, 692–695.

145. M. L. Gibiansky, J. C. Conrad, F. Jin, V. D. Gordon, D. A. Motto, M. A. Mathewson, W. G. Stopka, D. C. Zelasko, J. D. Shrout and G. C. Wong, Bacteria use type IV pili to walk upright and detach from surfaces, *Science*, 2010, **330**, 197–197.

146. H.-S. M. Park, M. Wolfgang and M. Koomey, Modification of Type IV Pilus- Associated Epithelial Cell Adherence and Multicellular Behavior by the PilU Protein of Neisseria gonorrhoeae, *Infection and Immunity*, 2002, **70**, 3891–3903.

147. S. L. Kuchma, N. J. Delalez, L. M. Filkins, E. A. Snavely, J. P. Armitage and G. A. O'Toole, Cyclic di-GMP-mediated repression of swarming motility by Pseudomonas aeruginosa PA14 requires the MotAB stator., *Journal of bacteriology*, 2015, **197**, 420–30.

148. C. L. Giltner, Y. Nguyen and L. L. Burrows, Type IV Pilin Proteins: Versatile Molecular Modules, *Microbiology and Molecular Biology Reviews*, 2012, **76**, 740–772.

149. Y. W. Chang, L. A. Rettberg, A. Treuner-Lange, J. Iwasa, L. S øgaard Andersen and G. J. Jensen, Architecture of the type IVa pilus machine, *Science*, 2016, **351**, aad2001.

150. W. E. Thomas, V. Vogel and E. Sokurenko, Biophysics of Catch Bonds, *Annual Review of Biophysics*, 2008, **37**, 399–416.

151. N. Biais, D. L. Higashi, J. Brujic, M. So and M. P. Sheetz, Force-dependent polymorphism in type IV pili reveals hidden epitopes., *Proceedings of the National Academy of Sciences of the United States of America*, 2010, **107**, 11358–63.

152. O. Kiehn, Decoding the organization of spinal circuits that control locomotion, *Nature Reviews Neuroscience*, 2016, **17**, 224–238.

153. V. Dietz, Proprioception and locomotor disorders, *Nature Reviews Neuroscience*, 2002, **3**, 781–790.

154. D. W. Adams, J. M. Pereira, C. Stoudmann, S. Stutzmann and M. Blokesch, The type IV pilus protein PilU functions as a PilT-dependent retraction ATPase, *PLoS Genetics*, 2019, **15**, e1008393.

155. J. L. Chlebek, H. Q. Hughes, A. S. Ratkiewicz, R. Rayyan, J. C. Y. Wang, B. E. Herrin, T. N. Dalia, N. Biais and A. B. Dalia, PilT and PilU are homohexameric ATPases that coordinate to retract type IVa pili, *PLoS Genetics*, 2019, **15**, e1008448.

156. F. Jünger, P. V. Olshausen and A. Rohrbach, Fast, label-free super-resolution live-cell imaging using rotating coherent scattering (ROCS) microscopy, *Scientific Reports*, 2016, **6**, 1.

157. J. Dreier, M. Castello, G. Coceano, R. Cáceres, J. Plastino, G. Vicidomini and I. Testa, Smart scanning for low-illumination and fast RESOLFT nanoscopy in vivo, *Nature Communications*, 2019, **10**, 1.

158. A. D. Malay, N. Miyazaki, A. Biela, S. Chakraborti, K. Majsterkiewicz, I. Stupka, C. S. Kaplan, A. Kowalczyk, B. M. A. G. Piette, G. K. A. Hochberg, D. Wu, T. P. Wrobel, A. Fineberg, M. S. Kushwah, M. Kelemen, P. Vavpetič, P. Pelicon, P. Kukura, J. L. P. Benesch, K. Iwasaki and J. G. Heddle, An ultra-stable gold-coordinated protein cage displaying reversible assembly, *Nature*, 2019, 1.

159. A. O'Neil, P. E. Prevelige, G. Basu and T. Douglas, Coconfinement of Fluorescent Proteins: Spatially Enforced Communication of GFP and mCherry Encapsulated within the P22 Capsid, *Biomacromolecules*, 2012, **13**, 3902–3907.

160. D. P. Patterson, B. Schwarz, R. S. Waters, T. Gedeon and T. Douglas, Encapsulation of an Enzyme Cascade within the Bacteriophage P22 Virus-Like Particle, *ACS Chemical Biology*, 2014, **9**, 359–365.

161. S. Qazi, H. M. Miettinen, R. A. Wilkinson, K. McCoy, T. Douglas and B. Wiedenheft, Programmed Self- Assembly of an Active P22-Cas9 Nanocarrier System, *Molecular Pharmaceutics*, 2016, **13**, 1191–1196.

162. P. C. Jordan, D. P. Patterson, K. N. Saboda, E. J. Edwards, H. M. Miettinen, G. Basu, M. C. Thielges and T. Douglas, Self-assembling biomolecular catalysts for hydrogen production, *Nature Chemistry*, 2016, **8**, 179–185.

163. J. D. Fiedler, S. D. Brown, J. L. Lau and M. G. Finn, RNA-Directed Packaging of Enzymes within Virus-like Particles, *Angewandte Chemie International Edition*, 2010, **49**, 9648–9651.

164. B. Wörsdörfer, Z. Pianowski and D. Hilvert, Efficient in Vitro Encapsulation of Protein Cargo by an Engineered Protein Container, *Journal of the American Chemical Society*, 2012, **134**, 909–911.

165. M. Comellas-Aragonès, H. Engelkamp, V. I. Claessen, N. A. J. M. Sommerdijk, A. E. Rowan, P. C. M. Christianen, J. C. Maan, B. J. M. Verduin,

J. J. L. M. Cornelissen and R. J. M. Nolte, A virus-based single-enzyme nanoreactor, *Nature Nanotechnology*, 2007, **2**, 635–639.

166. J. E. Glasgow, S. L. Capehart, M. B. Francis and D. Tullman-Ercek, Osmolyte-Mediated Encapsulation of Proteins inside MS2 Viral Capsids, *ACS Nano*, 2012, **6**, 8658–8664.

167. J. Johnson, Structures of virus and virus-like particles, *Current Opinion in Structural Biology*, 2000, **10**, 229–235.

168. T. Douglas, Viruses: Making Friends with Old Foes, *Science*, 2006, **312**, 873–875.

169. P. M. Harrison and P. Arosio, The ferritins: molecular properties, iron storage function and cellular regulation, *Biochimica et Biophysica Acta (BBA) - Bioenergetics*, 1996, **1275**, 161–203.

170. M. Uchida, S. Kang, C. Reichhardt, K. Harlen and T. Douglas, The ferritin superfamily: Supramolecular templates for materials synthesis, *Biochimica et Biophysica Acta (BBA) - General Subjects*, 2010, **1800**, 834–845.

171. A. L. Horwich, W. A. Fenton, E. Chapman and G. W. Farr, Two Families of Chaperonin: Physiology and Mechanism, *Annual Review of Cell and Developmental Biology*, 2007, **23**, 115–145.

172. K. K. Kim, R. Kim and S.-H. Kim, Crystal structure of a small heat-shock protein, *Nature*, 1998, **394**, 595–599.

173. W. Aumiller, M. Uchida and T. Douglas, Protein cage assembly across multiple length scales, *Chemical Society Reviews*, 2018, **47**, 3433–3469.

174. H. F. Lodish, A. Berk, C. A. Kaiser, M. Krieger, A. Bretscher, H. Ploegh, A. Amon and K. C. Martin, *Molecular cell biology*, Macmillan Learning, 8th edn., 2016.

175. E. C. Theil and D. J. Goss, Living with Iron (and Oxygen): Questions and Answers about Iron Homeostasis, *Chemical Reviews*, 2009, **109**, 4568–4579.

176. P. Arosio and S. Levi, Ferritin, iron homeostasis, and oxidative damage, *Free Radical Biology and Medicine*, 2002, **33**, 457–463.

177. J. Padilla, C. Colovos and T. Yeates, Nanohedra: Using symmetry to design self assembling protein cages, layers, crystals, and filaments, *Proceedings of the National Academy of Sciences of the United States of America*, 2001, **98**, 2217–2221.

178. N. King, W. Sheffler, M. Sawaya, B. Vollmar, J. Sumida, I. André, T. Gonen, T. Yeates and D. Baker, Computational design of self-assembling protein nanomaterials with atomic level accuracy, *Science*, 2012, **336**, 1171–1174.

179. B. Holliday and C. Mirkin, Strategies for the Construction of Supramolecular Compounds through Coordination Chemistry, *Angewandte Chemie - International Edition*, 2001, **40**, 2023–2043.

180. E. Salgado, R. Radford and F. Tezcan, Metal-directed protein self- assembly, *Accounts of Chemical Research*, 2010, **43**, 661–672.

181. J. Brodin, X. Ambroggio, C. Tang, K. Parent, T. Baker and F. Tezcan, Metal-directed, chemically tunable assembly of one-, two- and three-dimensional crystalline protein arrays, *Nature Chemistry*, 2012, **4**, 375–382.

182. B. Der, M. MacHius, M. Miley, J. Mills, T. Szyperski and B. Kuhlman, Metal-mediated affinity and orientation specificity in a computationally designed protein homodimer, *Journal of the American Chemical Society*, 2012, **134**, 375–385.

183. W. Zhang, Q. Luo, L. Miao, C. Hou, Y. Bai, Z. Dong, J. Xu and J. Liu, Self- assembly of glutathione S-transferase into nanowires, *Nanoscale*, 2012, **4**, 5847–5851.

184. D. Huard, K. Kane and F. Akif Tezcan, Re-engineering protein interfaces yields copper-inducible ferritin cage assembly, *Nature Chemical Biology*, 2013, **9**, 169–176.

185. A. Antson, J. Otridge, A. Brzozowski, E. Dodson, G. Dodson, K. Wilson, T. Smith, M. Yang, T. Kurecki and P. Gollnick, The structure of trp rna-binding attenuation protein, *Nature*, 1995, **374**, 693–700.

186. J. Heddle, T. Yokoyama, I. Yamashita, S.-Y. Park and J. Tame, Rounding up: Engineering 12-Membered Rings from the Cyclic 11-Mer TRAP, *Structure*, 2006, **14**, 925–933.

187. J. Heddle, I. Fujiwara, H. Yamadaki, S. Yoshii, K. Nishio, C. Addy, I. Yamashita and J. Tame, Using the ring-shaped protein TRAP to capture and confine gold nanodots on a surface, *Small*, 2007, **3**, 1950–1956.

188. F. Miranda, K. Iwasaki, S. Akashi, K. Sumitomo, M. Kobayashi, I. Yamashita, J. Tame and J. Heddle, A self-assembled protein nanotube with high aspect ratio, *Small*, 2009, **5**, 2077–2084.

189. M. Imamura, T. Uchihashi, T. Ando, A. Leifert, U. Simon, A. Malay and J. Heddle, Probing structural dynamics of an artificial protein cage using high-speed atomic force microscopy, *Nano Letters*, 2015, **15**, 1331–1335.

190. H. Häkkinen, The gold-sulfur interface at the nanoscale, *Nature Chemistry*, 2012, **4**, 443–455.

191. F. Arnold and J.-H. Zhang, Metal-mediated protein stabilization, *Trends in Biotechnology*, 1994, **12**, 189–192.

192. J. Brodin, J. Carr, P. Sontz and F. Tezcan, Exceptionally stable, redox-active supramolecular protein assemblies with emergent properties, *Proceedings of the National Academy of Sciences of the United States of America*, 2014, **111**, 2897–2902.

193. K. Bhabak, B. Bhuyan and G. Mugesh, Bioinorganic and medicinal chemistry: Aspects of gold(i)-protein complexes, *Dalton Transactions*, 2011, **40**, 2099–2111.

194. E. Sasaki, D. Böhringer, M. Van De Waterbeemd, M. Leibundgut, R. Zschoche, A. Heck, N. Ban and D. Hilvert, Structure and assembly of scalable porous protein cages, *Nature Communications*, 2017, **8**, year.

195. D. Caspar and A. Klug, Physical principles in the construction of regular viruses., *Cold Spring Harbor symposia on quantitative biology*, 1962, **27**, 1–24.

196. B. Prasad and M. Schmid, Principles of virus structural organization, *Advances in Experimental Medicine and Biology*, 2012, **726**, 17–47.

197. J. de Las Rivas and C. Fontanillo, Protein-protein interactions essentials: Key concepts to building and analyzing interactome networks, *PLoS Computational Biology*, 2010, **6**, 1–8.

198. S. Jones and J. M. Thornton, *Principles of protein-protein interactions*, 1996.

199. S. A. Hunter and J. R. Cochran, in *Methods in Enzymology*, Academic Press Inc., 2016, vol. 580, pp. 21–44.

200. W. Ma, L. Yang and L. He, *Overview of the detection methods for equilibrium dissociation constant KD of drug- receptor interaction*, 2018.

201. G. Perret and P. Simon, Radioreceptor assay: principles and applications to pharmacology, *Journal de pharmacologie*, 1984, **15**, 265–286.

202. P. Crevat-Pisano, C. Hariton, P. H. Rolland and J. P. Cano, Fundamental aspects of radioreceptor assays, *Journal of Pharmaceutical and Biomedical Analysis*, 1986, **4**, 697–716.

203. V. J. LiCata and A. J. Wowor, in *Biophysical Tools for Biologists, Volume One: In Vitro Techniques*, Academic Press, 2008, vol. 84 of Methods in Cell Biology, pp. 243–262.

204. A. Gijsbers, T. Nishigaki and N. Sánchez-Puig, Fluorescence anisotropy as a tool to study protein-protein interactions, *Journal of Visualized Experiments*, 2016, **2016**, e54640.

205. J. L. Cole, J. W. Lary, T. P. Moody and T. M. Laue, Analytical Ultracentrifugation: Sedimentation Velocity and Sedimentation Equilibrium, *Methods in Cell Biology*, 2008, **84**, 143–179.

206. J. Liu, J. D. Andya and S. J. Shire, A critical review of analytical ultracentrifugation and field flow fractionation methods for measuring protein aggregation, *AAPS Journal*, 2006, **8**, 580–589.

207. W. F. Stafford, Boundary analysis in sedimentation velocity experiments, *Methods in Enzymology*, 1994, **240**, 478–501.

208. P. Schuck, Size-distribution analysis of macromolecules by sedimentation velocity ultracentrifugation and Lamm equation modeling, *Biophysical Journal*, 2000, **78**, 1606–1619.

209. J. C. Hansen, J. Lebowitz and B. Demeler, Analytical Ultracentrifugation of Complex Macromolecular Systems, *Biochemistry*, 1994, **33**, 13155–13163.

210. A. Balbo, P. H. Brown, E. H. Braswell and P. Schuck, Measuring Protein-Protein Interactions by Equilibrium Sedimentation, *Current Protocols in Immunology*, 2007, **79**, 18.8.1–18.8.28.

211. P. Barton, R. P. Austin and R. E. Fessey, in *Comprehensive Medicinal Chemistry II*, ed. J. B. Taylor and D. J. Triggle, Elsevier, Oxford, 2006, vol. 5, pp. 321–340.

212. A. Saponaro, Isothermal Titration Calorimetry: A Biophysical Method to Characterize the Interaction between Label-free Biomolecules in Solution, *Bio-Protocol*, 2018, **8**, e2957.

213. K. Bouchemal, *New challenges for pharmaceutical formulations and drug delivery systems characterization using isothermal titration calorimetry*, 2008.

214. X. Du, Y. Li, Y. L. Xia, S. M. Ai, J. Liang, P. Sang, X. L. Ji and S. Q. Liu, *Insights into proteinligand interactions: Mechanisms, models, and methods*, 2016.

215. T. Krell, *Microcalorimetry: A response to challenges in modern biotechnology*, 2008.

216. M. L. Doyle, G. Louie, P. R. Dal Monte and T. D. Sokoloski, Tight binding affinities determined from thermodynamic linkage to protons by titration calorimetry, *Methods in Enzymology*, 1995, **259**, 183–194.

217. M. W. Freyer and E. A. Lewis, in *Biophysical Tools for Biologists, Volume One: In Vitro Techniques*, Academic Press, 2008, vol. 84 of Methods in Cell Biology, pp. 79–113.

218. K. Rajarathnam and J. Rösgen, Isothermal titration calorimetry of membrane proteins – Progress and challenges, *Biochimica et Biophysica Acta (BBA) - Biomembranes*, 2014, **1838**, 69–77.

219. G. De Crescenzo, C. Boucher, Y. Durocher and M. Jolicoeur, Kinetic Characterization by Surface Plasmon Resonance-Based Biosensors: Principle and Emerging Trends, *Cellular and Molecular Bioengineering*, 2008, **1**, 204–215.

220. S. G. Patching, Surface plasmon resonance spectroscopy for characterisation of membrane proteinligand interactions and its potential for drug discovery, *Biochimica et Biophysica Acta (BBA) - Biomembranes*, 2014, **1838**, 43–55.

221. M. Raghavan and P. J. Bjorkman, BIAcore: a microchip-based system for analyzing the formation of macromolecular complexes, *Structure*, 1995, **3**, 331–333.

222. R. L. Rich and D. G. Myszka, BIACORE J: a new platform for routine biomolecular interaction analysis†, *Journal of Molecular Recognition*, 2001, **14**, 223–228.

223. F. Real-Fernández, G. Rossi, F. Panza, F. Pratesi, P. Migliorini and P. Rovero, in *Surface Plasmon Resonance Method to Evaluate Anti-citrullinated Protein/Peptide Antibody Affinity to Citrullinated Peptides*, ed. G. Houen, Springer New York, New York, NY, 2015, pp. 267–274.

224. H. H. Nguyen, J. Park, S. Kang and M. Kim, *Surface plasmon resonance: A versatile technique for biosensor applications*, 2015.

225. P. A. Van Der Merwe, in *Surface Plasmon Resonance*, ed. S. E. Harding and B. Z. Chowdhry, Oxford University Press, Oxford, 1st edn., 2001, ch. 6, pp. 137 – 170.

226. A. Y. Joshi, S. C. Sharma and S. P. Harsha, Zeptogram scale mass sensing using single walled carbon nanotube based biosensors, *Sensors and Actuators, A: Physical*, 2011, **168**, 275–280.

227. P. L. Kastritis and A. M. Bonvin, On the binding affinity of macromolecular interactions: Daring to ask why proteins interact, *Journal of the Royal Society Interface*, 2013, **10**, 20120835.

228. E. Pettersen, T. Goddard, C. Huang, G. Couch, D. Greenblatt, E. Meng and T. Ferrin, UCSF Chimera - A visualization system for exploratory research and analysis, *Journal of Computational Chemistry*, 2004, **25**, 1605–1612.

229. E. Nogales, An electron microscopy journey in the study of microtubule structure and dynamics, *Protein Science*, 2015, **24**, 1912–1919.

230. J. Löwe, H. Li, K. H. Downing and E. Nogales, Refined structure of $\alpha\beta$-tubulin at 3.5 Å resolution, *Journal of Molecular Biology*, 2001, **313**, 1045–1057.

231. F. Montecinos-Franjola, P. Schuck and D. L. Sackett, Tubulin Dimer Reversible Dissociation, *Journal of Biological Chemistry*, 2016, **291**, 9281–9294.

232. R. C. Williams and H. W. Detric, Reversible Dissociation of the $\alpha\beta$ Dimer of Tubulin from Bovine Brain, *Biochemistry*, 1978, **17**, 3900–3907.

233. H. William Detrich, R. C. Williams and L. Wilson, Effect of Colchicine Binding on the Reversible Dissociation of the Tubulin Dimer, *Biochemistry*, 1982, **21**, 2392–2400.

234. M. R. Mejillano and R. H. Himes, Tubulin Dimer Dissociation Detected by Fluorescence Anisotropy, *Biochemistry*, 1989, **28**, 6518–6524.

235. D. L. Sackett and R. E. Lippoldt, Thermodynamics of Reversible Monomer-Dimer Association of Tubulin, *Biochemistry*, 1991, **30**, 3511–3517.

236. D. Panda, B. Bhattacharyya and S. Roy, Reversible Dimer Dissociation of Tubulin S and Tubulin Detected by Fluorescence Anisotropy, *Biochemistry*, 1992, **31**, 9709–9716.

237. K. E. Shearwin and S. N. Timasheff, Effect of Colchicine Analogues on the Dissociation of $\alpha\beta$ Tubulin into Subunits: The Locus of Colchicine Binding, *Biochemistry*, 1994, **33**, 894–901.

238. K. E. Shearwin, B. Perez-Ramirez and S. N. Timashef, Linkages between the Dissociation of $\alpha\beta$ Tubulin into Subunits and Ligand Binding: The Ground State of Tubulin Is the GDP Conformation, *Biochemistry*, 1994, **33**, 885–893.

239. M. Menéndez, G. Rivas, J. F. Dıáz and J. M. Andreu, Control of the Structural Stability of the Tubulin Dimer by One High Affinity Bound Magnesium Ion at Nucleotide N-site, *Journal of Biological Chemistry*, 1998, **273**, 167–176.

240. M. Caplow and L. Fee, Dissociation of the tubulin dimer is extremely slow, thermodynamically very unfavorable, and reversible in the absence of an energy source, *Molecular Biology of the Cell*, 2002, **13**, 2120–2131.

241. M. Castoldi and A. V. Popov, Purification of brain tubulin through two cycles of polymerization- depolymerization in a high- molarity buffer, *Protein Expression and Purification*, 2003, **32**, 83–88.

242. K. C. Abruzzi, A. Smith, W. Chen and F. Solomon, Protection from Free β-tubulin by the β-tubulin Binding Protein Rbl2p, *Molecular and Cellular Biology*, 2002, **22**, 138–147.

243. F. Montecinos-Franjola, S. K. Chaturvedi, P. Schuck and D. L. Sackett, All tubulins are not alike: Heterodimer dissociation differs among different biological sources, *Journal of Biological Chemistry*, 2019, **294**, 10315–10324.